X-ray Optical Delay Line at EuXFEL and Investigation of B_4C Damage Threshold

Dissertation
zur Erlangung des Doktorgrades
an der Fakultät für Mathematik, Inforamatik und Naturwissenschaften
Fachberreich Physik
der Universität Hamburg

vorgelegt von
Marziyeh Sadat Tavakkoly

Hamburg
2024

Gutachter der Dissertation:	Prof. Dr. Wolfgang Hillert Dr. Maurizio Vannoni
Zusammensetzung der Prüfungskommission:	Prof. Dr. Wolfgang Hillert Prof. Dr. Markus Ilchen Dr. Michael Meyer Prof. Dr. Daniela Pfannkuche Dr. Maurizio Vannoni
Vorsitzende/r der Prüfungskommission:	Prof. Dr. Daniela Pfannkuche
Datum der Disputation:	12.02.2025
Vorsitzender Fach-Promotionsausschusses PHYSIK:	Prof. Dr. Wolfgang Parak
Leiter des Fachbereichs PHYSIK:	Prof. Dr. Markus Drescher
Dekan der Fakultät MIN:	Prof. Dr.-Ing. Norbert Ritter

Acknowledgements

I would like to express my deepest gratitude to my supervisor, Dr. Maurizio Vannoni, for his invaluable guidance and support throughout my research journey. His expertise in X-ray optics and his dedication to imparting knowledge have been instrumental in my academic and personal growth. His approach to mentorship—teaching me not only solutions but also the skills to solve problems independently—has been a profound and lasting lesson that I will carry forward in my career.

I would also like to extend my sincere thanks to my supervisors, Prof. Wolfgang Hillert and Dr. Michael Meyer for their unwavering support and for making my path through this Ph.D. journey much smoother.

I am incredibly grateful to Dr. Harald Sinn, whose ideas, brainstorming, and continuous support have been pivotal throughout my research.

A special thanks goes to all the members of the XRO, SQS teams, and FZU collaborators who greatly contributed to the success of the damage experiment. Their assistance during shifts was invaluable, and without their help, this experiment would not have been possible. In particular, I would like to acknowledge the following individuals for their valuable support in the design and measurement of samples, as well as during beam time, conducted under proposal number 900332:

XRO Team: Immo Bahns, Idoia Freijo Martin, Mikako Makita, Liubov Samoylova, Silja Schmidtchen, Kelin Tasca, Antje Trapp

SQS Team: Thomas Baumann, Rebecca Boll, Alberto De Fanis, Simon Dold, Tommaso Mazza, Jacobo Montano, Yevheniy Ovcharenko

FZU collaborators: Tomas Burian, Jaromir Chalupsky, Vera Hajkova, Alzbeta Horynova, Simon Jelinek, Libor Juha, Nikita Medvedev, Vojtech Vozda

I would also like to thank the following individuals whose expertise and contributions were essential to success of the ODL project:

ME: Daniele La Civita, Marc Planas, Fan Yang

SEC: Carsten Deiter

SPF: Svitozar Serkez

XPD: Jan Grünert, Andreas Koch

DESY collaborators: Winni Decking, Torsten Wohlenberg

For the creation of the coating, I am grateful to Michael Störmer, and for the OASYS software, my thanks go to Luca Rebuffi and Manuel Sanchez del Rio.

Finally, this work was supported by the HIR3X – Helmholtz International Laboratory on Reliability, Repetition, Results at the most advanced X-ray Sources, and I am deeply thankful for the funding that made this research possible.

Dedication

To my love, Reza,

for his endless love, unwavering support, and constant encouragement.

To my family,

for nurturing me with endless affection and belief in my dreams.

Declaration

I hereby declare and affirm that this doctoral dissertation is my own work and that I have not used any aids and sources other than those indicated.

If electronic resources based on generative artificial intelligence (gAI) were used in the course of writing this dissertation, I confirm that my own work was the main and value-adding contribution and that complete documentation of all resources used is available in accordance with good scientific practice. I am responsible for any erroneous or distorted content, incorrect references, violations of data protection and copyright law or plagiarism that may have been generated by the gAI.

25.11.2024

Date

Signature of doctoral candidate

Abstract

A two-color pump-probe experiment is essential for investigating complex chemical reactions and electronic dynamics in quantum systems. To facilitate this at the European X-ray Free Electron Laser (EuXFEL), a Magnetic Chicane (MC) was installed between the undulators to deflect the electron beam; however, using only the MC does generally not allow for zero and negative temporal delay between the two pulses of different wavelengths. The X-ray Optical Delay Line (ODL) was developed to provide tunable temporal delays (positive, zero, and negative) and adjustable wavelengths in pump-probe experiments. The ODL consists of four flat mirrors made of B_4C (50 nm) on a Si substrate, designed to deflect the photon beam and will be installed parallel to the Magnetic Chicane. The specifications of the ODL, both from mechanical and optical perspectives, are detailed, supported by wavefront propagation, ray tracing, and finite element analysis (FEA) simulations to predict its performance.

The first mirror of the ODL features a fine motorized pitch rotation mechanism, in addition to the fourth mirror, which includes motorized pitch, roll, and vertical movements. COMSOL ray tracing simulations confirm that this motorized movement is adequate for aligning the mirrors. The first mirror is water-cooled to mitigate excessive heat and reduce spontaneous background radiation. The heat load and mechanical structure causes a bump of 9.5 nm on the first mirror (M1), based on simulations. The quality of the mirror surfaces was measured using a Fizeau interferometer. The roughness was assessed before and after coating using a White Light Interferometer. SRW (Synchrotron Radiation Workshop) wavefront propagation simulations further demonstrated that the mirrors maintain excellent quality, resulting in no degradation of the beam.

The European XFEL operates at a repetition rate of up to 4.5 MHz with femtosecond pulse duration, presenting challenges for mirror durability under both single-shot and multi-pulse conditions. The absorbed dose was calculated for single-shot damage and determined that for higher pulse energies, users should open some undulators upstream of the ODL to prevent damage. For multi-pulse conditions, COMSOL heat transfer simulations assessed the accumulated temperature over time.

To address damage concerns, experiments were conducted at the SQS instrument to investigate the damage thresholds. Results indicated that the fluence threshold for single-shot damage of B_4C (50 nm)/Si-substrate at 1 keV and a grazing angle of 9 mrad is 0.34 µJ/µm^2, compared to 0.16 µJ/µm^2 for uncoated silicon, highlighting the advantages of B_4C as a coating. The experiments covered grazing angles of 9, 15, and 19 mrad, resulting in measuring an electron collision length of 8.6 nm, indicating enhanced heat transport through the material and increased damage thresholds. These findings offer critical insights for designing more resilient optical components in XFEL facilities.

Additionally, Monte Carlo and COMSOL simulations were performed to estimate the energy deposition depth and temperature profiles over time and depth within the material. A safety diagram outlining safe operating parameters for future ODL users was created, indicating operating limits based on photon energy and pulse energy to guide decisions on opening undulators and prevent mirror damage.

Zusammenfassung

Ein zweifarben Pump-Probe-Experiment ist für die Untersuchung komplexer chemischer Reaktionen und Elektronendynamik in Quantensystemen unerlässlich. Um dies am European XFEL zu ermöglichen, wurde eine magnetische Schikane (MC) zwischen den Undulatoren installiert, um den Elektronenstrahl abzulenken; die alleinige Verwendung der MC ermöglicht generell jedoch keine zeitliche Verzögerung von Null zwischen den beiden Pulsen von unterschiedlicher Wellenlänge. Die X-ray Optical Delay Line (ODL) wurde entwickelt, um abstimmbare zeitliche Verzögerungen (positiv, null und negativ) und einstellbare Wellenlängen in Pump-Probe-Experimenten zu ermöglichen. Die ODL besteht aus vier planen Spiegeln aus B_4C (50 nm) auf einem Si-Substrat, die den Photonenstrahl ablenken und parallel zu der magnetischen Schikane installiert werden sollen. Die Spezifikationen der ODL, sowohl aus mechanischer als auch aus optischer Sicht, werden detailliert beschrieben und durch Simulationen der Wellenfrontausbreitung, Strahlverfolgung und Finite-Elemente-Analyse (FEA) unterstützt, um seine Leistung vorherzusagen.

Der erste Spiegel des ODL verfügt über einen feinmotorisierten Mechanismus für die Drehung um die Längsachse, während der vierte Spiegel motorisierte Bewegungen für die Längsachse, die Querachse und die Hochachse aufweist. COMSOL-Raytracing-Simulationen bestätigen, dass diese motorisierte Bewegung für die Ausrichtung der Spiegel ausreichend ist. Der erste Spiegel ist wassergekühlt, um übermäßige Hitze zu vermeiden und die spontane Hintergrundstrahlung zu reduzieren. Die Wärmebelastung und die mechanische Struktur verursachen auf dem ersten Spiegel (M1) eine Erhebung von 9.5 nm, wie Simulationen ergaben. Die Qualität der Spiegeloberflächen wurde mit einem Fizeau-Interferometer gemessen. Die Rauheit wurde vor und nach der Beschichtung mit einem Weißlichtinterferometer gemessen. SRW-Wellenfrontsimulationen zeigten außerdem, dass die Spiegel eine ausgezeichnete Qualität aufweisen und der Strahl dadurch nicht beeinträchtigt wird.

Der European XFEL arbeitet mit einer Repetitionsrate von bis zu 4.5 MHz und einer Pulsdauer von Femtosekunden, was die Haltbarkeit der Spiegel sowohl unter Einzel- als auch unten "Multipuls-Bedingungen" vor Herausforderungen stellt. Wir berechneten die Energiedosis für Einzelschussschäden und stellten fest, dass die Nutzer bei höheren Energien einige Undulatoren vor dem ODL öffnen soll-

ten, um Schäden zu vermeiden. Für Multipuls-Bedingungen wurde mit COMSOL-Wärmeübertragungssimulationen die akkumulierte Temperatur im Laufe der Zeit bewertet.

Um den Bedenken hinsichtlich einer Beschädigung Rechnung zu tragen, führten wir Experimente am SQS-Instrument durch, um die Schadensschwellen zu untersuchen. Die Ergebnisse zeigten, dass die Fluenzschwelle für die Beschädigung von B_4C (50 nm)/Si-sub bei 1 keV und einem Einfallswinkel von 9 mrad bei 0.34 µJ/µm^2 liegt, verglichen mit 0.16 µJ/µm^2 für unbeschichtetes Silizium, was die Vorteile von B_4C als Beschichtung unterstreicht. Bei den Experimenten wurden Einfallswinkel von 9, 15 und 19 mrad erfasst, was zur Messung einer Elektronenkollisionslänge von 8,6 nm führte, was auf einen verbesserten Wärmetransport durch das Material und eine höhere Zerstörungsschwelle hinweist. Diese Ergebnisse liefern wichtige Erkenntnisse für die Entwicklung widerstandsfähigerer optischer Komponenten in XFEL-Anlagen.

Darüber hinaus wurden Monte-Carlo-Simulationen und COMSOL-Simulationen durchgeführt, um die Tiefe des Energieeintrags und die Temperaturprofile über die Zeit und die Tiefe im Material abzuschätzen. Es wurde ein Sicherheitsdiagramm mit sicheren Betriebsparametern für künftige ODL-Benutzer erstellt, das Betriebsgrenzen auf der Grundlage von Photonenenergie und Pulsenergie angibt, um Entscheidungen über das Öffnen von Undulatoren zu erleichtern und Spiegelschäden zu vermeiden.

Contents

List of Figures

List of Tables

CHAPTER 1 Introduction

Understanding our environment and the materials around us is essential for improving our quality of life. To achieve this, we rely on the field of physics, which helps us explore the tiny building blocks of the universe, including atoms and molecules. Many of these structures are too small to be seen with ordinary light, which is why we need special types of light, like X-rays, that have much shorter wavelengths. These X-rays can help us see and study things at the atomic level, such as viruses and bacteria, and are crucial for various scientific fields, including medical research and materials science [1].

The journey into X-ray science began with the discovery made by Wilhelm Conrad Röntgen in 1895. He found a new type of ray that could pass through solid objects, including the human body, and he called them X-rays. Röntgen quickly realized the potential of X-rays in medicine, famously taking the first X-ray image of his wife's hand shortly after his discovery. Since then, X-rays have been used not only in medicine but also in many other areas of research. For instance, X-ray diffraction helped scientists determine the structure of DNA just a few decades later [2, 3].

Traditionally, X-rays were produced using X-ray tubes, which are quite inefficient, converting only 1% of electrical energy into X-ray photons. The rest is lost as heat. However, a significant improvement came in the 1970s with the development of synchrotron radiation. Synchrotrons are large circular accelerators that speed up electrons to very high velocities using powerful magnets. As these electrons travel in circles, they produce extremely bright light, particularly in the X-ray range. This synchrotron light is millions of times brighter than that from a standard X-ray tube and can be tuned to specific wavelengths, making it much more useful for research [2, 3].

The evolution of X-ray sources continued with the invention of free electron lasers (FELs). The first FEL was developed by John Madey in 1971, and it represented a major step forward in X-ray technology. FELs can generate extremely short and intense X-ray pulses, allowing scientists to capture "snapshots" of molecular struc-

tures in a fraction of a second. This ability to take pictures faster than the processes that can damage samples has transformed fields like structural biology. Fig. 1.1 illustrates the progression of X-ray sources over the years, highlighting the increasing brilliance of these technologies and their advancements [1, 2, 4–6].

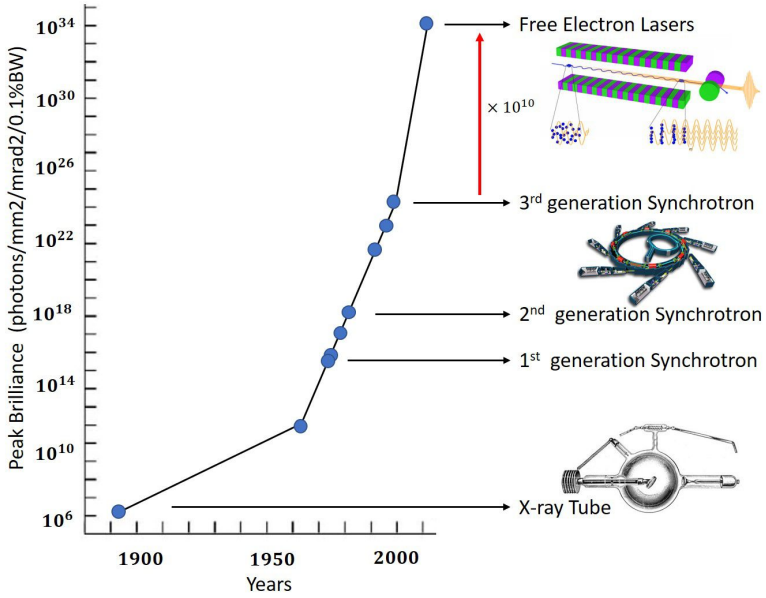

Figure 1.1: Timeline of X-ray Sources.

There are several FEL facilities around the world, as shown in Fig. 1.2, which emphasizes their distribution. One of the leading facilities in this area is the European XFEL, which produces X-ray flashes at an astonishing rate of 27,000 flashes per second. These flashes are a billion times brighter than conventional X-ray sources, providing unique opportunities for scientists to conduct cutting-edge research, particularly in understanding the structures of molecules.

A recent advancement in experimental techniques is the implementation of two-color pump-probe experiments. This approach enables researchers to investigate complex chemical reactions and material changes with remarkable precision. At European XFEL, this capability is facilitated by the use of a magnetic chicane and an Optical Delay Line (ODL) located between the undulator cells, which adjusts the timing of the photon pulses. These tools provide two synchronized sources with tunable temporal delays and adjustable wavelengths, opening up exciting new opportunities for experiments and investigations.

In this thesis, we will explore the importance of the ODL and its configuration, focusing on the challenges involved in aligning mirrors properly. Using simulations, we will analyze how small misalignments in the mirrors can affect the quality of the X-ray beam. Additionally, the materials chosen for the ODL mirrors will be discussed, including the reasons for selecting silicon and boron carbide (B_4C) as

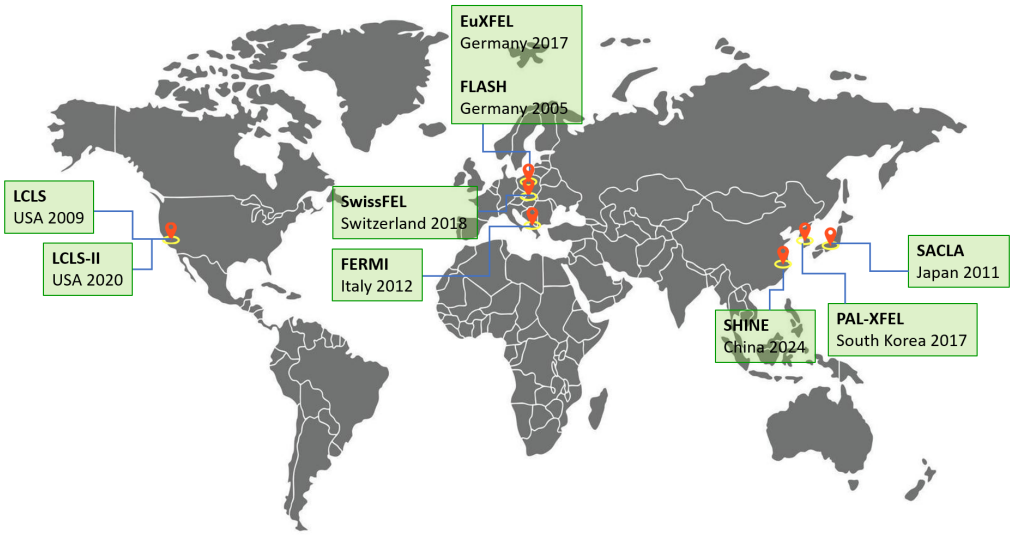

Figure 1.2: Free electron laser facilities in the world.

well as an explanation of how we manage the heat generated during operation.

A crucial aspect of this research is understanding how much energy the mirrors can withstand without incurring damage. Given that the ODL mirrors are positioned very close to the X-ray source, they are exposed to intense light and can be damaged if not properly managed.

By determining the damage thresholds for B_4C coatings on silicon, we aim to ensure that these optical elements can tolerate the intense conditions created by the European XFEL.

Additionally, we will investigate a critical parameter known as electron collision length, which plays a significant role in our research. The electron system can transport energy well beyond the initial absorption layer during femtosecond pulse events. In order to design optical components that can withstand higher instantaneous power and optimize scientific instruments for XFELs, it is necessary to understand the fundamental processes that influence the damage threshold.

This thesis is structured as follows:

- **Chapter 2** provides an overview of free electron lasers (FELs), detailing their operational principles and advantages over synchrotron radiation. It also introduces the European XFEL and its SQS scientific instrument, used in this research.

- **Chapter 3** elaborates on the ODL, discussing its capabilities, benefits, and challenges, including alignment and durability. This chapter presents simulations predicting the ODL stability and functionality under varying conditions.

- **Chapter 4** describes the damage experiments conducted to determine the thresholds for materials similar to those used in the ODL, including a comparative analysis of substrates with and without coatings.

- **Chapter 5** concludes the thesis by summarizing the research findings and outlining future directions for the ODL, including its manufacturing and installation, along with potential experiments with using ODL, and additional damage experiment to investigate electron collision length at varying photon energies.

In summary, this research aims to enhance our understanding of the optical and mechanical parameters vital for optimizing the ODL, as well as to identify the critical parameter of electron collision range, which plays a significant role in determining the damage threshold. We hope to improve experimental techniques and pave the way for future discoveries.

CHAPTER 2

Free Electron Lasers

2.1 Importance of Free Electron Lasers

Science relies on the determination of complex molecular structures in many fields, including structural biology, materials science, and chemistry which requires very bright X-ray sources. Traditional X-ray sources, such as medical X-ray tubes, have limitations in brightness and coherence, making it difficult to investigate molecular and atomic structures in detail. Particle accelerators, particularly electron accelerators, have significantly increased the brightness of X-ray sources, however, a major step forward has been achieved with the advent of free electron lasers (FELs).

Free electron lasers, which were first proposed by John Madey in 1971, produce high-intensity, coherent electromagnetic radiation using high-energy electrons moving through magnetic structures [5]. Unlike conventional lasers that depend on electronic transitions in atoms or molecules, FELs generate light across a broad spectrum, from microwaves to X-rays, offering exceptional brightness and transverse coherence. Additionally, FELs are capable of producing ultrashort pulses of X-ray light, often on the order of femtoseconds, making it possible to capture dynamic processes that occur on extremely short time scales. This unique combination of brightness, transverse coherence, and ultrashort pulses makes FELs an invaluable tool for investigating structural dynamics at the atomic and molecular levels.

X-ray free electron lasers (XFELs) represent a significant advance in the development of X-ray sources, providing unique capabilities that are expanding the boundaries of science. XFELs are distinguished by three extraordinary properties:

1. Extreme Peak Brightness: The peak brilliance of XFEL pulses is approximately 100 million to a billion times higher than synchrotron X-rays, providing a new method for mapping atomic details and determining the composition of molecules. Scientists utilize this exceptional brightness to create three-dimensional images of viruses, cells, and nanomaterials, enabling groundbreaking discoveries in structural biology and beyond. The European XFEL, for instance, facilitates studies ranging from the mapping of virus structures to the exploration of processes occurring deep

within planets [7–9].

2. Ultrashort Pulses: XFEL pulses are impressively short, lasting only a few femtoseconds. These ultrafast temporal flashes allow researchers to capture chemical reactions in real-time, observing the formation and breaking of chemical bonds. Techniques such as "diffract-before-destroy" take advantage of these short pulses to probe samples before they are destroyed, protecting the integrity of the data and providing insights into dynamic processes at the atomic level [10, 11].

3. Transverse Coherence: The transverse coherence of XFEL pulses means that the waves of the laser light are in phase and reinforce one another, enhancing the quality and applicability of the radiation for experimental purposes. This coherence enables the development of imaging methods with higher spatial resolution and contrast sensitivity, as well as photon correlation spectroscopy methods for studying the dynamic properties of soft matter and amorphous materials. High-resolution imaging of single particles and nanomaterials, alongside the investigation of dynamic processes, is evidence of the transformative potential of XFELs. However, compared to conventional optical lasers, the longitudinal coherence of an X-ray SASE FEL is relatively poor, due to its start-up process, which is driven by random electron density fluctuations (shot noise) within the electron bunch [12, 13].

The operational XFEL facilities around the world, such as those in Germany (European XFEL in Schenefeld and FLASH at DESY in Hamburg), in Italy (FERMI at Elettra in Trieste), in the US (LCLS at SLAC in California), and in Japan (SACLA at the RIKEN Harima Institute in Hyogo), emphasize the importance and widespread adoption of this advanced technology throughout the world [1]. These facilities empower scientists to push the boundaries of knowledge, opening new possibilities in our understanding of the microscopic and ultrafast processes in the natural world.

2.2 Principle of Free Electron Lasers and SASE Radiation

The X-ray radiation generation in a FEL facility begins with the creation of electron bunches. Electrons are generated via the photoelectric effect: a cathode is illuminated by an ultraviolet laser pulse, ejecting billions of electrons per laser pulse. Each electron bunch is then accelerated to nearly the speed of light ($v \simeq c$) by high-frequency electromagnetic fields using a radiofrequency (RF) electron gun. Due to their identical negative charges, electrons within a bunch repel each other. To counteract this and maintain a compact longitudinal bunch structure, strong accelerating fields are applied. Additionally, magnetic fields produced by

solenoids (two coils surrounding the electron gun) provide transverse focusing of the electrons, ensuring they remain tightly confined. Each dense bunch typically contains approximately 10^9 electrons, and thousands of ultraviolet laser pulses per second are converted into these dense electron bunches.

The electron bunches are then injected into a linear accelerator (LINAC), where they are accelerated to high energies using radiofrequency (RF) cavities. This acceleration process produces electron bunches with a mean energy $E_e = \gamma mc^2$ and momentum $p = \gamma mv$, where $\gamma = \frac{1}{\sqrt{1-\frac{v^2}{c^2}}}$ is the Lorentz factor, m is the electron rest mass, and c is the speed of light in vacuum. The electron energy typically ranges from a few hundred MeV to several GeV, depending on the desired FEL wavelength. For the European XFEL, the electron energy can reach up to 17.5 GeV [14]. Fig. 2.1 illustrates the basic components of an FEL, including the electron gun, linear accelerator, and undulator.

Another component of the FEL system is the bunch compressor (BC), which shortens the electron bunches to achieve ultra-short temporal durations and significantly increases the peak current by exploiting the beam correlated energy spread. BC systems are specifically developed for use within the linear accelerator tunnel and are designed with an asymmetric four-dipole chicane configuration [15].

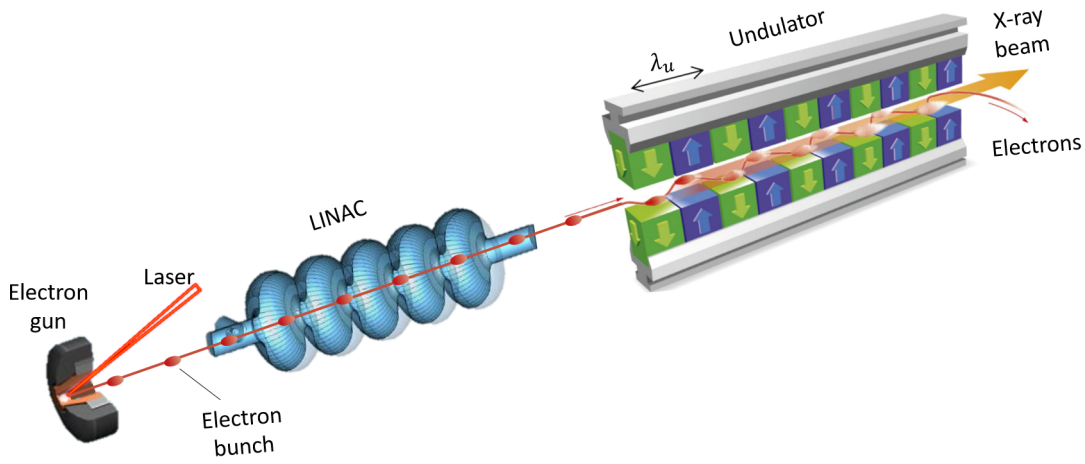

Figure 2.1: The fundamental components of a free electron laser: an electron gun, a linear accelerator, and an undulator.

Following acceleration, the electron bunches are directed into an array of undulators to generate X-ray pulses. An undulator is composed of a series of alternating permanent magnets that create a periodic magnetic field. As the relativistic electron bunches traverse this field, they undergo transverse oscillatory motion due to the Lorentz force:

$$\mathbf{F} = \frac{d\mathbf{p}}{dt} = -e(\mathbf{v} \times \mathbf{B}) \tag{2.1}$$

where $\mathbf{B}$ is the magnetic field:

$$\mathbf{B} = B_0 \sin(2\pi z/\lambda_u)\hat{y} \tag{2.2}$$

here, λ_u is the undulator period, z is the axial coordinate, and B_0 is the peak undulator magnetic field strength [1, 5, 16].

The oscillatory motion induced by the undulator causes the electrons to emit X-ray light in a process known as "spontaneous radiation". The on-axis wavelength of the radiation is:

$$\lambda(\theta = 0) = \frac{\lambda_u}{2\gamma^2}(1 + \frac{K^2}{2}) \tag{2.3}$$

where $K = \frac{eB_0\lambda_u}{2\pi mc}$ is the undulator parameter.

The key difference between XFELs and synchrotrons lies in the microbunching process (see Fig. 2.2) within the undulator section, which is approximately 200 m long at the European XFEL, depending on the beamline.

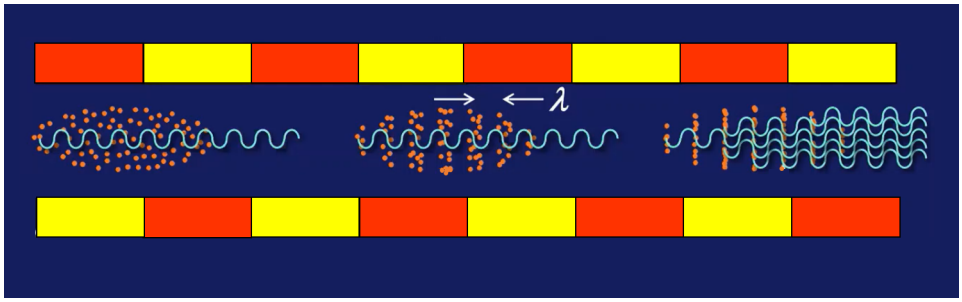

Figure 2.2: The periodic arrangement of magnets in the undulator causes the electron bunch to develop microbunching, with the distance between adjacent microbunches corresponds to the emitted wavelength, λ.

The electrons oscillate through the periodic magnetic field of the undulator (blue line in Fig. 2.3), emitting an initial wave of radiation (radiated electric field E_x), which interacts with the transverse component of the electron velocity $v_x = \frac{Kc}{\gamma} cos(\frac{2\pi z}{\lambda_u})$. This interaction introduces a feedback mechanism where the radiated field alters the electron distribution.

The energy exchange between the electrons and the electric field is described as:

$$\frac{dE_e}{dt} = \mathbf{v} \cdot \mathbf{F} \tag{2.4}$$

For a co-propagating electromagnetic wave, the electric field can be expressed as:

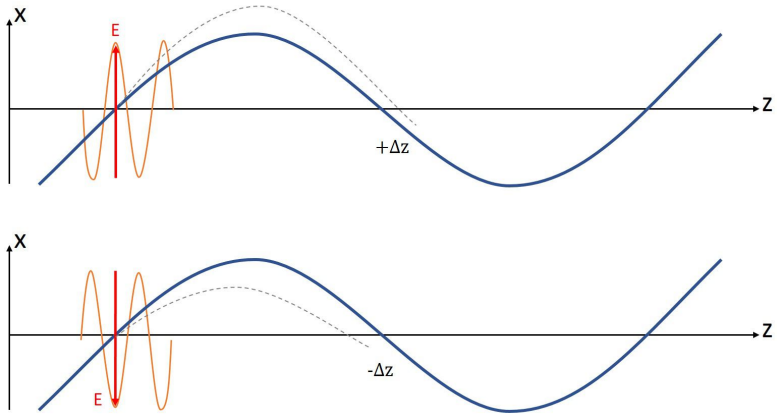

Figure 2.3: The microbunching mechanism. As the electron beam travels along the undulator in the z-direction, it oscillates transversely in the x-direction due to the periodic magnetic field. This oscillation generates an electromagnetic wave E_x (orange curve), which interacts with the transverse velocity v_x of the electrons (blue curve). The energy exchange between E_x and v_x leads to phase alignment among electrons, creating microbunches [1].

$$\mathbf{E} = E_0 \cos(kz - \omega t + \phi_0)\hat{x} \tag{2.5}$$

where E_0 is the initial electric field amplitude, $k = 2\pi/\lambda$ is the wave number of the radiation field, $\omega = kc$ is the angular frequency, and ϕ_0 is relative phase to the electron oscillation. The rate of energy exchange is expressed as:

$$\frac{dE_e}{dt} = -e\mathbf{v} \cdot (\mathbf{E} + \mathbf{v} \times \mathbf{B}) = -e\mathbf{v} \cdot \mathbf{E} \tag{2.6}$$

where $\mathbf{v}\cdot(\mathbf{v}\times\mathbf{B})$ is identically zero by vector theorem. Substituting the transverse velocity (v_x) and radiated field (E_x) terms, the energy exchange becomes:

$$\frac{dE_e}{dt} = -\frac{eE_0Kc}{\gamma} \cos(k_u z) \cdot \cos(kz - \omega t + \phi_0) \tag{2.7}$$

Using the trigonometric expression $\cos A \cos B = \frac{1}{2}[\cos(A-B) + \cos(A+B)]$, this simplifies to:

$$\frac{dE_e}{dt} = -\frac{eE_0Kc}{2\gamma}(\cos(\psi) + \cos(\chi)) \tag{2.8}$$

$$\psi = (k + k_u)z - \omega t + \phi_0 \tag{2.9}$$

$$\chi = (k - k_u)z - \omega t + \phi_0 \tag{2.10}$$

The dynamics of this energy exchange are characterized by two phases, ψ and χ. The ψ term varies slowly over many undulator periods, leading to a continuous

unidirectional energy exchange, whereas the χ term varies rapidly.

The first term in Eq. 2.8 will provide a continuous energy transfer if $\cos(\psi)$ is positive and remains constant along the entire undulator (i.e. independent of time), with the optimum phase being $\psi = 0$ or $\psi = \pm n2\pi$. The electrons move along the undulator with an average longitudinal velocity $z(t) = \overline{v}_z t$ and get

$$\psi = (k + k_u)\overline{v}_z t - \omega t + \phi_0 = const \tag{2.11}$$

or

$$\frac{d\psi}{dt} = (k + k_u)\overline{v}_z - kc = 0 \tag{2.12}$$

The condition $\psi = const$ can only be fulfilled for a certain wavelength, which is exactly the same as the light wavelength observed in undulator radiation. This fact is the reason why spontaneous undulator radiation can serve as seed radiation in an FEL (for the detailed calculation one can see Ref.[5]).

$$\lambda_{res} = \frac{\lambda_u}{2\gamma^2}(1 + \frac{K^2}{2}) \tag{2.13}$$

Depending on the relative phase of the electrons to the co-propagating wave, some electrons gain energy from the radiation field while other electrons lose energy, leading to their acceleration or deceleration. If Eq. 2.12 is satisfied, the energy exchange oscillates rapidly according to $\cos(\chi)$ around $\cos(\psi)$. In regions where $\theta = \psi + \pi/2$ falls within specific ranges, depending on their phase, electrons will either gain or lose energy:

- $-\pi < \theta < 0$: Electrons gain energy from the field.
- $\theta = 0$: The average energy exchange is zero.
- $0 < \theta < \pi$: Electrons lose energy to the field.

Since the electron bunch is much longer than the radiation wavelength, all phases θ are initially uniformly populated. This uniform distribution leads to a periodic sequence of regions where electrons (on average) gain or lose energy along the bunch. Despite the local energy exchange, the net energy transfer remains zero, as the number of electrons gaining energy equals those losing energy.

As the electron bunch travels through the undulator, it develops a periodic *energy modulation* due to this energy exchange. After a certain undulator distance, this energy modulation evolves into a *density modulation* as electrons shift their longitudinal positions.

This energy modulation alters the resonance condition for $\theta = \text{const}$, causing a non-uniform phase shift $\frac{d\theta}{dt}$ along the bunch. Consequently, the uniform phase

distribution transforms into a non-uniform one. Thus electrons begin to develop a reduced charge density in some axial positions and an increased charge density in others. This process initiates microbunching within the larger electron bunch.

As the electrons travel further through the undulator, this microbunching intensifies. Regions with higher electron density facilitate a stronger interaction with the electromagnetic field, enhancing the net energy transfer. The electron bunch progressively loses its average energy, while the radiation intensity grows exponentially along the undulator.

This feedback process amplifies the electron density modulation and the emitted radiation power until saturation is reached, characterized by maximum peak power and transverse coherence.

This mechanism, where lasing begins with *spontaneous emission* of undulator radiation driven by random density fluctuations and transitions into exponential growth of density modulation and transverse coherent radiation, is known as *Self-Amplified Spontaneous Emission* (SASE) [1, 4, 5, 17, 18].

The evolution of radiation in a FEL can be summarized in three distinct regimes: linear growth, exponential amplification, and saturation.

Linear Growth: In a short undulator, the emitted radiation is known as spontaneous radiation, and its power scales with N_e, the total number of electrons in the bunch. For short distances, the radiated energy grows linearly with the undulator length. This is the initial stage where the interaction between the electrons and the radiated field is weak, and the electron density remains randomly distributed.

Exponential Amplification: As the electrons continue through the undulator, their density modulation increases due to energy exchange between the radiated electric field and electron. This phenomenon, known as microbunching, aligns more electrons in phase with the emitted radiation, leading to coherent emission. The radiated field grows proportionally to the number of participating electrons, N_e, and the radiated power scales as N_e^2, results in exponential growth. As illustrated in Fig. 2.4, the radiated power transitions from linear growth to exponential amplification. During this stage, the initially random distribution of electrons becomes increasingly organized into well-defined microbunches, with more electrons contributing to the coherent emission.

Saturation: The process ends in the saturation regime, where the electron bunch reaches maximum density modulation. At this point, the radiated power and transverse coherence are at their highest levels. Further passage through the undulator does not enhance the radiation.

In the end, the electrons are no longer needed and are captured by an "electron dump". Bending magnets guide the electrons into a chamber beneath the tunnels, where they enter tubes filled with graphite to safely absorb their remaining energy.

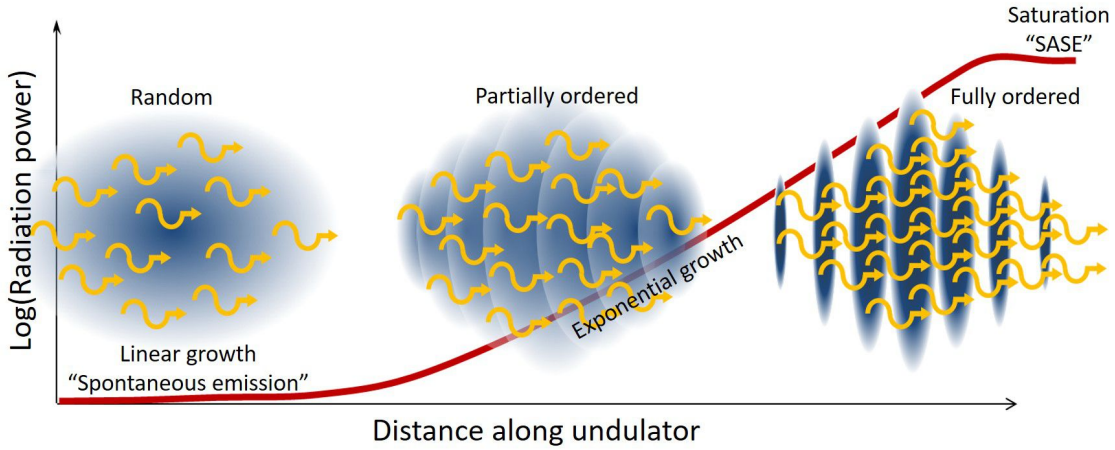

Figure 2.4: Power gain curve for an XFEL. 1. No density modulation within the electron bunch. 2. Emergence of density modulation and exponential growth of radiated power 3. Saturation characterized by nearly full electron density modulation, maximum radiated power, and full transverse coherence.

2.3 European XFEL

The European X-Ray Free Electron Laser (European XFEL) is an advanced X-ray research facility commissioned in 2017. The facility is located underground and extends over 3.4 kilometers (Fig. 2.5) [19, 20].

It starts with an electron injector made of cesium telluride (CsTe2) at DESY in Bahrenfeld-Hamburg. This injector produces and injects electrons into a 1.7 km-long linear accelerator with superconducting RF cavities, accelerating them to an energy of up to 17.5 GeV. The use of superconducting acceleration elements developed at DESY allows for up to 27,000 repetitions per second. This increase in energy is achieved through a sequential series of structures called cavities, made of niobium (Nb), which becomes superconducting at ultra-low temperatures. The European XFEL accelerator cavities are cooled to -271°C using liquid helium. Afterward, accelerated electrons are introduced into undulators and follow zigzag trajectories, resulting in the emission of X-rays with wavelengths ranging from 0.05 nm (SASE2) to 4.7 nm (SASE3) [22]. These X-rays travel through 1 km-long photon-transport tunnels equipped with various X-ray optics elements, finally arriving at the experimental hall of the European XFEL headquarters in Schenefeld. Here, the experimental stations, laboratories, and administrative buildings are located.

During normal operation, the European XFEL generates up to 27,000 bunches per second, significantly more than the 60 to 120 bunches produced by other XFELs. The bunches are arranged into 10 trains per second, each containing 2,700 bunches, with a time separation between bunches of 222 ns, which corresponds to a frequency of 4.5 MHz [23]. Fig. 2.6 displays the pattern and timing of the bunch trains.

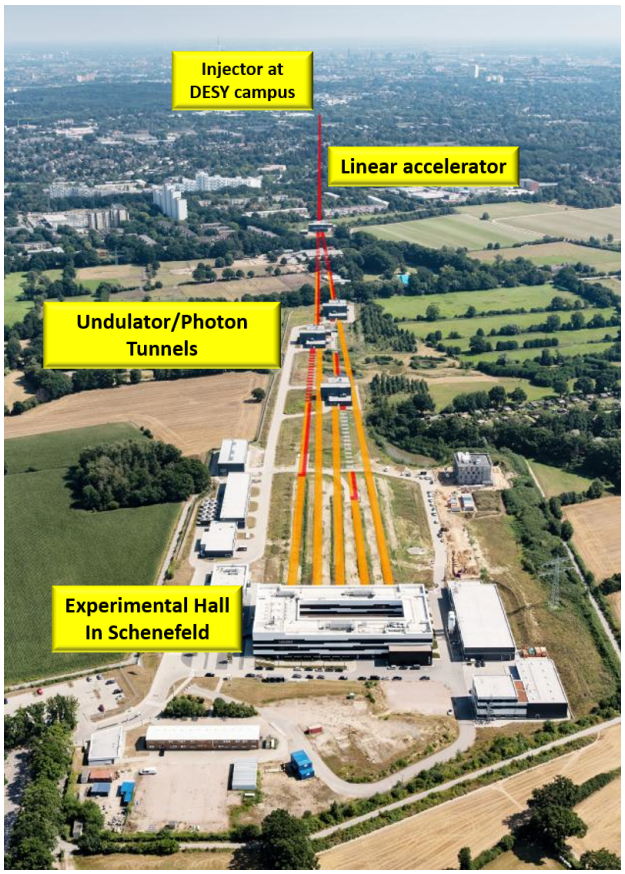

Figure 2.5: Aerial view of the European XFEL[21].

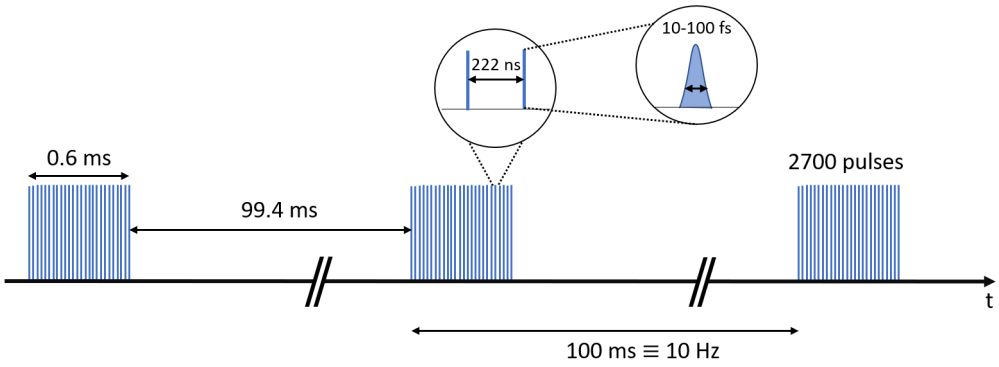

Figure 2.6: X-ray pulse pattern of European XFEL.

The X-ray pulses produced by the European XFEL are shorter than those from most other X-ray sources. The high pulse energy and femtosecond duration (10 - 100 fs) of the X-ray pulses, along with their coherence, provide entirely new research opportunities, such as structural studies of individual biomolecules, which are not feasible with current third-generation light sources [5]. During the past year, this multinational and multidisciplinary facility delivered 4896 hours of accelerator time for user experiments.

2.3.1 SQS Beamline

The European XFEL operates three self-amplified spontaneous emission (SASE) branches, designated as SASE1, SASE2, and SASE3. SASE1 and SASE2 provide hard X-ray radiation, covering the range from approximately 3 keV to 25 keV, while SASE3 produces soft X-rays at energies ranging from roughly 250 eV to 3 keV. Each SASE is significantly longer than the saturation length, enabling special modes of operation, such as self-seeding for the hard X-ray undulators and two-color operation at SASE3 [24–28]. Currently, the European XFEL possesses seven instruments in its underground experimental hall: two for SASE1, two for SASE2, and three for SASE3. Each instrument is optimized for specific experimental purposes and is permanently assigned to one of the facility's beamlines to meet the unique requirements of different experiments. One of the key instruments at SASE3 is the Small Quantum Systems (SQS), which is dedicated to investigating fundamental light-matter interactions on isolated species in the gas phase, including atoms, molecules, ions, and nanoparticles in the soft X-ray regime.

Research at SQS primarily focuses on non-linear phenomena such as multiple ionization and multi-photon processes, as well as time-resolved experiments following dynamic processes on the femtosecond timescale. Coherent scattering techniques are also employed to study larger systems, such as ions, clusters, nanoparticles, and large biomolecules. The use of soft X-rays facilitates precise control of electronic subshell excitations in atomic targets and enables site- or element-specific excitations in molecular systems.

One notable kind of experiment conducted at SQS is the two-color pump-probe experiment. In these setups, high-intensity X-ray pulses drive the system into highly excited states or initiate non-linear X-ray processes, while synchronized optical laser pulses manipulate electronic states and nuclear dynamics. Probing the interaction of the X-ray FEL with the sample is achieved through either direct coherent X-ray scattering to obtain structural information or through various spectroscopic techniques based on electron, ion and fluorescence detection.

The SQS instrument specifications include a photon energy range from 250 eV to 3000 eV, a tunable focus size between 1 and 3 µm, and a pulse duration of 25 fs under normal operation. Polarization is currently horizontally linear, additionally, linear horizontal, vertical or circular polarization will be operational following the commissioning of APPLE-X undulators in 2025. The number of pulses per train is adjustable, with up to 300 pulses at a repetition rate of 1.1 MHz.

The beam transport system at SQS allows for the use of either the direct beam from the variable-gap SASE3 undulator or a reduced-bandwidth beam from the soft X-ray grating (Fig. 2.7) [29]. A Kirkpatrick–Baez (KB) bendable high-polished

mirror system ensures precise focusing, capable of reducing the beam to spot sizes as small as 1 µm. Various diagnostic devices are installed both upstream and downstream of the interaction regions to monitor key FEL radiation properties, such as pulse energy, pulse duration, arrival time, spectral distribution, and focal spot size, ensuring precise control throughout experiments.

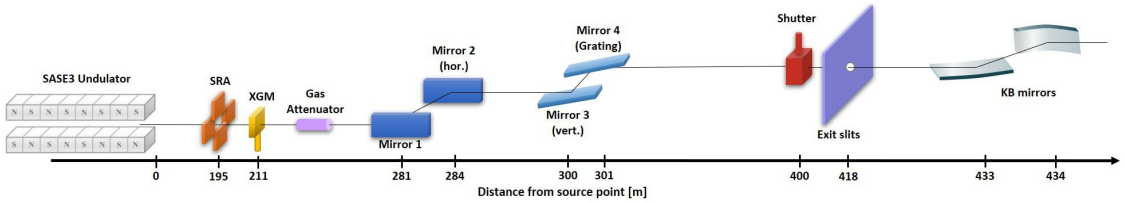

Figure 2.7: Beam transport layout for the SQS branch of the SASE3 beamline (out of scale).

2.3.1.1 SQS Bendable Kirkpatrick–Baez (KB) Mirrors

One of the key optical components in the SQS instrument is the Kirkpatrick–Baez (KB) mirror system, which can focus X-rays to very small spots, often down to the micrometer scale. Since KB mirrors play a critical role in both our simulations and experiments, and will be discussed further in subsequent chapters, we introduce them briefly here.

A KB system consists of two crossed, elliptically shaped mirrors, as shown in Fig. 2.8. Each mirror surface is polished to an elliptical shape, designed with the first focal point at the radiation source, such as the undulator exit, and the second focal point at the sample position. Because manufacturing ellipsoidal surfaces with two principal curvature planes is challenging, each mirror is curved only in one plane, and the two are arranged perpendicular to each other [30].

The geometry of a KB mirror system is based on an elliptical shape, with the ellipse described by the relation $\frac{z^2}{a^2} + \frac{x^2}{b^2} = 1$, as shown in Fig. 2.9. The dimensions of the ellipse are defined in terms of the grazing incidence angle θ and the distances p and q from the center of the mirror to the source point and the focal point, respectively, where $a = \frac{1}{2}(p+q)$ represents the semimajor axis, and $b = [a^2(1-e^2)]^{\frac{1}{2}}$ represents the semiminor axis. The eccentricity e is given by $e = \frac{1}{2}2a[p^2 + q^2 - 2pq\cos(\pi - 2\theta)]^{\frac{1}{2}}$ [32, 33].

The design parameters for each mirror (p, q, θ) are tailored to the specific beamline requirements or experimental application. The SQS KB mirror system consists of two approximately 1-meter-long bendable mirrors, allowing for adjustments in beam size and focal position. Both the VKB (vertically focusing Kirkpatrick–Baez) and HKB (horizontally focusing Kirkpatrick–Baez) mirrors operate at a nominal

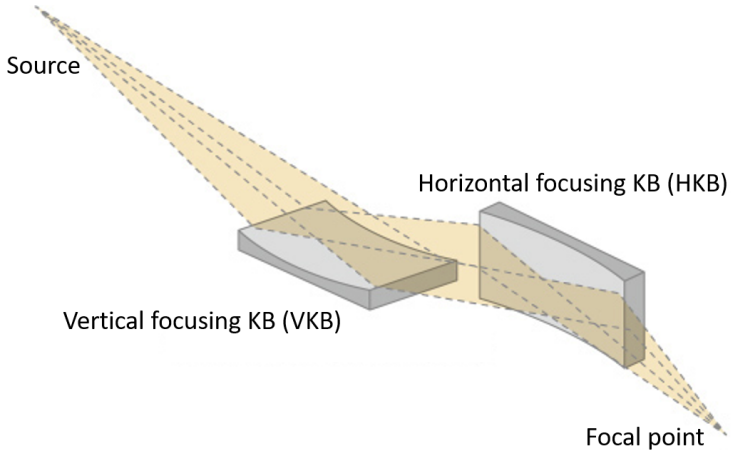

Figure 2.8: Schematic of KB focusing geometry, illustrating a vertically focusing (VKB) and horizontally focusing (HKB) KB mirror arrangement [31].

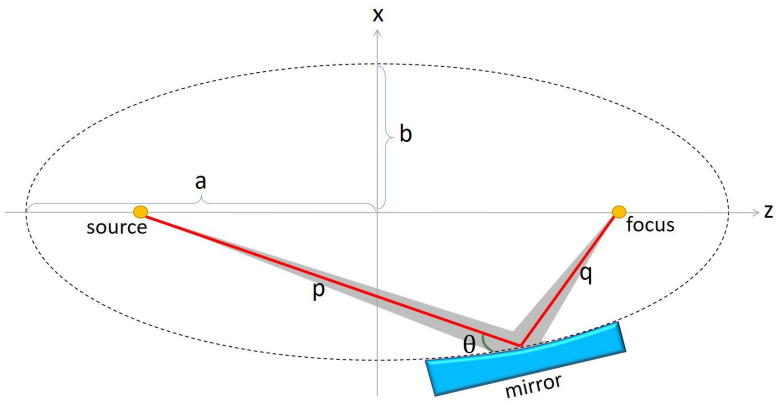

Figure 2.9: Elliptical mirror geometry, illustrating the semimajor axis a, semiminor axis b, source-to-mirror distance p, focal length q, and grazing incidence angle θ.

grazing angle of 9 mrad. This angle provides reasonable geometric transmission and high reflectivity for photon energies up to 3 keV, achieved with a B_4C coating [29, 34].

For example, in the SQS instrument, the VKB mirror is configured for a source distance p =432.7308 m, a focal length q =3 m. The HKB mirror, meanwhile, has parameters of p =433.9308 m, q =1.8 m. These parameters are adopted for the simulations described in the following chapters.

CHAPTER 3

Optical Delay Line

3.1 Motivation and Pump-Probe Experiment

An essential technique for investigating electron and nuclear dynamics in quantum systems is the pump-probe experiment. This method is vital for scientists aiming to understand chemical reactions and how molecules work in complex ways. Femtosecond pump-probe spectroscopy, whether in condensed matter, gas phase, or liquid, has led to significant advancements in biology, chemistry, and materials science [35–46].

In a typical pump-probe experiment, the first pulse acts as the pump, while the second serves as the probe. Because of their differing energies and wavelengths, this experiment is also known as a two-color experiment. The procedure begins with an intense pump pulse that excites the system, promoting a molecule to a higher energy state and thereby driving the system into a non-equilibrium state. This excitation may involve transferring electrons from bonding to anti-bonding orbitals, consequently weakening atomic bonds. The excited molecules can undergo various subsequent processes, such as vibrations, relaxation, or dissociation. Scientists are particularly interested in the events that occur after the pump pulse. The second pulse, known as the probe, detects changes in the molecule electronic and nuclear structure and dynamics resulting from the pump interaction. In these widely utilized experiments, the pump pulse initiates a non-equilibrium process in the excited or ground state of the system, while the delayed probe pulse keeps track of the time evolution of system. By extending the pump-probe technique to subfemtosecond timescales, we can probe the motion of valence electrons within quantum systems [41, 45].

In many cases, the pump source is an optical laser, such as UV or IR, while the probe is an X-ray source. This combination facilitates the understanding of complex chemical phenomena in the condensed phase, particularly with the advancements in high-intensity, commercially available, and tunable ultrafast laser systems [37]. Following photoexcitation with an optical pump pulse, X-ray absorption and emis-

sion spectra of ultrafast photochemical processes can be measured. Additionally, optical-pump X-ray-probe experiments allow for the measurement of coherently coupled electronic and atomic motions, as well as ultrafast electron delocalization in complex photochemical phenomena [36, 42, 43, 45–50].

However, a significant limitation of this approach is that femtosecond optical and IR spectra are only sensitive to valence charge distributions at specific atomic sites. Recent advancements in generating tunable, high-intensity, time-delayed, femtosecond X-ray pulse pairs have been achieved at various XFEL facilities worldwide. These technological innovations have made it possible to conduct X-ray-pump X-ray-probe experiments that study nuclear and electronic dynamics at different atomic sites in small molecules, utilizing various electron ionization detection schemes. Two-color X-ray photon correlation techniques have been applied to measure non-equilibrium structure correlations over short length scales in both solutions and solids. When either the pump or probe pulse is tuned to X-ray wavelengths, the interaction with highly localized core-level electrons is significantly enhanced, making it possible to determine the density of electrons at specific atomic sites. This technique is routinely applied to track photo-induced chemical and material transitions on femtosecond timescales [35, 37, 40, 44, 51–53].

As an illustrative example, consider a halogenated polyethane (PE), denoted as $IC_nH_{2n}Cl$, consisting of a carbon chain with chlorine and iodine atoms attached (see Fig. 3.1). The pump pulse can be tuned to approximately 630 eV to specifically target the iodine atom, creating a core hole (3d) by removing an electron. At this energy, the photoionization cross-section at the iodine site is over ten times higher than the chlorine site [54–56].

Following ionization of the iodine atom, electronic relaxation occurs via Auger decay, generating a positive charge at the iodine site. In cases of multi-photon processes leading to multiple ionization, the positive charge accumulation at the iodine site can be even higher. This buildup of positive charge triggers electron rearrangement and charge transfer processes, which can be monitored by the probe pulse.

The probe pulse, tuned to approximately 250 eV, enhances ionization at the chlorine site. This adjustment modifies the local charge surrounding the chlorine atom, affecting its electron binding energy (2p). By measuring the electrons emitted from the chlorine atom at various time intervals, researchers can track the movement of charge through the molecule, monitoring charge redistribution and electronic rearrangements in response to the initial ionization.

The local charge at the chlorine site changes based on charge propagation during the pump-probe delay, which is reflected in the variations in chlorine electron binding energies. Monitoring electron emissions within energy ranges specific to the chlorine

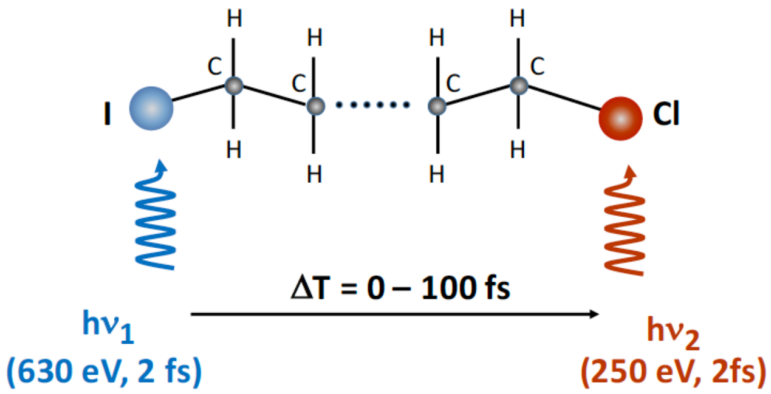

Figure 3.1: Structure of $IC_nH_{2n}Cl$, showing selective ionization of iodine at 630 eV and chlorine at 250 eV for charge dynamics studies based on Ref. [54–56].

atom enhances the probe site selectivity.

At longer timescales, molecular fragmentation can occur, enabling the examination of the resulting fragments and allowing the probe to investigate fragments containing chlorine. The absorption of probe photons by these fragments may produce effects distinct from those observed when photons are absorbed by the intact parent molecule, including more pronounced secondary fragmentation. Consequently, a two-color, time-dependent study can provide insights into both charge migration and the dynamics of radiation damage propagation.

Given the high number of X-ray pulses—up to 27,000 per second—researchers can capture a wealth of data. By correlating electron emissions with specific ion fragments, they can gain deeper insights into molecular behavior. The experiment is capable of measuring extremely short timescales (on the order of femtoseconds), facilitating an understanding of how quickly information regarding changes propagates through the molecule. Selectively exciting different regions of the molecule allows for a detailed analysis of atomic interactions.

At the European XFEL, scientists aim to understand complex molecular interactions and the energy distribution throughout a molecule post-excitation. To facilitate this, modifications are made to the SASE3 undulator, including the installation of a Magnetic Chicane (MC), which deflects electrons, and an Optical Delay Line (ODL), which deflects photons, to achieve two tunable wavelengths and enable the X-ray pump X-ray probe technique. The high-intensity of XFEL pulses and high repetition rate enable scientists to capture the sequence of events in ionization and access the dynamics of this process by varying the time delay between the pump and probe, and by adjusting the power of the MC. Additionally, by altering the parameters of the undulators upstream and downstream of the MC and ODL, it is possible to tune the wavelength for each pulse, allowing excitation at well-defined atomic positions. The details of the ODL will be discussed further in this chapter.

3.2 Optical Delay Line and its Specification

To facilitate a two-color pump-probe experiment, a Magnetic Chicane (MC) was installed between the SASE3 undulators, consisting of 11 undulator cells upstream and 10 cells downstream. Fig. 3.2 illustrates the structure of the magnetic chicane.

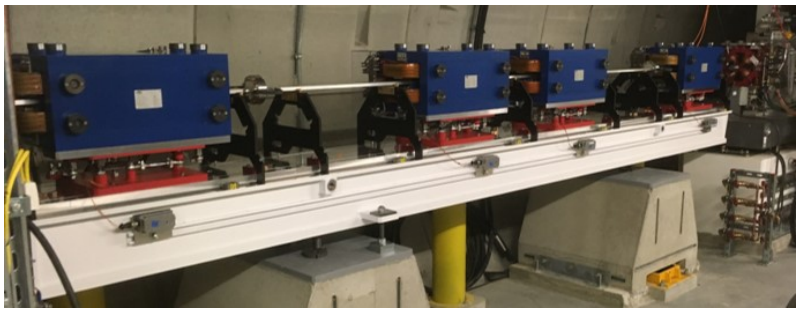

Figure 3.2: Magnetic chicane installed in SASE3, featuring four dipole magnets (blue devices shown) that horizontally deflect the electron beam.

In this setup, electrons pass through the first undulator (U1), generating the first wavelength of X-ray radiation (λ_1). This X-ray radiation then travels along the beamline while the electron bunches are deflected by the magnetic chicane, which introduces a time delay between emissions. Subsequently, the bunches of electrons enter the second undulator (U2), producing the second wavelength (λ_2) (see Fig. 3.3a). This setup enables the generation of two wavelengths with different X-ray energies.

By adjusting the magnetic chicane power, one can vary the deflection of the electrons, creating a delay in their arrival at U2. This delay can reach several picoseconds, depending on the energy of electrons. However, using only the magnetic chicane does not allow for the simultaneous overlap of photon pulses from both colors (zero time delay) or for obtaining photon pulses of color2 before those of color1 (negative delay). This limitation led to the development of the Optical Delay Line (ODL) (see Fig. 3.3b).

The ODL consists of four flat silicon mirrors coated with 50 nm of B_4C, designed to deflect photons. These mirrors will be positioned in the middle of the MC. In this configuration, electrons first pass through the undulator (U1), where the first color of X-ray radiation is generated. After exiting U1, both the electron beam and the photon pulses of color1 travel together. As the electrons pass through the MC, they are deflected horizontally by the first two dipole magnets, moving at least 3 mm away from the X-ray radiation. Simultaneously, the photon pulses of color1 are deflected vertically by the first two mirrors of the ODL and then redirected back to the main path by the last two mirrors. This arrangement introduces a temporal delay of 200 fs for the photon pulses of color1. By passing through the last two dipole

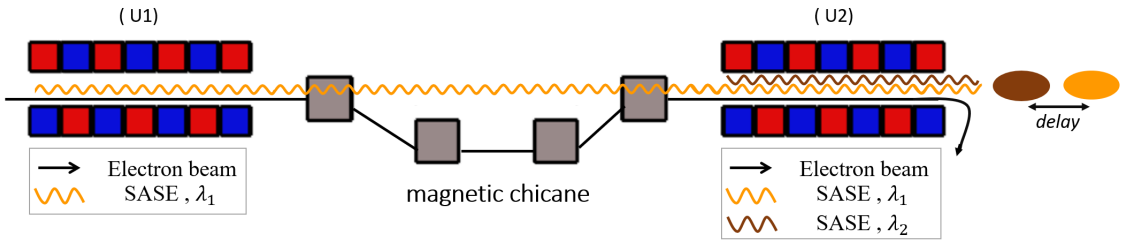

(a) With magnetic chicane.

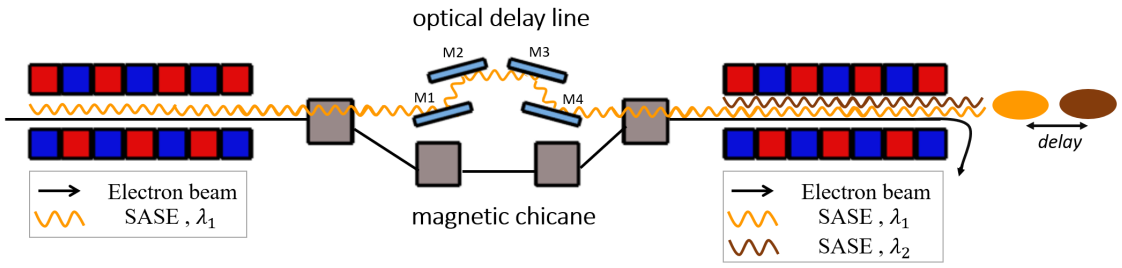

(b) With magnetic chicane and optical delay line.

Figure 3.3: Schematic illustration of a simple two-color FEL set-up with (a) magnetic chicane, (b) with magnetic chicane and optical delay line.

magnets of the MC, the electrons return to the main path, traveling alongside the photon pulses of color1. If the temporal delay for the electrons reaching U2 is less than 200 fs, they arrive earlier and generate the photon pulses of color2, resulting in a negative delay. If the temporal delays of the MC and ODL are equal, both colors will overlap. Conversely, if the temporal delay introduced by the MC exceeds 200 fs, the first color will reach the end of the beamline before the second color, resulting in a positive delay. Thus, the ODL allows for negative, zero, and positive delays. It provides a fixed negative delay of 200 fs, while adjustments to the power of the MC can modify the overall time delay.

Fig. 3.4 and Table 3.1 illustrate the orientation of the mirrors. Mirror1 (M1) and mirror2 (M2) are separated by a gap of approximately 3 mm. The dimensions of each mirror are 140 × 40 × 20 mm (length × width × thickness).

Parameter	Value
Mirror physical length, L	140 mm
Distance (M_1 to M_2), d_{12}	185 mm
Minimum optical path length	650 mm
Grazing incidence angle, θ	9 mrad
Gap, g	3.331 mm

Table 3.1: Specification of ODL.

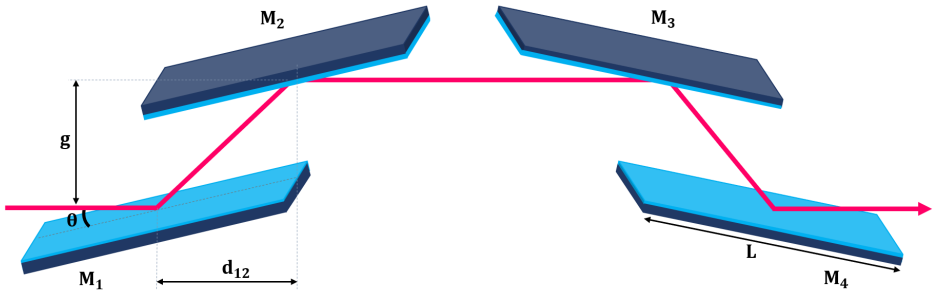

Figure 3.4: Optical delay line layout.

3.2.1 Time Delay

ODL mirrors cannot adjust the temporal delay between two wavelengths; they provide only a fixed negative delay. The temporal delay induced by the ODL can be determined by:

$$\Delta t = \frac{2g}{c(\sin(2\theta) - \tan(2\theta))} = \frac{2g}{c}\left(\frac{1-\cos(2\theta)}{\sin(2\theta)}\right) \approx \frac{2g}{c}\theta \tag{3.1}$$

Where $c = 299,792,458\,\mathrm{m/s}$ is the speed of light. The temporal delay is calculated using the gap $g = 3.331\,\mathrm{mm}$ between the mirrors and the grazing incidence angle $\theta = 9\,\mathrm{mrad}$ indicated in Table 3.1. These values can be substituted into the equation above as follows:

$$\Delta t \approx \frac{2 \times 3.331 \times 10^{-3}}{299,792,458} \times 0.009 \tag{3.2}$$

which results in a temporal delay of approximately 200 fs.

As previously described, the overall delay can be changed by adjusting the power of MC. The maximum delay of the electron beam depends on its energy. The MC displaces the electron beam horizontally, while the ODL is installed vertically to displace the photon beam along the vertical axis.

When the ODL is inserted, a minimum displacement of the electron beam is necessary to maintain a safety distance of at least 3 mm from the mechanical components and mirrors, preventing damage to the electron beam [57]. To further increase safety, an additional 2 mm of separation between the edge of the mirror and the electron beam is recommended. This results in a total minimum safety distance of 5 mm between the optical beam and the electron beam. Consequently, the clear apertures[1] of the mirrors must be positioned very close to their physical edges. The negative delay is less than 200 fs, ranging from -133 fs to 430 fs for 14 GeV, as shown in Fig. 3.5b [56]. The solid blue line represents the delay achievable using the

[1] Clear aperture refers to the specific area on the mirror surface where the reflection of light occurs.

MC without the ODL inserted. The orange line represents the delay after the ODL is inserted. Changing electron energies affects the maximum possible delay, while the minimum remains constant. Therefore, at higher energies, the maximum delay possible will be lower, while at lower energies, it will be higher (see Fig. 3.5a and Fig. 3.5c) [54, 56]. The blue curve remains accessible even if the ODL is retracted, but crossing the zero delay is not possible in this scenario.

3.2.2 Mechanical Specifications

Some motorized and manual adjustments for the ODL are implemented to achieve precise alignment of the mirrors and ensure an aligned beam spot. Each mirror allows for manual adjustments in all directions, while selected mirrors are equipped with motorized controls. Due to space limitations within the ODL setup, it is not feasible to have motorized movements for all mirrors, so we prioritize motorized control where the need for precise adjustments is critical.

The initial alignment will be carried out in the lab, but if the mirrors become misaligned during transportation or installation, the motorized adjustments allow us to correct this during the commissioning period. Given the considerable distance between the mirrors and the experimental hall, even minor misalignments can significantly shift the beam position. For this reason, achieving fine resolution in movement and rotation is essential. The selection of the motorized adjustments was decided by the availability of motors with specific resolutions and ranges in the market. The mechanical group reviewed and suggested options with better resolutions and ranges, which were then evaluated to determine whether they met the alignment requirements of the system. In the following sections, we discuss whether the resolution of these movements is adequate to maintain alignment throughout the beamline.

Mirror M1 is equipped with a motorized fine pitch rotation, achieving a resolution of 0.1 µrad and a repeatability of 0.2 µrad. Mirror M4 includes motors for pitch and roll rotation, as well as vertical movement, with a resolution of 2 µrad in pitch and roll, and 0.25 µm in vertical movement; its repeatability is 4 µrad in pitch and roll, and 0.5 µm in vertical. The fine pitch adjustment on M1 is crucial due to the significant distance of the ODL from the experimental hall, while M4 allows for coarser pitch rotations. It is only possible to manually align mirrors M2 and M3 independently. The ODL chamber is designed to support all degrees of freedom, facilitating both manual and motorized adjustments in any direction. The next section will explore the adequacy of these degrees of freedom and the mirror movements. Table 3.2 lists the motorized movements.

A pre-alignment of the ODL will be conducted in the lab prior to its installation

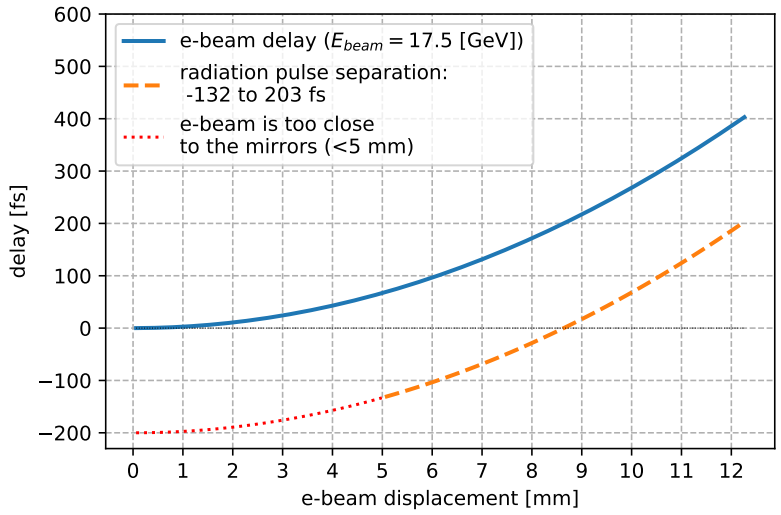

(a) $E_{\text{beam}} = 17.5\,\text{GeV}$.

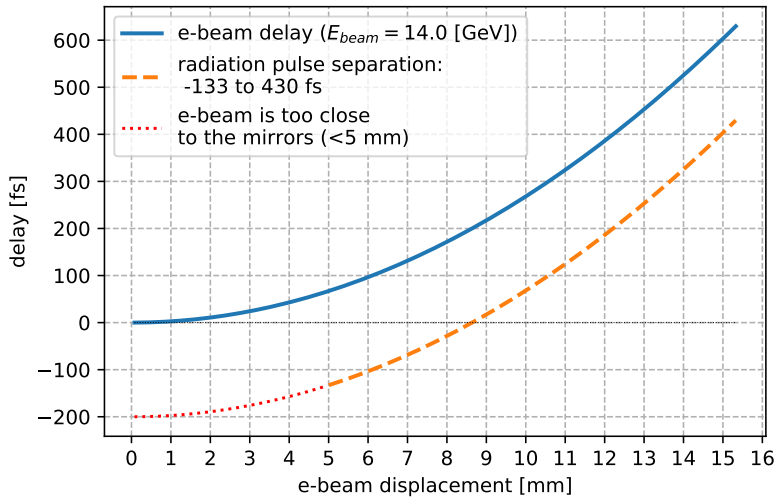

(b) $E_{\text{beam}} = 14\,\text{GeV}$.

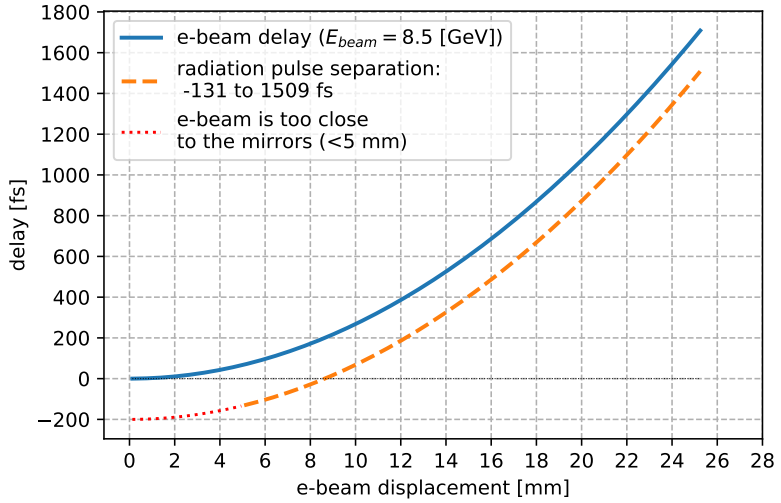

(c) $E_{\text{beam}} = 8.5\,\text{GeV}$.

Figure 3.5: Time delay achievable at different energies.

Movement	Resolution	Range
M_1 - pitch rotation	0.1 µrad	± 50 mrad
M_4 - pitch rotation	2 µrad	± 50 mrad
M_4 - roll rotation	2 µrad	± 50 mrad
M_4 - vertical movement	0.25 µm	± 2.5 mm
ODL - pitch rotation	1 µrad	± 12.5 mrad
ODL - roll rotation	4 µrad	± 12.5 mrad
ODL - vertical movement	1 µm	± 5 mm
ODL - horizontal movement	25 µm	± 12.5 mm

Table 3.2: Motorised degrees of freedom.

in the tunnel, utilizing autocollimators, laser trackers, or measuring arms for precision alignment. Diagnostic equipment will be employed for mirror alignment within the ODL. YAG screens will be installed in front of mirrors M1, M2, and M4, as well as after M4, allowing for step-by-step beam tracking and alignment of all mirrors. A series of cameras will be positioned on the side of the chamber to monitor the YAG screens, as discussed in the following sections.

For the mirror holding system, as shown in Fig. 3.6 and 3.8, a slot is designed on each side of the mirrors to hold them. Additionally, the holders can be manually adjusted to micrometer precision in the vertical direction and to hundreds of microradians in angular adjustments.

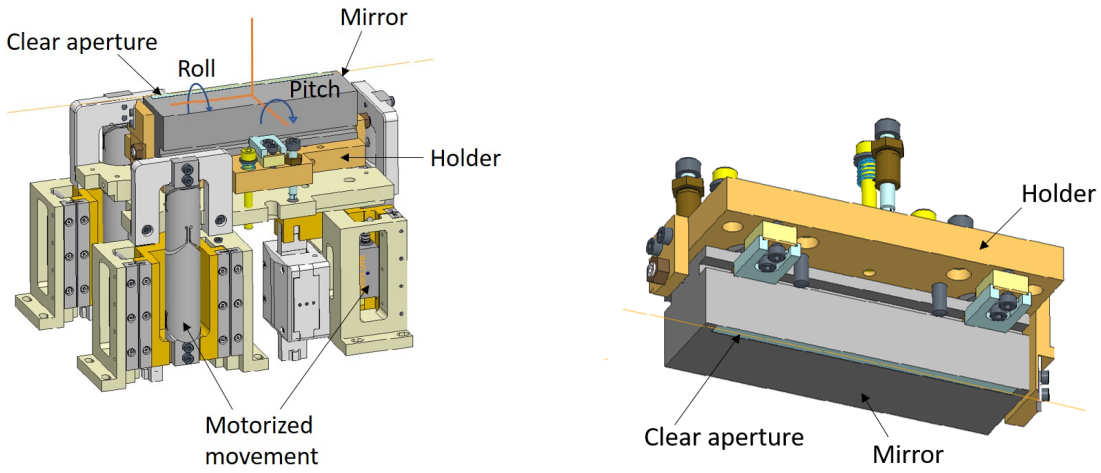

(a) M4 holder.

(b) M2 holder.

Figure 3.6: Schematic of the mirror holding system, featuring two slots designed for securing the mirrors. The left image shows the holder and mirror M4, which has motorized motion for alignment adjustments: two rotations (pitch rotation axis: perpendicular to the beam direction, roll axis: along the beam direction) and one vertical movement. The center of rotation is at the center of the mirror surface. The right image displays the holder and mirror M2. The holder components are shown in orange. Mirrors M2 and M3 are positioned upside down and, since they are fixed, do not have motorized movement. Diagram drawn by FMB-Berlin[58].

The cooling system for the first mirror is integrated into the holding system, consisting of a nickel-coated copper bar mounted 100 µm from the mirror, with the gap filled with eutectic material (see Fig. 3.8 and Fig. 3.35).

Additionally, a B_4C mask is installed upstream of the ODL to limit thermal power from spontaneous radiation on M1 and to protect the mirror and mechanics. This mask consists of two movable parts that allow the gap to be opened or closed. Another B_4C mask, which also holds a YAG screen, is located at the end of the chamber.

The mechanical components will be manufactured by FMB-Berlin, with completion expected by the beginning of 2025.

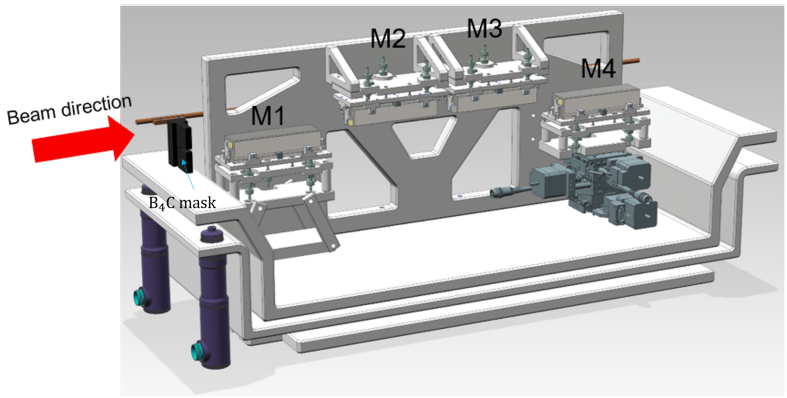

Figure 3.7: ODL mechanical conceptual design. The X-ray beam enters from the left side of the figure. Mirrors M2 and M3 are fixed. A B_4C mask is installed upstream of the ODL to limit thermal power from spontaneous radiation impacting M1, thereby protecting both the mirror surface and associated mechanical components. Drawn by M.Planas, European XFEL.

3.3 Ray-Tracing Simulation

The first pulse (source S1) is produced by the last closed cells of the upstream undulators (U1), while the second pulse (source S2) originates from the last downstream undulator cells (U2). Both pulses pass through the entire beamline, including the KB mirrors, and are focused at the sample position of the SQS instrument [24, 29]. The SQS KB-mirrors are bendable and can be adjusted to various source distances. However, only one of the two sources can be efficiently focused at the sample position. If we aim to tune KB-mirrors to image one of the two sources at one specific position, the image of the other one will be shifted to a different position in the beam direction, thus practically increasing the beam spot of the image [56]. On the other hand, the ODL is approximately 500 meters away from the sample. Thus, misalignment of a mirror in the ODL will significantly shift the focus spot.

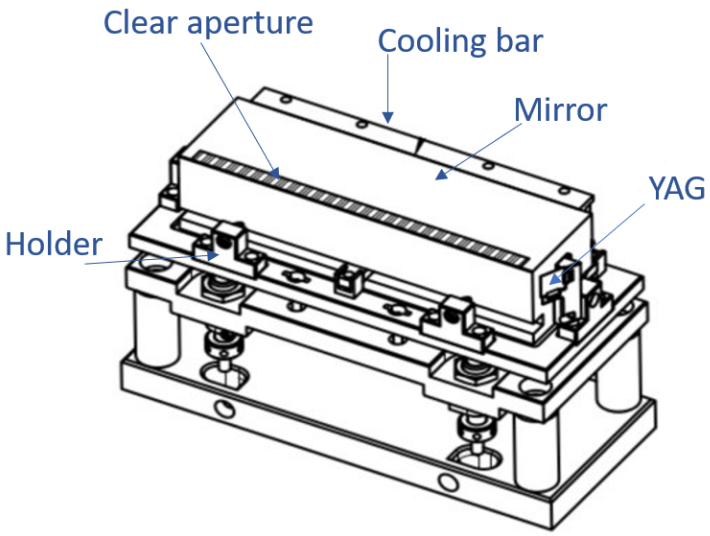

Figure 3.8: Drawing of the mirror mount for the ODL mirror. A YAG screen is mounted in front of the mirror for future alignment and beam tracking purposes. A cooled copper bar is attached to the side of the mirror to manage heat dissipation. Drawn by M.Planas, European XFEL.

Additionally, this misalignment causes the focus spot from source S1 to move away from its nominal position, raising concerns about its displacement.

We used ray-tracing simulations to track the beam path and assess how mirror movements or rotations impact the beam position and size. Modeling in COMSOL Ray Optics Module allows us to directly observe these effects, which is especially useful given the complex beamline configuration that can be challenging to calculate analytically.

The Ray Optics Module in COMSOL Multiphysics enables a ray-tracing approach that leverages Finite Element Method (FEM) implementations, commonly used for engineering problems, which can also be applied to X-ray optics [59]. Combining the Ray Optics Module with other modules in the COMSOL product suite allows ray tracing within temperature gradients and deformed geometries, enabling accurate structural-thermal-optical performance analysis within a single simulation environment—an approach that would be highly complex to implement analytically.

COMSOL Ray Optics Module was chosen because it enables seamless integration of the SQS KB mirrors, facilitating precise adjustments to their focusing parameters. This setup allows us to readily calculate the resulting focused beam position and quickly test variations in ODL mirror movements to observe their effect on beam size and focal position. The results of these simulations are reported here. The actual KB configuration of SQS was inserted, but offset mirrors and the soft X-ray monochromator were removed from the investigation. Only a perfect system will be

examined at this moment, indicating that surface errors or imperfect focusing are not taken into consideration.

Source S1 is located at a distance $x = -90\,\mathrm{m}$ with respect to S2, and the center of the ODL is placed 5 m downstream of S1 (Fig. 3.9). Table 3.3 shows all the parameters for the KB configuration with respect to SQS.

Mirror orientation	p(m)	q(m)
Vertically focusing	432.7308	3
Horizontally focusing	433.9308	1.8

Table 3.3: Parameters for KB configuration for the XFEL SQS beamline.

Ray tracing does not depend on the energy of the photon beam since all surfaces are reflective and therefore achromatic. In the ray-tracing software, the calculation is performed for the beam source size and the divergence for both sources as $S_{\mathrm{fwhm}} = 53.49\,\mu\mathrm{m}$ and $\delta\theta_{\mathrm{fwhm}} = 8.76\,\mu\mathrm{rad}$, respectively. Figures 3.10 and 3.11 show the spot size of sources S1 and S2 at the sample position ($x = 435.730\,\mathrm{m}$) based on different KB mirror configurations. In Fig. 3.10, the KB mirrors are set to focus both sources simultaneously. Using the bendable KB mirrors, it is possible to adjust both sources to a similar spot size, though slightly larger than their individual focal spots. In Fig. 3.11, the KB mirrors are configured to focus specifically on S2. This configuration, using the nominal parameters from Table 3.3, allows S2 to be at the focal position of the KB, achieving a minimal spot size. However, since S1 is not at its optimal focus position, its spot size remains larger. The KB mirror system consists of two orthogonal mirrors that focus the X-ray beams. Each mirror has a different curvature, resulting in different magnifications in the horizontal and vertical directions. This design creates an elliptical or asymmetrical beam shape rather than a circular one. Moreover, if the KB mirrors are not well-aligned or the beam is not at the focal position, aberrations occur, and the beam shape becomes imperfect [60, 61].

Table 3.2 indicates that several motorized rotations and movements are provided for the first and fourth mirrors to align the beam precisely at the center. The displacement of the focal spot at the SQS sample position due to pitch rotation on M1 is shown in Fig. 3.12a. The relationship between the pitch angle and focal spot displacement is essentially linear, with an increase in pitch of 1 µrad on M1 resulting in a shift of approximately 1.14 µm in the focal position.

Similarly, in Fig. 3.12b, the effect of roll rotation on M4 is illustrated. A 20 µrad roll rotation on M4 causes a horizontal displacement of about 0.13 µm at the sample position, and a 100 µrad roll results in a shift of approximately 0.68 µm.

Fig. 3.12c presents the displacement of the focal spot due to vertical movement on M4. Here, a vertical movement of 100 µm results in a displacement of around

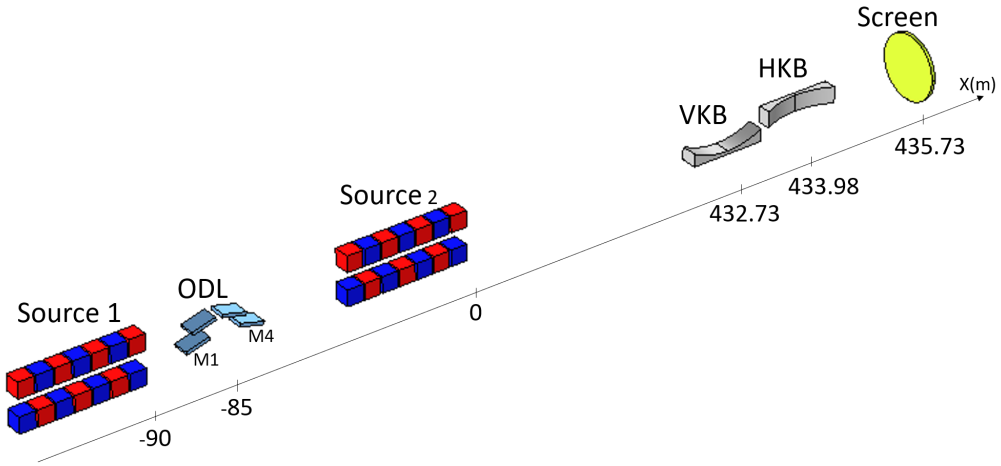

Figure 3.9: Positions of optical components in the SQS beamline.

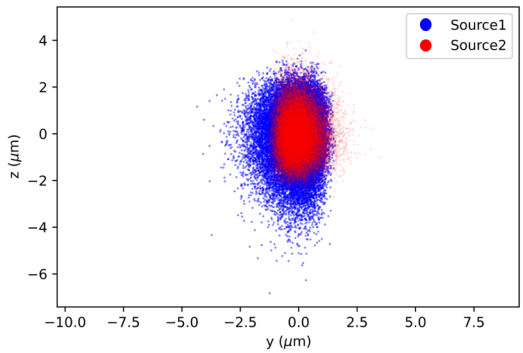

Figure 3.10: Spot size after the KB (x=435.730 m). The KB is set in order to focus both sources.

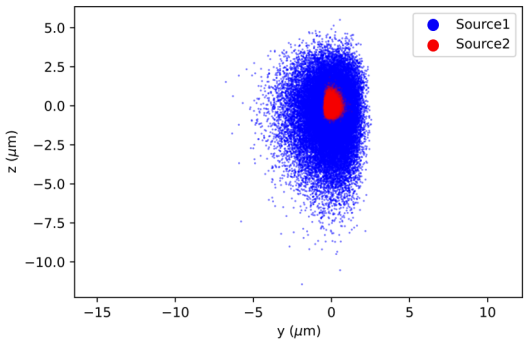

Figure 3.11: Spot size after the KB (x=435.730 m). The KB is set in order to create an image of Source 2.

1.4 µm in the beam position, while a 300 µm vertical movement leads to a displacement of roughly 4.2 µm.

Based on this analysis of how much the focused beam shifts due to the angular and positional adjustments of ODL mirrors, we can conclude that the motor resolutions listed in Table 3.2 are sufficient for precise final alignment.

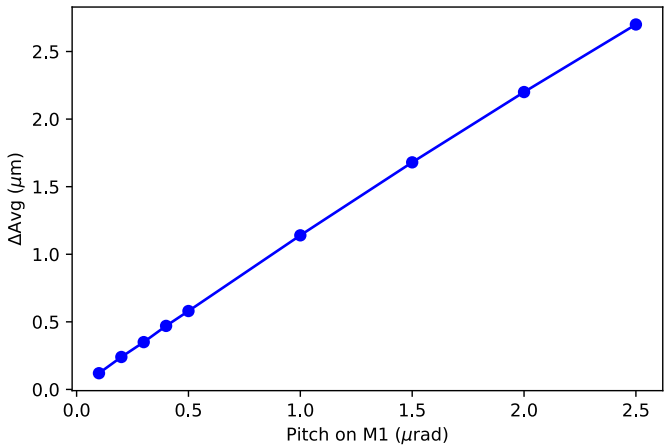

(a) Due to pitch on M1.

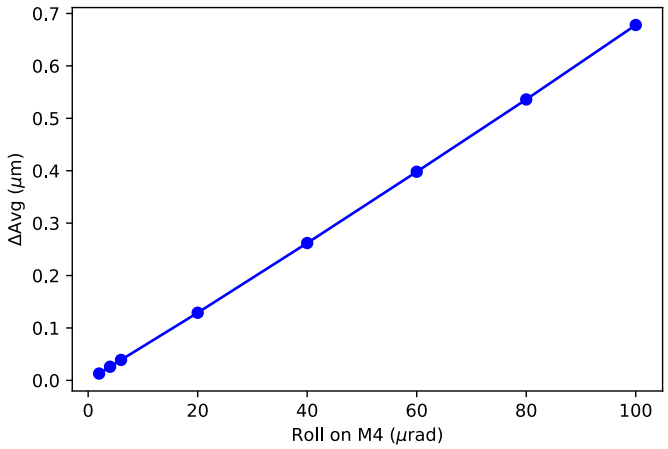

(b) Due to roll on M4.

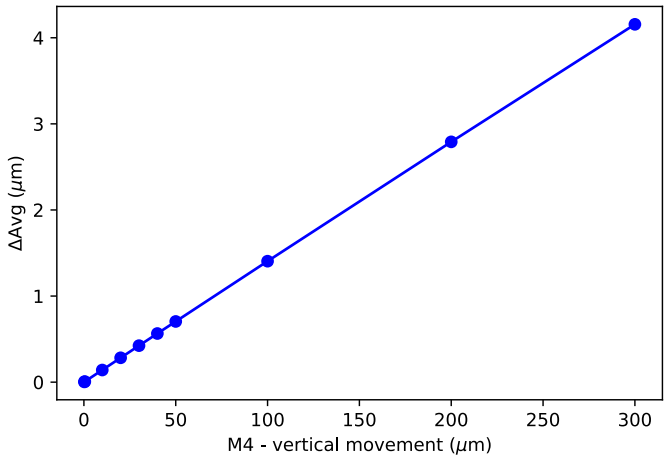

(c) Due to the vertical translation of M4.

Figure 3.12: Displacement of S1 focal spot (Δ Average spot) at the sample position.

3.3.1 Method for Aligning the Mirrors of the ODL

The ODL chamber will be installed in the middle of the MC and the undulators in tunnel SASE3 (XTD4). One critical aspect to consider is the alignment of the

mirrors, as they will be located in the electron tunnel. If the mirrors are not perfectly aligned, accessing and adjusting them will be difficult, as it would require shutting down the SASE3 undulator. Therefore, ensuring precise alignment and verifying the mechanical parts and motors before installation is essential.

The method of alignment is carefully planned and discussed in detail here. Before the mirrors are installed in the tunnel, a preliminary alignment will be performed in a clean room laboratory. FMB-Berlin, the company responsible for manufacturing the chamber, will handle the initial positioning using dummy mirrors. Following this, we will verify the positioning of the mirrors using the FaroArm in the clean room. The FaroArm, a highly flexible tool, measures the distance between two points with a precision of 10 µm to 20 µm. However, it lacks sufficient accuracy for measuring angles, with a tolerance of around 70 µrad, which is not adequate for our needs.

To ensure the angular alignment of the mirrors, both sides of the mirrors are polished to allow reflections. We will use an autocollimator for angular alignment. The autocollimator will first be fixed in place, and we will align M4 to 9 mrad, followed by M3. Once these are aligned, we will position and align M1 to 9 mrad, and finally, we will adjust M2. Alternatively, we could start the alignment process with M1, as both sides of the mirrors are polished, allowing flexibility in the alignment sequence. This process ensures that the entire system is aligned relative to one another.

The resolution of the autocollimator depends on the optical tube specifications. For this application, the misalignment tolerance must be less than 0.1 µrad in rotation, equivalent to 0.2 arcseconds. To ensure accurate alignment, the autocollimator must be capable of accommodating the gap between the upper and lower mirrors, which is 3.33 mm.

With an ODL length of about 70 mm, the autocollimator should measure at a distance of 1 meter to cover the entire setup. Given this distance, the required aperture can be calculated as follows: the 18 mrad angles in a beam spread, and with the 1-meter measurement distance, the aperture needs to accommodate this spread plus the 3.33 mm gap (see Fig. 3.13). The autocollimator aperture size is:

$$2 \times \tan(\text{deflection angle}) \times \text{distance} + \text{gap} = \text{Aperture Size}.$$

$$2 \times \tan(18\,\text{mrad}) \times 1\,\text{m} + 3.33\,\text{mm} = 39.33\,\text{mm}.$$

The field of view of the autocollimator is another parameter, as it must cover the angular range of the deflected beams. Given that the mirrors have an angular range of $2 \times 18 = 36$ mrad, this value is converted to arcseconds, since autocollimator

specifications are typically provided in arcseconds in the market.

$$36\,\text{mrad} \times \frac{180}{1000\pi} = 2.063\,\text{degrees} = 7426.8\,\text{arcsec.}$$

Therefore, the autocollimator specifications include an accuracy of 0.2 arcseconds, a clear aperture of 40 mm, and a total field of view of 3° (or approximately 7500 arcseconds), meeting the requirements for mirror alignment.

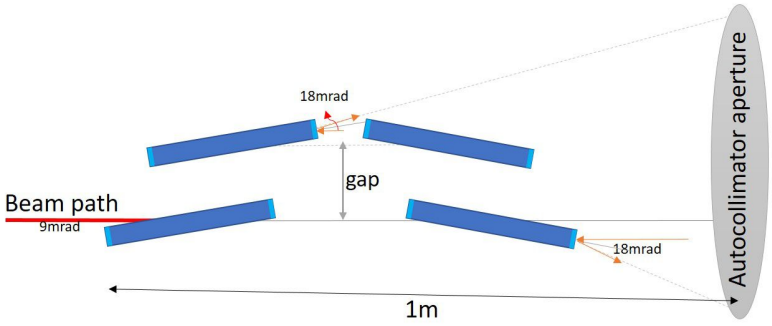

Figure 3.13: Schematic of the ODL mirror alignment setup using an autocollimator. The gap between the mirrors is 3.33 mm.

However, there is a possibility that the mirrors could become misaligned during transportation or installation. Therefore, after installation and during the commissioning period, we will fine-tune the alignment of the mirrors. During commissioning, the XRO team aligns all the mirrors and other optical elements across the beamlines.

As illustrated in Fig. 3.14, some YAG screens will be placed in front of M1, M2, and M4, and cameras will be used to visualize the X-ray beam on the YAG screens.

The alignment process will follow these steps:

- Initially, the entire ODL chamber is moved up or down until we observe the beam on the YAG screen placed in front of M1.
- Next, we adjust the chamber so that the beam reflects of M1.
- M1 is equipped with a fine pitch rotation mechanism. We rotate M1 until the beam appears on the YAG screen in front of M2.
- After confirming the beam on the M2 screen, we adjust M1 or entire ODL to ensure the beam reflects from M2. M2 and M3 are fixed in position, so the beam should then reflect from M3 to M4.
- M4 has both pitch and roll rotation capabilities, as well as vertical movement. We rotate and move M4 until the beam is visible on the M4 YAG screen. Once aligned, we lower the chamber to reflect the beam off M4.

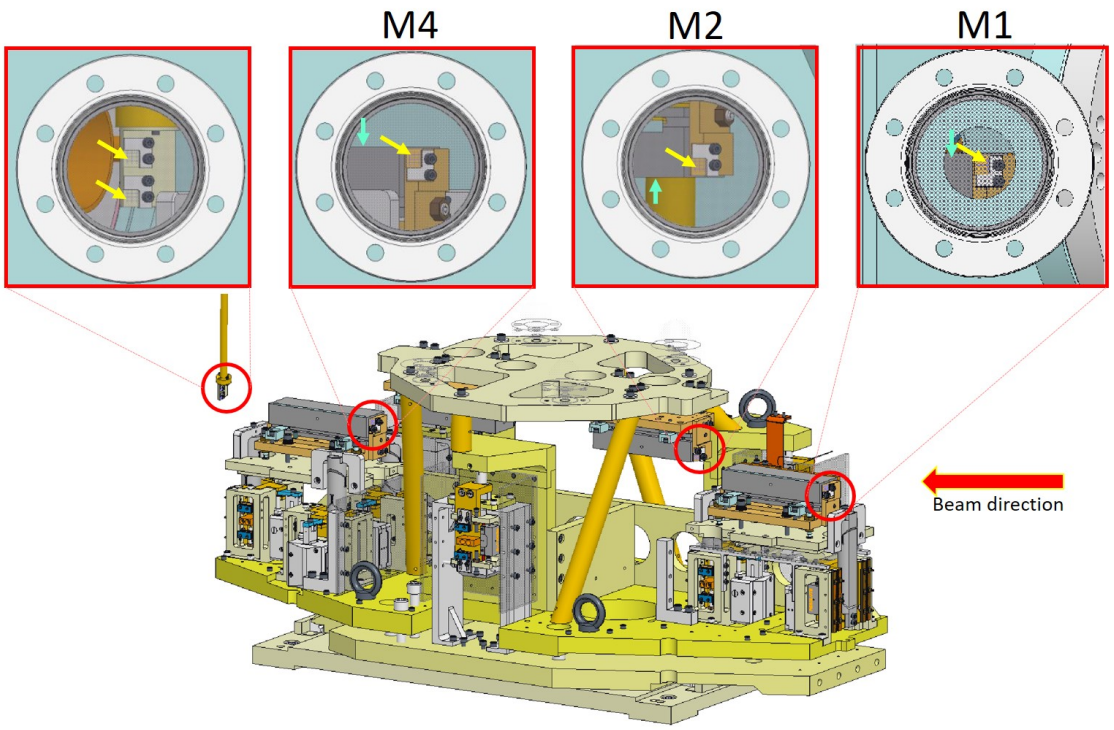

Figure 3.14: Schematic representation of the ODL mirror alignment setup. The yellow arrows indicate the positions of YAG screens, which are placed in front of mirrors M1, M2, and M4, as well as at the end of the chamber, allowing for beam tracking throughout the alignment process. Blue arrows represent the mirror surfaces. Each YAG screen has an associated camera to capture the beam image on the screen. Drawn by FMB-Berlin [58].

- Finally, we check the beam at the end of the chamber using another YAG screen positioned there.

Using the COMSOL Ray Optics Module, we simulated this alignment method to verify its feasibility. In this investigation, errors were intentionally introduced to each mirror, and they were then aligned step by step. This allowed us to evaluate the impact of misalignment on beam reflection and ensure that each adjustment would successfully align the mirrors. The method was tested in several scenarios, and one of the more challenging cases is presented here.

The initial errors were as follows:

- M1: -0.041 mm and 0.958 mrad
- M2: -0.104 mm and -1.111 mrad
- M3: 0.393 mm and 2.787 mrad
- M4: 0.019 mm and 0.563 mrad

In Fig. 3.15, the red line represents the path of the beam. The gray areas indicate the mirrors. Due to the misalignment, the beam fails to reach M3 and M4. This misalignment is evident as the red beam deviates from the mirror path after M2 and does not hit M3 as expected.

To correct this, the following adjustments were made:

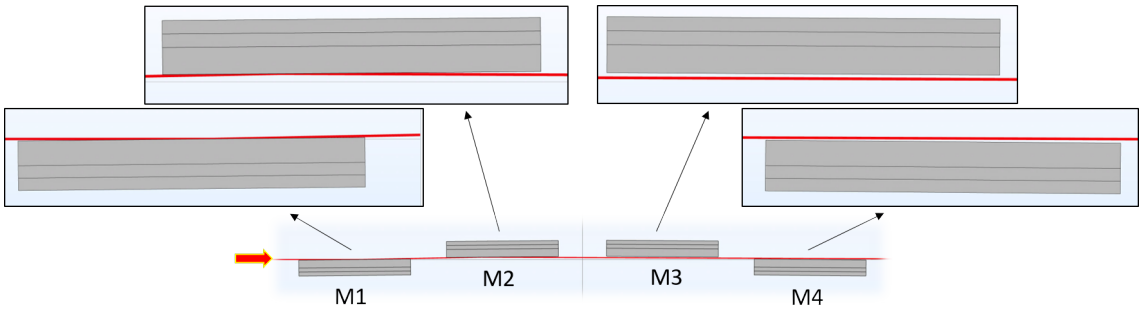

Figure 3.15: COMSOL ray-tracing simulation showing the impact of initial alignment errors on beam reflection. The beam fails to reflect from M3 and M4 due to misalignments, with corrective movements and rotations applied to restore alignment.

1. **Vertical adjustment:** The entire ODL chamber was moved down by -0.8 mm.

2. **M1 rotation:** M1 was rotated by 0.4 mrad to catch the beam on M2.

3. **Overall chamber rotation:** The entire ODL chamber was rotated by 3.5 mrad to realign the path of the beam with the mirrors.

4. **M4 adjustments:** M4 was moved by 1.75 mm and given a pitch rotation of -3.892 mrad to catch the beam correctly on its surface.

After these corrections, the beam was successfully reflected from each mirror. This alignment was observed in the simulation by the continuous red line reaching each mirror without any further deviations. The final alignment confirms that each mirror adjustment effectively brought the beam back onto the intended path. These values are approximate and serve as an example to demonstrate that the alignment process can be achieved using the available adjustments.

The 3D COMSOL simulation can be used in future alignments, allowing for easy adjustment of parameters or introduction of additional errors. This tool provides insight into how much and in which direction each mirror should be moved to achieve proper alignment.

3.4 Optical Properties

It is well known that silicon has traditionally been used as a substrate for FEL optics due to its availability, low cost, durability, and thermal stability as well as its ability to be effectively polished. As a result of recent technological advances, silicon substrates with low surface roughness with angstrom precision are now available for X-ray reflection. An elliptical or parabolic mirror is made of silicon because it has suitable mechanical properties. Silicon demonstrates strong resistance to heat load deformation and has a low coefficient of linear thermal expansion, which increases minimally with temperature, making it an ideal material as a mirror substrate [62].

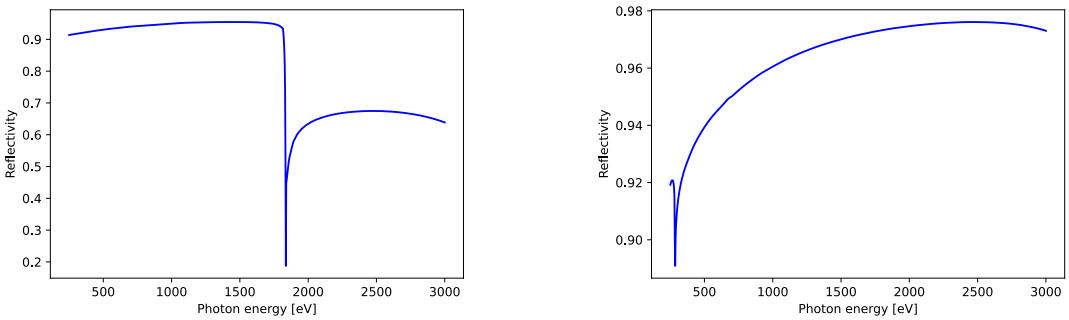

(a) Silicon.

(b) 50nm B_4C on Si substrate.

Figure 3.16: Reflectivity at 9 mrad grazing angle.

Choosing a coating material based on its reflectivity for a certain range of X-ray energies is an important factor to consider. For moderate photon energies, Boron-Carbide (B_4C) is primarily used as a protective coating, while Platinum (Pt) is mainly used for high photon energies at the European XFEL. Fig. 3.16 shows the reflectivity of B_4C and Si as a function of photon energy. The reflectivity of silicon experiences a sudden drop at 1840 eV, indicating that B_4C coating should be used for improved performance in this energy range. Additionally, B_4C has excellent thermal properties, a high melting point, low density, and a low atomic number, all of which contribute to greater penetration depth by dispersing absorbed energy over a larger area [63, 64]. Based on these properties, the material exhibits excellent damage resistance, which will be discussed in detail in the following chapter.

3.4.1 Refraction and Reflection of X-ray

Materials in the X-ray regime have complex refractive indexes, where the real part of the index is typically less than one, it is expressed as [2]:

$$n = 1 - \delta + i\beta \tag{3.3}$$

where δ is of order 10^{-5} in solid materials and only around 10^{-8} in air. The imaginary part β is usually much smaller than δ. Based on Snell law, the grazing incidence angle θ can be related to the refracted grazing angle θ' (see Fig 3.17)

$$\cos\theta = n\cos\theta' \tag{3.4}$$

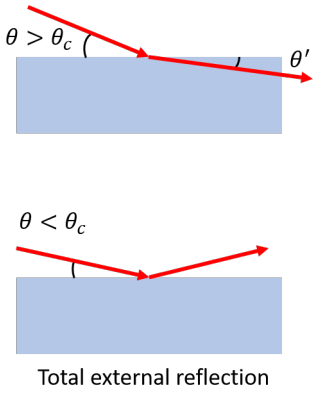

Figure 3.17: Total external reflection of X-rays at grazing angles below the critical angle due to their index of refraction being slightly less than one.

An index of refraction less than one results in total external reflection of X-rays below a certain grazing angle known as the critical angle θ_c. The critical angle can be found by setting $\theta = \theta_c$, $\theta' = 0$ and using equation (3.3) and Taylor expansion of Cosine $[\cos x \approx 1 - \frac{x^2}{2!}]$:

$$\theta_c = \sqrt{2\delta} \tag{3.5}$$

For simplicity, we will assume that β is zero. Since δ is typically around 10^{-5}, θ_c is on the order of a milli-radian. In the refracting medium, there is a phenomenon known as evanescent waves when $\theta < \theta_c$ (Fig 3.18). This wave propagates parallel to the flat interface, and it decays rapidly in the material, usually with a penetration depth of only a few nanometers. However, at an incident angle of several times θ_c, this penetration depth increases to several micrometers. Therefore, in total reflection, the reflectivity is not 100 percent and therefore a fraction of the incident light will be absorbed.

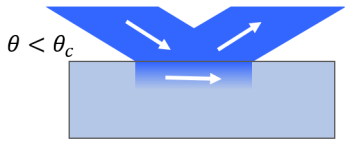

Figure 3.18: Evanescent wave.

3.4.2 Penetration Depth

Understanding penetration depth is essential for optimizing X-ray mirror performance. This parameter indicates how far X-rays penetrate into a material before being absorbed, a factor that varies with material properties, photon energy, and grazing angle. Selecting a material with an appropriate penetration depth is crucial for achieving optimal performance across specific X-ray energy ranges.

Penetration depth affects temperature distribution within the mirror, influencing its stability and durability. Accurate knowledge of this parameter aids in thermal management and ensures that mirrors are designed to withstand high radiation doses. Thus, penetration depth calculations are vital for material selection, enhancing mirror resilience, and designing effective X-ray optical systems with improved damage resistance.

The penetration depth of X-rays is calculated by the solution of Maxwell equation for a wave incident from a vacuum on a medium with a complex refractive index.

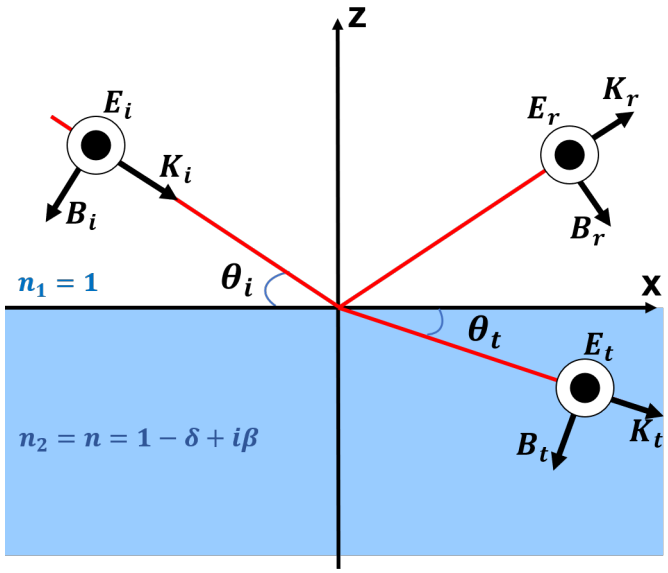

Figure 3.19: Wave vectors of incident, reflected, and transmitted waves at an interface with refractive indices $n_1 = 1$ and $n_2 = 1 - \delta + i\beta$.

For any grazing angle, the expression for the electric vector of the beam:

$$\text{Incident Beam:} \quad \vec{E_i} = \vec{E_{0i}}\, e^{-i\omega t}\, e^{i\vec{K_i}\cdot\vec{r}} \tag{3.6}$$

$$\text{Reflected Beam:} \quad \vec{E_r} = \vec{E_{0r}}\, e^{-i\omega t}\, e^{i\vec{K_r}\cdot\vec{r}} \tag{3.7}$$

$$\text{Transmitted Beam:} \quad \vec{E_t} = \vec{E_{0t}}\, e^{-i\omega t}\, e^{i\vec{K_t}\cdot\vec{r}} \tag{3.8}$$

Where $K_i = \frac{2\pi}{\lambda}$ is the incident wave vector and E_{0i} is the amplitude, as indicated in Fig 3.19. Similarly, the reflected and the transmitted wave vectors are K_r and K_t, respectively, and the amplitudes are E_{0r} and E_{0t}. The waves at the interface z=0 must be continuous. These required that the amplitudes are related by [1]

$$E_{0i} + E_{0r} = E_{0t} \tag{3.9}$$

and

$$\vec{E_{0i}}\, e^{i\vec{K_i}\cdot\vec{r}} + \vec{E_{0r}}\, e^{i\vec{K_r}\cdot\vec{r}} = \vec{E_{0t}}\, e^{i\vec{K_t}\cdot\vec{r}} \tag{3.10}$$

Consider only the transmitted beam:

$$\vec{E_t} = \vec{E_{0t}}\, e^{-i\omega t}\, e^{i\vec{K_t}\cdot\vec{r}} \tag{3.11}$$

$$\vec{K_t}\cdot\vec{r} = \hat{x}K_t\cos\theta_t + \hat{z}K_t\sin\theta_t \tag{3.12}$$

Consider just the $\hat{z}$ part, because we want to find the penetration depth through the material:

$$e^{i\vec{K_t}\cdot\vec{z}} = e^{iK_t\sin\theta_t\hat{z}} \tag{3.13}$$

The wave number in vacuum is denoted by $k = |K_i| = |K_r|$ and in the material it is $nk = |K_t|$. And from the Snell law:

$$\text{Snell law:}\quad \frac{n_1}{n_2} = \frac{\sin\alpha_2}{\sin\alpha_1} = \frac{\cos\theta_t}{\cos\theta_i} \Rightarrow \cos\theta_t = \frac{\cos\theta_i}{n}$$
$$\Rightarrow \sin\theta_t = \sqrt{1-\cos^2\theta_t} = \sqrt{1-\frac{\cos^2\theta_i}{n^2}}$$

$$\exp[iK_t\sin(\theta_t)\hat{z}] = \exp[ink\sqrt{1-\frac{\cos^2\theta_i}{n^2}}\hat{z}] = \exp\left[ik\sqrt{n^2-\cos^2\theta_i}\hat{z}\right] \tag{3.14}$$

In the X-ray wavelength region, both δ and β are very much smaller than unity, in order of 10^{-5} or less, so we can ignore δ^2, β^2 and $\beta\delta$.

$$n^2 = 1 - 2\delta + i2\beta \tag{3.15}$$

We need to separate imaginary and real part with the help of below relation:

$$\begin{aligned}\sqrt{a+ib} &= x+iy \\ x &= \pm\sqrt{\frac{\sqrt{a^2+b^2}+a}{2}} \\ y &= \pm\sqrt{\frac{\sqrt{a^2+b^2}-a}{2}}\end{aligned} \tag{3.16}$$

When $\theta \ll \Rightarrow \sin^2\theta_i \approx \theta_i^2$

$$\begin{aligned}\exp\left[ik\sqrt{n^2-\cos^2\theta_i}\right] &= \exp\left[ik\sqrt{\sin^2\theta_i - 2\delta + i2\beta}\right] \\ &= \exp\left[ik\sqrt{{\theta_i}^2 - 2\delta + i2\beta}\right] \\ &= \exp[ik(A+iB)] \\ &\text{where} \\ A &= \sqrt{\frac{\sqrt{(\theta_i^2-2\delta)^2+4\beta^2}+(\theta_i^2-2\delta)}{2}} \\ B &= \sqrt{\frac{\sqrt{(\theta_i^2-2\delta)^2+4\beta^2}-(\theta_i^2-2\delta)}{2}}\end{aligned} \tag{3.17}$$

Absorption implies that the beam is attenuated in the material over a characteristic $1/e$ length, denoted by Z_{pen}, known as penetration depth. It is important to note that this length refers to the attenuation of the *intensity*, not the *amplitude*. After traversing a distance z in the material, the intensity is attenuated by a factor of $e^{-z/Z_{pen}}$, where the penetration depth corresponds to the distance at which the intensity of the beam has dropped to $1/e$ of its initial value, meaning that approximately 63% of the photons have been stopped [2, 65].

$$I = |E_t|^2 = E_{0t}^2 e^{-2k_t B} \tag{3.18}$$

$$\begin{aligned}Z_{pen} &= \frac{\lambda}{4\pi B} \\ &= \frac{\lambda}{2\sqrt{2}\pi}\frac{1}{\sqrt{\sqrt{(\theta_i^2-2\delta)^2+4\beta^2}-(\theta_i^2-2\delta)}}\end{aligned} \tag{3.19}$$

The reflectivity can also be calculated using the same approach [2, 66, 67]:

$$R = \frac{A^2(\theta_i^2-A)^2+\beta^2}{A^2(\theta_i^2+A)^2+\beta^2} \tag{3.20}$$

Fig. 3.20 displays the penetration depth and reflectivity of B_4C at 1000 eV

photon energy as a function of grazing angle. The values were obtained from the Henke tables [68]. For angles much smaller than the critical angle given in Eq. 3.5, the mirror will be highly reflecting and the penetration depth will remain constant at about 3 nm, and it increases quickly as the angle increases beyond the critical value.

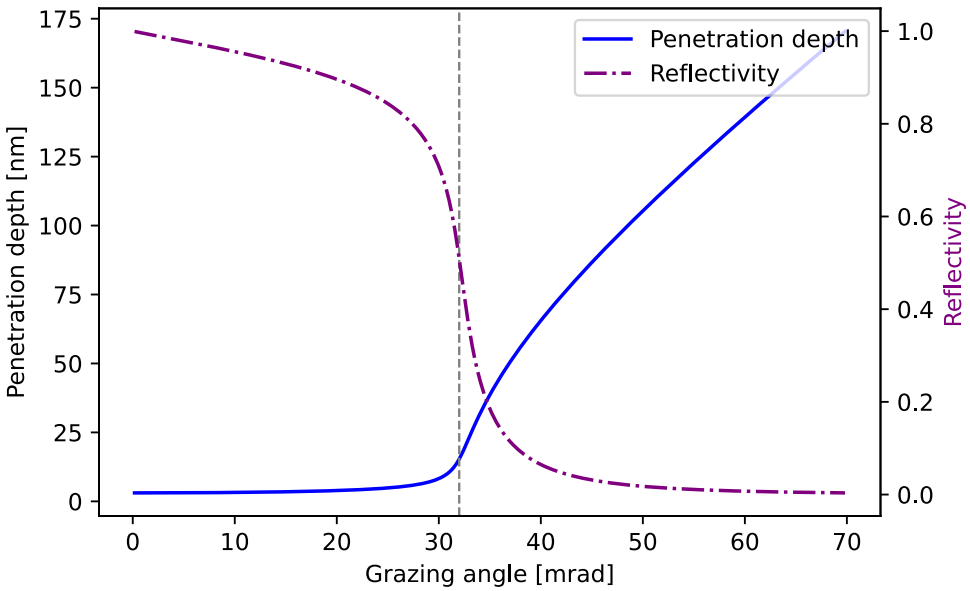

Figure 3.20: The graph displays the penetration depth and reflectivity of B_4C as a function of the grazing incidence angle for 1 keV photon energy. The critical angle θ_c is 32 mrad.

3.4.3 Grazing Incidence Angle

The SQS beamline operates in the photon energy range of 250 eV to 3 keV. Fig. 3.21a illustrates the critical angle as a function of photon energy for B_4C with a density of 2.52 g/cm^3. Based on this analysis, a fixed grazing angle of 9 mrad was selected for the ODL mirrors. As shown in Fig. 3.21b, the reflectivity as a function of grazing angle demonstrates that 9 mrad provides optimal performance across the entire photon energy range. This fixed angle ensures consistent and efficient reflection for all relevant photon energies.

3.4.4 ODL Mirrors

ODL mirrors, made of a silicon substrate, were produced and polished by ZEISS company [69].

As previously described, the mirror is designed to have an optical aperture that extends very close to the edge, allowing it to intercept photons while maintaining a

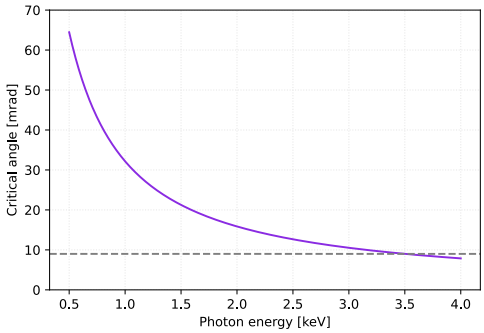

(a) Critical angle for different photon energy in B_4C.

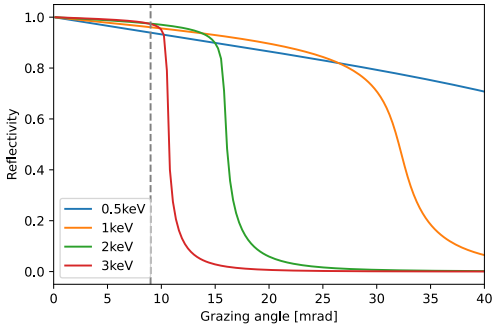

(b) Reflectivity versus grazing angle for various photon energies, for B_4C.

Figure 3.21: Demonstrating the suitability of a fixed 9 mrad grazing angle for the photon energy range of 250 eV to 3 keV.

greater distance from electrons. In order to achieve this configuration, a sharp edge must be formed between the polished surface and the adjacent side surface. This mirror is 140 mm long, and the clear aperture (6 mm wide) is directly adjacent to the sharp edge (Fig. 3.22). Initially, the mirrors are polished on larger substrates. The substrate was 10 mm larger than needed (50 mm wide) and was grinded down to 40 mm to achieve the sharp edge. The clear aperture is 6 mm, so ZEISS created a 16 mm clear aperture, polished it, and then cut 10 mm to achieve a sharp edge. The radius of curvature is more than 262 km [70].

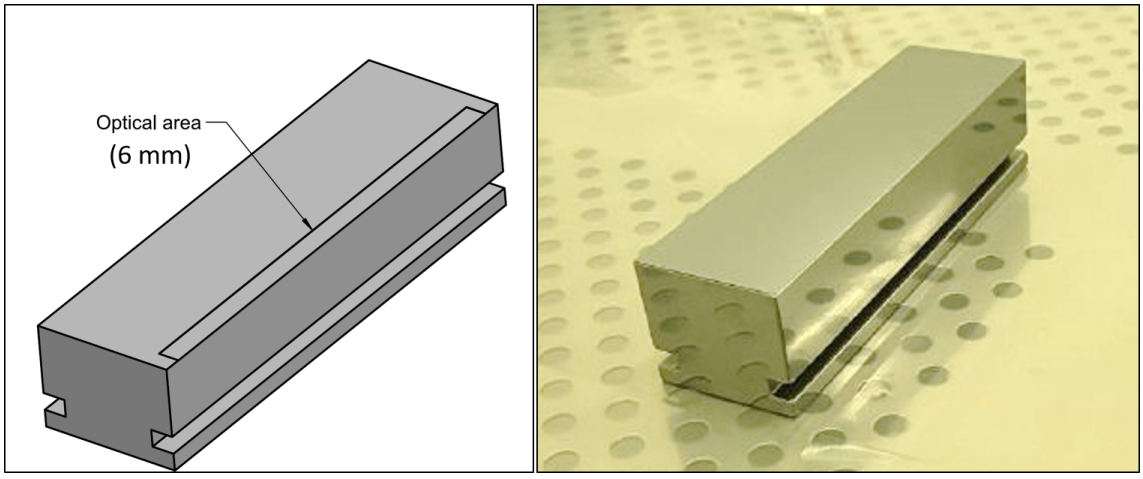

Figure 3.22: ODL mirror.

As part of the optical alignment of ODL, both lateral surfaces are polished in order to serve as a reference for alignment using an autocollimator in the future.

Mirror substrates are cleaned by applying a gentle nitrogen flow to them at the European XFEL. Afterward, the mirrors are coated with a 50 nm B_4C layer at the Helmholtz-Zentrum Hereon in Geesthacht, Germany. The B_4C coating is deposited on the entire reflecting surface of the mirrors using the 4.5 m-long Hereon magnetron

sputtering facility, which provides a deposition length of up to 1500 mm. An X-ray reflectrometer using a laboratory source (8048 eV) is then used to measure the coating thickness. Typically, the layer thickness can be determined with an accuracy of 0.01 nm at a single point [70–73].

3.5 Metrology and Characterization of ODL Mirrors

Reflective X-ray optics must meet exceptionally high levels of accuracy and reproducibility to achieve optimal performance, from the beam transport mirrors in the tunnels to the focusing systems in the hutches. Typical specifications for flat mirrors include a surface height error of less than 2 nm peak-to-valley (P-V) and an average radius of curvature of approximately 200 km. Further, simulations must be performed to determine the extent to which these factors may contribute to drifts in the beam position and wavefront phase distortions.

The measurements were conducted with the 12-inch large aperture Fizeau interferometer at the European XFEL in a normal incidence configuration. A brief explanation of the Fizeau interferometer is provided in Appendix A.2. The mirrors were positioned in front of the Fizeau, with their reflecting surfaces oriented facing side, with the sharp edge and clear aperture positioned at the top as shown in Fig. 3.23. The digital mask (7 mm wide) was slightly larger than the clear aperture in the software to focus on the region of interest.

We aimed to measure the mirrors both before and after coating to compare the results and determine the extent of any differences induced by the coating process. To ensure consistent setup and precise, reproducible mirror positioning in both cases, the mirrors were supported on a plate equipped with micrometer screws. These screws, installed in the plate, served as fiducial reference points: two along the length of the mirror and one on the side (see Fig. 3.23). The mirrors were aligned to contact these fiducial points as a reference. To avoid affecting the measurement by the stress caused by micrometer screw contact, the micrometer screws were moved back by 0.15 mm before the measurements were started. Each measurement result is represented as a 2D surface height map, which is an average of 15 individual measurements.

A) Before coating: Fig. 3.24 and Fig. 3.25 present the 2D surface map and the central profile of the clear aperture with both the best tilt[2] and parabola removed for

[2]The removal of tilt refers to subtracting the best-fitted tilt line from the profile, which compensates for misalignment or non-parallel positioning of the mirror with respect to the interferometer. This ensures that the analysis focuses on the actual shape of the mirror rather than misalignment artifacts.

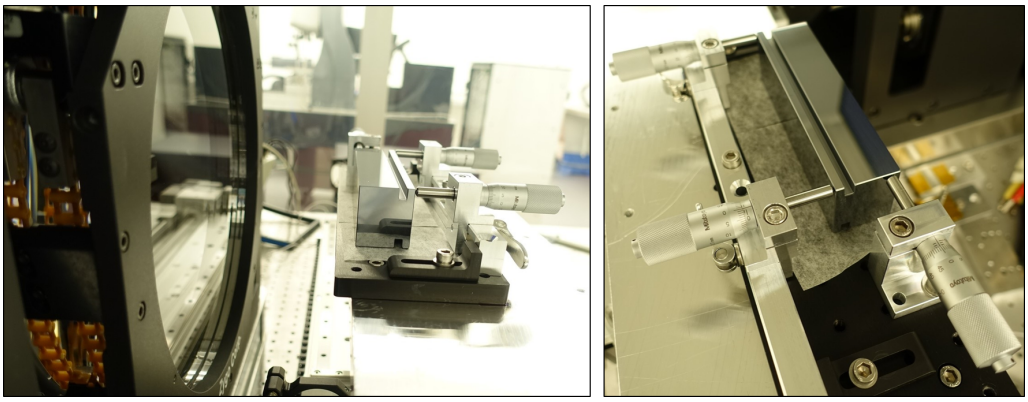

Figure 3.23: Measurement setup in front of Fizeau interferometer.

M1. A total of six mirrors were ordered, although only four are required, leaving the remaining two as spares. To select the four best mirrors, we compared their quality. Fig. 3.26 presents a comparison of the central profiles of the mirrors, showing that while M1 is not as good, the other five mirrors exhibit similar characteristics. Fig. 3.27 compares the surface height error peak-to-valley and RMS values for all six mirrors. The detailed profiles of all the mirrors can be found in Appendix A.4.

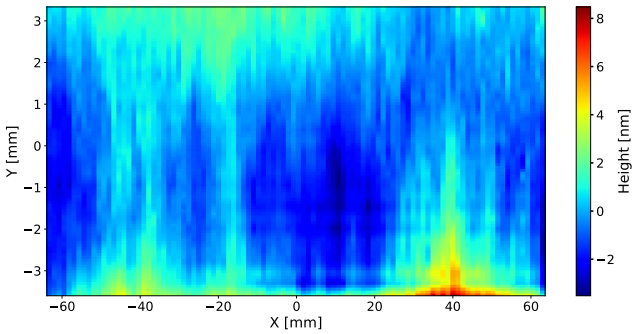

Figure 3.24: 2D map with best tilt and parabola removed for M1 before coating (P-V: 11.9 nm; RMS: 1.39 nm).The negative Y value (-3.5) represents the edge of the mirror.

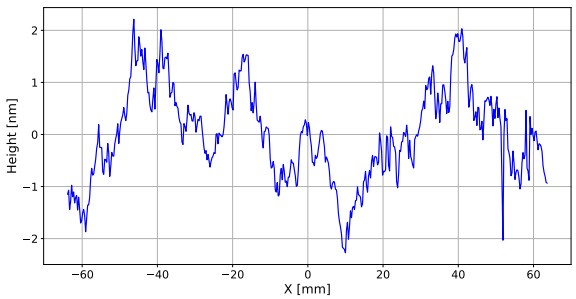

Figure 3.25: Central profile with best tilt and parabola removed for M1 before coating (P-V: 4.5 nm; RMS: 0.89 nm).

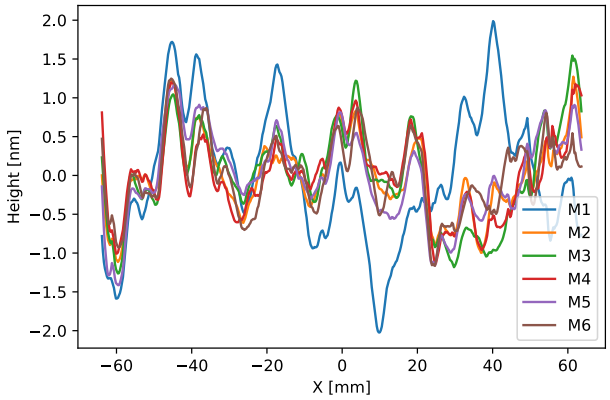

Figure 3.26: Comparing the central profile of all six mirrors.

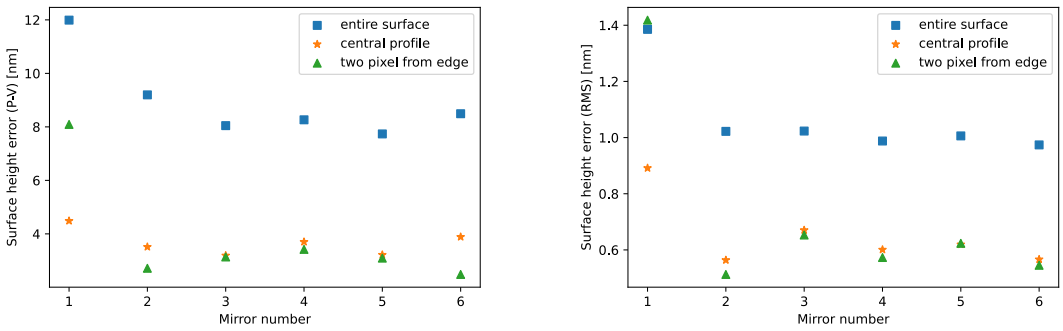

(a) Peak to valley. **(b)** RMS.

Figure 3.27: Comparison of peak-to-valley and RMS values for all six mirrors.

B) After coating: We initially ordered only two mirrors for coating to evaluate and verify the coating quality; the remaining four mirrors will be sent for coating next year. Appendix A.4 provides the 1D and 2D maps of the measurements for M1 and M3 after coating.

Fig. 3.28 and Fig. 3.29 display a comparison of measurements before and after coating for both mirrors. They illustrate the differences in the radius of curvature and surface height errors of the central profiles before and after coating. The radius of curvature of M1 after the B_4C coating is 128.31 ± 9.72 km, while for M3, it is 68.97 ± 1.37 km. The bending of the mirrors after coating can be attributed to changes in stress in the thin film applied to the surface. When a thin film, such as B_4C, is deposited on a substrate, it can induce tensile or compressive stress, depending on the film and deposition process. This stress causes the substrate to bend as it balances the forces introduced by the coating. The phenomenon can be quantified using Stoney's equation, which relates the radius curvature of the substrate to the residual stress in the thin film. Materials with lower Young's modulus are more sensitive to such stresses, leading to larger deflections. For further

details on this effect, refer to Ref. [74, 75].

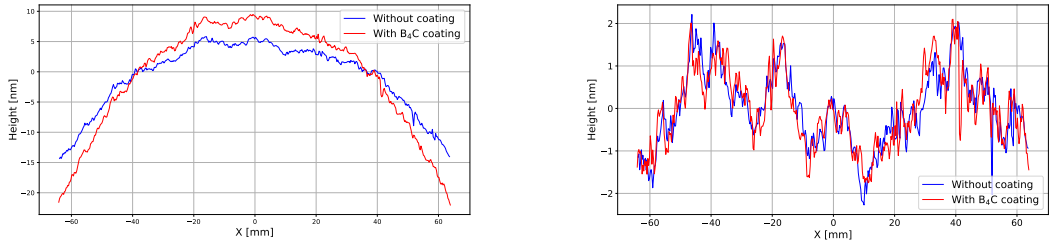

(a) Tilt removed. **(b)** Tilt and parabola removed.

Figure 3.28: Comparison of central profiles for M1 before and after coating.

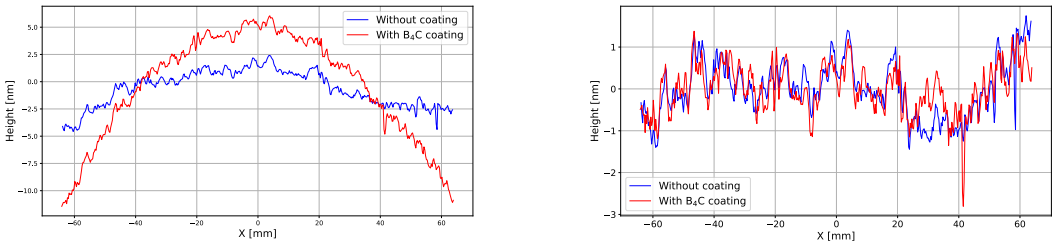

(a) Tilt removed. **(b)** Tilt and parabola removed.

Figure 3.29: Comparing of central profiles for M3 before and after coating.

3.5.1 Roughness

We measured the roughness of the mirrors using a ZYGO White Light Interferometer NexView, with measurements taken at various positions across the clear aperture surface. The White Light Interferometer (WLI) is briefly described in Appendix A.3. Fig. 3.30 illustrates the measurement setup. The measurements were performed using a 20x magnification lens with a 1x zoom.

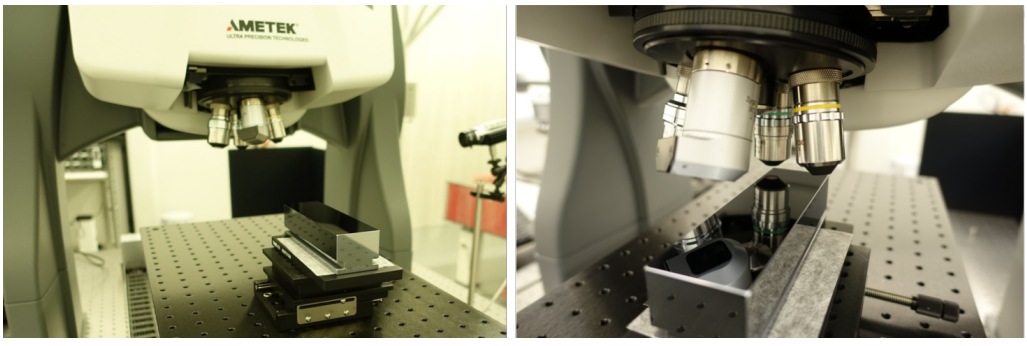

Figure 3.30: WLI measurement setup.

The resulting roughness values are averaged over 21 measurement positions. S_a represents the arithmetical mean height of the surface, which is used to assess roughness, while S_q represents the root mean square height of the surface. The roughness

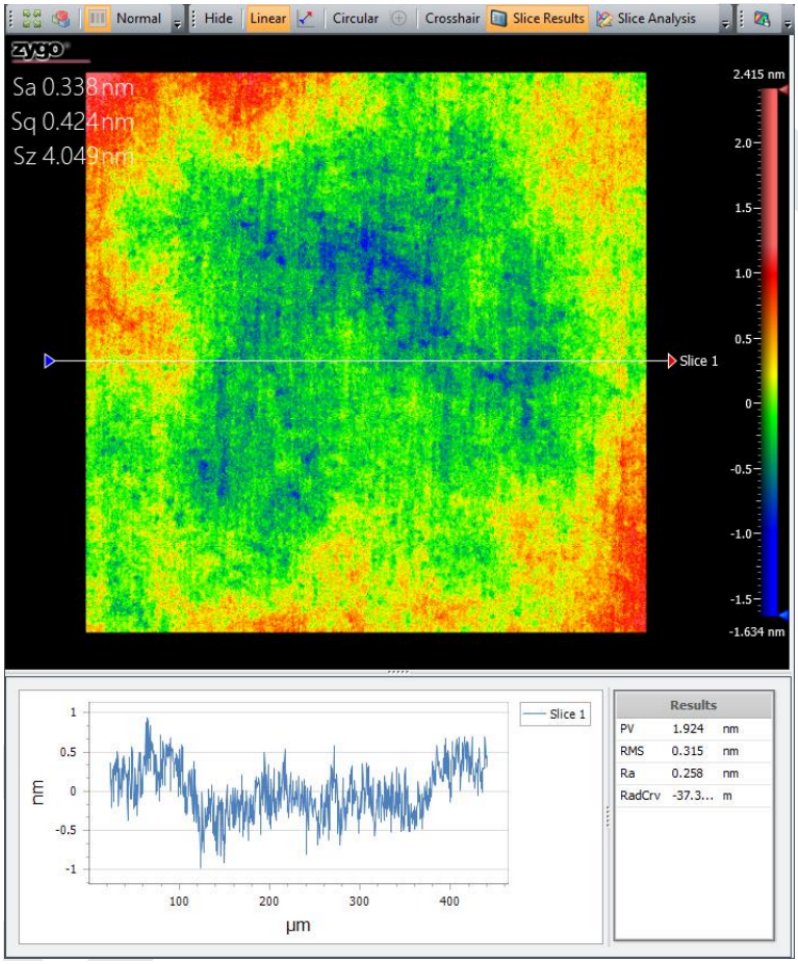

Figure 3.31: An example of a WLI measurement at one of the positions. S_a represents the arithmetical mean height of the surface, defined as the absolute value of the difference in height of each point compared to the arithmetical mean of the surface. S_q indicates the root mean square height of the surface, and S_z is the sum of the largest peak height and the largest pit depth within the defined area.

of the silicon substrate ranged between 0.19 and 0.4 nm, indicating a well-polished surface. After applying the B_4C coating, the roughness remained unchanged. The roughness measurements before and after coating were very similar, demonstrating the excellent performance of the HZG Hereon sputtering facility in coating ultra-precise mirrors. The results are summarized in Table 3.4.

	S_a(nm)	Std - S_a(nm)	S_q(nm)	Std - S_q(nm)
M1 , uncoated	0.21	0.02	0.26	0.02
M1 , coated	0.20	0.02	0.29	0.05
M3 , uncoated	0.21	0.02	0.23	0.04
M3 , coated	0.19	0.03	0.27	0.06

Table 3.4: Roughness measurements for M1 and M3 before and after coating.

3.5.2 Wavefront Propagation Simulations for Influence of Mirror Surface Imperfections

XFELs are noted for their exceptional coherence properties. In addition to opening up a new class of experiments, this characteristic also places strict demands on the optical quality of the system. In the previous section, we discussed the surface quality of the mirrors, which were measured using a Fizeau interferometer. If the mirror surface quality is inadequate, surface irregularities can cause beam distortions. To quantify the potential distortions in the wavefront caused by these optical elements, it is crucial to perform wavefront propagation simulations.

Ray tracing, based on geometric optics, is used to model beamlines transporting synchrotron and FEL radiation from the source to the experiment. While this method is sufficiently accurate for many scenarios, it has limitations. For coherent sources, where interference and diffraction effects are important, ray tracing is inadequate because it does not account for the phase of the radiation field, which is essential for modeling these effects. In contrast, wavefront propagation provides a more comprehensive approach by modeling the evolution of the complex electric field, including both amplitude and phase [2, 76].

Additionally, wavefront propagation is necessary when evaluating the effects of mirror surface imperfections on the beam profile. Since the typical quality of mirror surfaces involves imperfections on the nanometer scale, accurately modeling their impact using ray tracing (for example in COMSOL) would require a mesh size smaller than a nanometer. Such fine resolution is computationally infeasible for ray tracing.

To address this need, various optical simulation tools have been developed. Some of these tools, like SRW (Synchrotron Radiation Workshop), have a long-standing history. This tool, along with newer applications have been integrated into a user-friendly software package known as OASYS (OrAnge SYnchrotron Suite). Many of the calculations presented in this thesis were performed directly in OASYS or using Python scripts created with its help. Since its development in 2013, OASYS has become a comprehensive, open-source graphical environment for modeling X-ray sources, optical systems, and experiments. It was designed to meet the growing demand for sophisticated analysis and design of optical systems for 4th generation synchrotron radiation and FEL facilities [77, 78]. In this section, we utilize the SRW module within OASYS to simulate wavefront propagation. In the subsequent section, we will use SHADOW within OASYS to analyze mirror performance under thermal load.

The SRW code is based on the Fourier optics approach, where optical elements are represented as propagators [79–81]. This tool is designed to address the needs of

beamline scientists by facilitating the design, optimization, and improvement of X-ray optics to meet specific experimental requirements. Using SRW within OASYS, one can simulate various sources, including undulators and wigglers, as well as different optical elements like mirrors, crystals, and lenses. This enables the modeling of complete XFEL beamlines and the start-to-end simulation of experiments. Radiation from free electron lasers is partially coherent, meaning that a single wavefront is often sufficient to describe the photon beam. Wavefront propagation techniques can be employed to transport this wavefront along the beamline. A common method of propagating the electric field E is to solve the Helmholtz equation in the form of the Fresnel-Kirchhoff integral [82]. In this work, we calculate the wavefront using coherent mode, and we added the experimental metrology data to simulate the effects of mirror errors on the wavefront.

For the simulation, a Gaussian source with 1 keV photon energy was used ($\sigma = 28.8\,\mu\text{m}$), which is more usable for future ODL mirrors. Fig. 3.32 presents a schematic of the beamline, illustrating the positions of the source and the main optical elements (the sketch is not to scale). The mirrors are configured reflection for a grazing incidence angle of 9 mrad. The distance from the center of the ODL to the sample position is approximately 5.2 meters. Strong focusing is achieved using a Kirkpatrick-Baez (KB) mirror system, which is placed about 2 meters upstream of the sample position (focal plane). For each of the four mirrors of the ODL, surface distortions are included in the simulation.

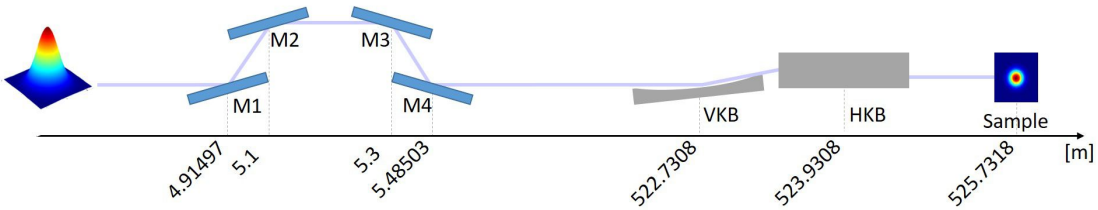

Figure 3.32: Schematic layout of the beamline used in the simulation. The diagram is not to scale.

The simulations are conducted both with and without the KB mirrors to analyze the beam profile in both focused and unfocused conditions. Fig. 3.33 displays the beam profile at the sample position, considering the metrology data and including the effects of the parabolic surface distortions. The left panel shows the results without the KB mirrors (with beam sizes of $\sigma_x = 1814\,\mu\text{m}$ and $\sigma_y = 2145\,\mu\text{m}$), while the right panel shows the results with the KB mirrors (with beam sizes of $\sigma_x = 1.36\,\mu\text{m}$ and $\sigma_y = 2.73\,\mu\text{m}$).

Fig. 3.34 presents intensity distribution images, comparing the beam profiles using a perfect mirror and a real mirror with surface imperfections. Results without KB mirrors are shown on the left side, and results with KB mirrors are shown on

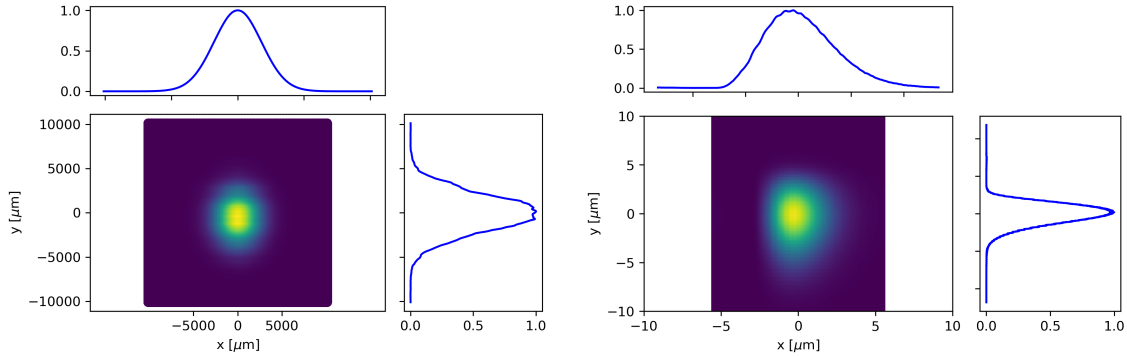

(a) Without KB ($\sigma_x = 1814\,\mu\text{m}$, $\sigma_y = 2145\,\mu\text{m}$). **(b)** With KB ($\sigma_x = 1.36\,\mu\text{m}$, $\sigma_y = 2.73\,\mu\text{m}$).

Figure 3.33: OASYS - SRW simulation. Beam profile at the sample position illustrating the effects of mirror surface imperfections (with metrology data considered). (a) Without the KB mirrors, the beam exhibits slight distortion along the y-axis. (b) With the KB mirrors, these distortions become negligible.

the right side. As the results indicate, the beam is slightly altered due to the surface imperfections. However, when the KB mirrors are used, the impact of the surface distortions becomes negligible.

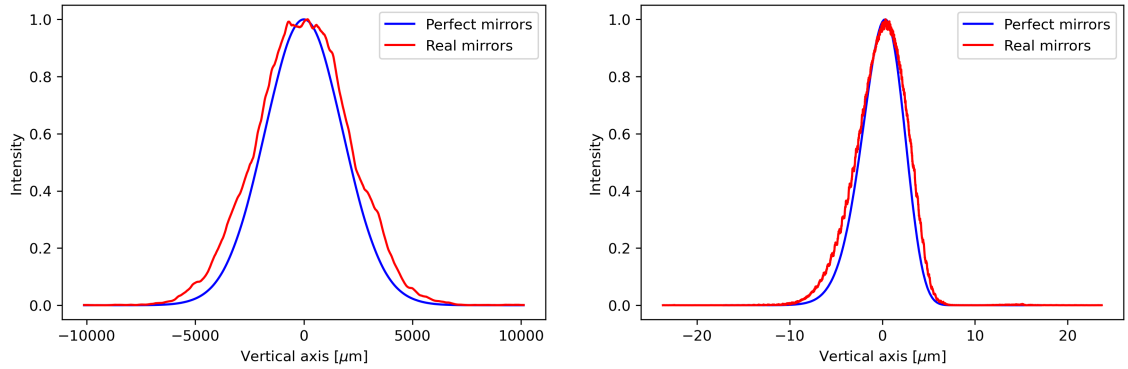

(a) Unfocused beam profile without KB. **(b)** Focused beam profile with KB.

Figure 3.34: OASYS - SRW simulation. Comparison of intensity distribution at the sample position using perfect and real mirrors with surface imperfections.

3.6 Effect of Heat Load and Mechanical Structure on the Beam Profile

In this section, we discuss the thermal heat load on the mirrors and the resulting deformations of ODL on the beam profile. Specifically, we investigate: How much are the mirrors deformed due to this heat load and their mechanical structure? Should the mirrors be cooled, and how do deformations affect the beam profile?

Deformations of optical elements, caused by both heat load and mechanical stress, need to be carefully examined. To achieve this, optics simulations must

incorporate the results from engineering models of thermal deformations, which are typically carried out using finite element analysis (FEA). In this section, the findings from the mechanical engineering team's FEA simulations are summarized and incorporated into our ray-tracing analysis to assess the impact of mirror deformations on the beam profile.

3.6.1 Cooling of M1

The generated radiation can be categorized into two main types:

1. **SASE radiation (direct radiation)** – Highly coherent radiation with a well-defined energy and direction.
2. **spontaneous radiation (background radiation)** – A broader energy spectrum surrounding the powerful X-ray beam.

The mechanical group conducted simulations and concluded that cooling the first mirror (M1) with water would be sufficient to reduce the thermal load (the results of these simulations will be discussed in the next section). The M1 is exposed to both SASE and spontaneous background radiation. The background radiation is absorbed entirely by M1, preventing any significant impact on the other mirrors.

To further diminish the thermal load, a B_4C mask will be installed upstream of M1 to block part of the spontaneous radiation and protect the mirror and associated mechanics. This mask consists of two movable parts, allowing the gap to be adjusted as needed.

The average heat load on the mirror from FEL radiation is a few watts, which can be minimized through water cooling. To achieve this, a nickel-coated copper bar is positioned approximately 100 µm from the side of the mirror. The copper bar is connected to a water-cooled copper pipe via thermal braids, ensuring efficient heat removal. The braids, being soft elements with very low natural frequencies, act as low-pass filters, reducing most of the high-frequency vibrations. The cooling system is designed to avoid direct contact with the mirror, preventing vibrations that could degrade its optical performance. A thin layer of liquid indium-gallium (InGa) alloy is placed between the mirror and the copper bar to provide efficient thermal conduction while minimizing mechanical stress. Additionally, this alloy layer acts as a damper for vibrations. Fig. 3.35 illustrates the cooling method employed for M1.

3.6.2 FEA Analysis

Thermal loads on the mirror typically cause surface deformations, often referred to as "bumps." Finite Element Analysis (FEA) simulations using ANSYS were con-

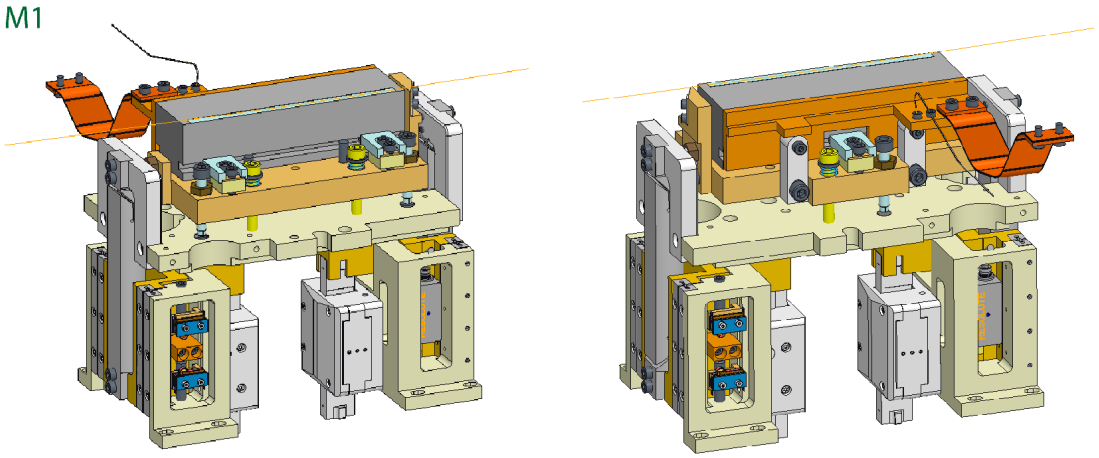

Figure 3.35: Cooling system for the first mirror (M1), depicted in orange. Drawn by FMB-Berlin [58].

ducted to model these deformations. The results were then used to evaluate their impact on the beam profile through ray-tracing simulations performed in SHADOW.

The ANSYS simulations were based on the following parameters (approximate values provided by the ME group for their simulations):

- Pulse energy: 5 mJ
- Number of pulses per train: 200
- Reflectivity: 98%
- Repetition rate: 10 Hz
- Heat load from SASE radiation: 0.2 W
- Heat load from spontaneous radiation: 4 W
- FWHM beam size: 0.459 mm
- Incidence angle: 9 mrad

The heat load was calculated using the formula:

$$\text{Heat Load} = \text{Pulse Energy} \times \text{Number of Pulses} \times (1 - \text{Reflectivity}) \times \text{Repetition Rate}$$

The boundary conditions used in the simulation are as follows:

- Convection coefficient on the cooling area: $h_1 = 3000\,\mathrm{W/m^2\,^\circ C}$
- Convection coefficient on the contact surface: $h_2 = 50000\,\mathrm{W/m^2\,^\circ C}$

- Emissivity on the top surface: 0.8
- Initial temperature: 22°C

Fig. 3.36a shows the boundary conditions, 3.36b illustrates the temperature distribution with the FEL beam for M1, and 3.36c displays the temperature distribution for M2, M3, and M4.

The simulation results indicate that M1 experiences a total deformation of approximately 9.5 nm: 1.3 nm from the SASE radiation, 7.5 nm from the spontaneous background radiation, and 0.7 nm from mechanical structure. This deformation corresponds to a radius of curvature of about 200 km.

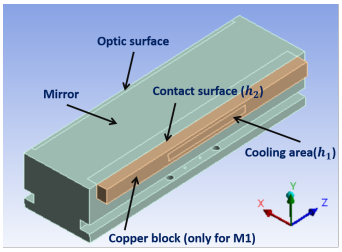

(a) Boundary conditions used in the FEA simulation.

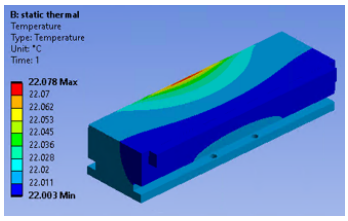

(b) Temperature distribution across M1 under the influence of FEL radiation.

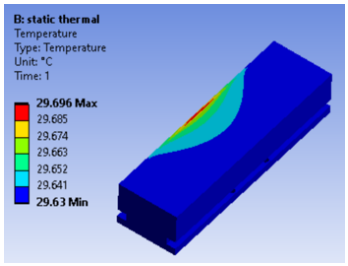

(c) Temperature distribution for M2, M3, and M4.

Figure 3.36: Temperature distribution due to heat load, simulated using ANSYS by the ME group.

Fig. 3.37a shows the total vertical deformation of M1 due to heat load and mechanical structure, while Fig. 3.37b presents the total deformation for M2, M3, and M4, which is approximately 1–2 nm, indicating lower deformations. M2 and M3 experience different deformation patterns because they are positioned upside down, causing gravity and mechanical structure to impact them differently than M1 and M4.

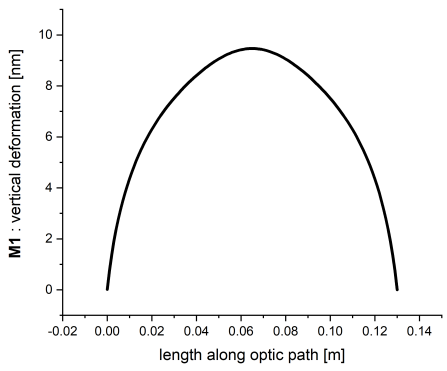

(a) For mirror M1.

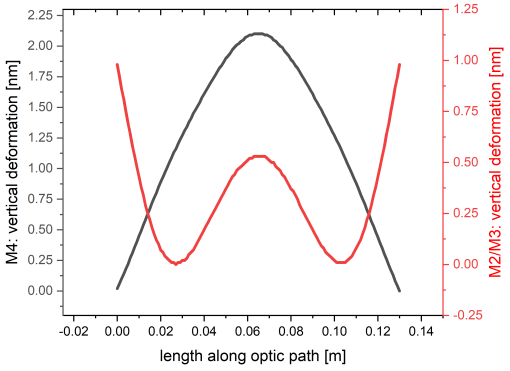

(b) For mirrors M2, M3, and M4.

Figure 3.37: Total vertical deformation due to heat load and mechanical structure.

3.6.3 SHADOW, Ray-Tracing Simulation

A thermal bump of several nanometers builds up during pulse trains, causing slight deformation of the beam and potentially leading to a small defocusing effect in subsequent optics. The convex deformation of M1 increases the beam divergence, effectively creating a virtual source that appears closer to the ODL than the actual source[83].

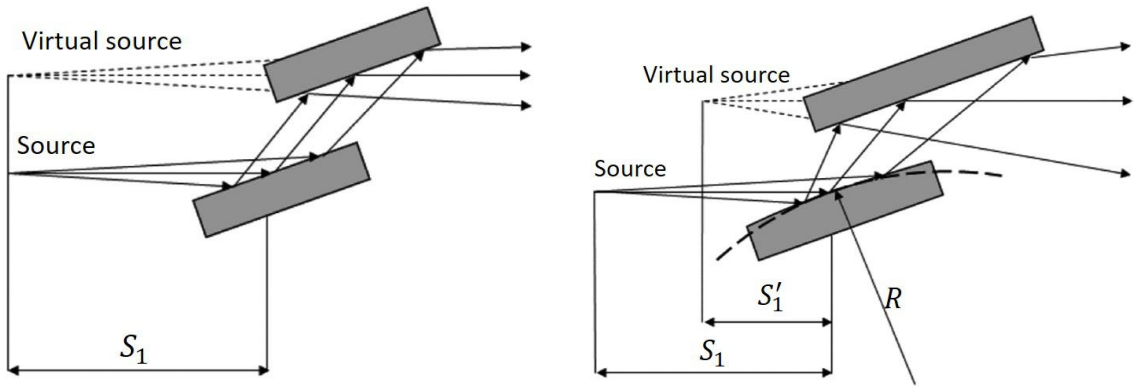

(a) Perfect mirror, the virtual source is aligned with the true source.

(b) Deformed mirror, the virtual source shifts closer to the ODL than the real source.

Figure 3.38: A side-view schematic representation of the first mirror in the ODL, showing both perfect and thermally-deformed states[83].

To estimate the location of the virtual source, the deformed first mirror can be treated as a tangentially defocusing mirror. The relationship between the source and virtual source is given by:

$$\frac{1}{S_1} - \frac{1}{S_1'} = -\frac{2}{R\sin\theta} \tag{3.21}$$

where S_1 and S_1' are the distances from the source to the mirror and from the mirror to the virtual source, respectively. R is the radius of curvature for the thermal bump, and θ is the grazing incidence angle of the central ray. The distance between the virtual source and the first mirror is then calculated as:

$$S_1' = \frac{S_1 R\sin\theta}{2S_1 + R\sin\theta} \tag{3.22}$$

Consider the KB system as a focusing optical element. The distance from the virtual source to the KB is $p = S_1' + d$, where d is the distance between the mirror and the KB system. The focal distance, q, is then determined using the following equation:

$$\frac{1}{p} + \frac{1}{q} = \frac{1}{f} \tag{3.23}$$

where f is the focal length of the KB mirror. We aim to investigate how much the focal distance q will change. Since this thermal deformation is primarily in the vertical direction, it mainly affects the vertical KB (VKB). Our KB system is bendable, then they can be set to focus the first source (U1). In the absence of thermal deformation, $R = \infty$ and the focal length of the VKB is $f = 2.98\,\text{m}$. For a thermal deformation radius of $R = 200\,\text{km}$, the focal distance changes by only 2.9 mm, indicating that the beam is not affected by deformation.

These analytical formulations provide an approximation. In the following, we will use SHADOW (ray-tracing simulations) within OASYS to account for the deformation of all mirrors and determine the beam profile.

The ray-tracing method is a powerful tool for predicting the performance of optical systems, particularly in synchrotron and FEL radiation applications. One of the most widely used codes for this purpose is SHADOW, implemented within the OASYS framework. In this ray-tracing approach, each ray is represented as a mathematical entity defined by four vectors and two phases. The source is modeled using the Monte-Carlo method, which samples rays according to the spatial, angular, and energy distributions characteristic of synchrotron or FEL sources. Each ray represents a small photon beam that is traced through a series of optical elements (e.g., mirrors, gratings, crystals), making the method well-suited for simulating incoherent beams. The beam intensity is computed as the sum of the intensities of all the rays, with each contributing independently to the total intensity [77].

The simulation using OASYS was performed, keeping the same beamline configuration as described in Section 3.5.2. The input beam was Gaussian with a sigma angular distribution of 3.7 µrad. Since the deformation on the mirror is too small, we use the deformed mirrors 10 times more to evaluate the impact. Fig. 3.39 shows the intensity distribution at the sample position with and without the KB system.

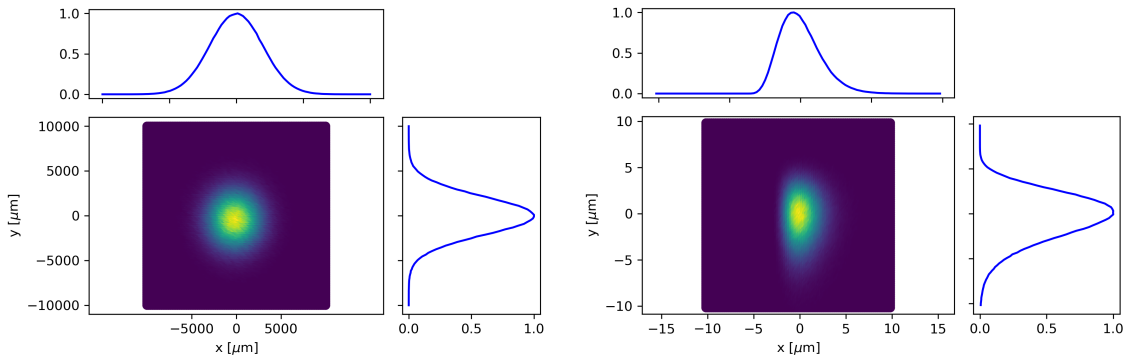

(a) Without KB ($\sigma_x = 1956.6\,\mu\text{m}$, $\sigma_y = 2137.5\,\mu\text{m}$).

(b) With KB ($\sigma_x = 1.43\,\mu\text{m}$ and $\sigma_y = 2.55\,\mu\text{m}$).

Figure 3.39: OASYS - SHADOW simulation, beam profile at the sample position using deformed mirrors.

Fig. 3.40 illustrates the effect of mirror deformation on the beam profile by com-

paring the beam profiles using a perfect mirror and a mirror with 10 times more deformed surface. The same result was obtained using wavefront propagation simulation (SRW). In this case, using SHADOW is more convenient as it consumes less time than SRW. As expected, the average thermal and heat loads, as well as the mechanical structure, do not cause any distortions in the beam profile, demonstrating that water cooling can be effectively applied.

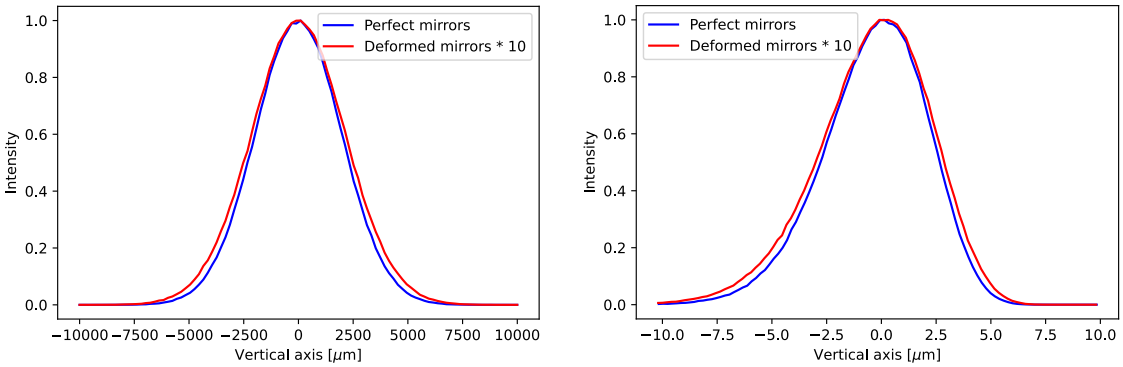

(a) Without KB.

(b) With KB.

Figure 3.40: OASYS-SHADOW simulation. Comparison of the intensity distribution at the sample position between a perfect mirror and a deformed mirror. To evaluate the impact, the deformation of the mirror was artificially increased by a factor of 10, as the actual deformation is too small. The results show no significant effect on the beam profile. The KB mirrors are assumed to have perfect surfaces.

3.7 Damage

One of the central concerns regarding the ODL mirrors is whether they can withstand the high X-ray peak power during FEL operation, both single and multi-pulse. Since the ODL mirrors are located close to S1 (approximately 5 m), the beam footprint on the mirrors is relatively small.

The footprint of a beam on a mirror refers to the area the FEL beam covers on the mirror surface. For grazing incident condition, the footprint of the beam has a length of the beam width divided by $sin(\theta)$ (see Fig. 3.41).

On the other hand, the SASE3 undulator operates at a repetition rate of 10 Hz and produces X-ray pulse trains with tunable photon energies ranging from 250 to 3000 eV, with single-pulse energies reaching several millijoules. Consequently, a key question emerges: can specialized X-ray optics endure the high peak power of an X-ray photon pulse? This analysis is divided into two main sections: single-shot and multi-pulse damage.

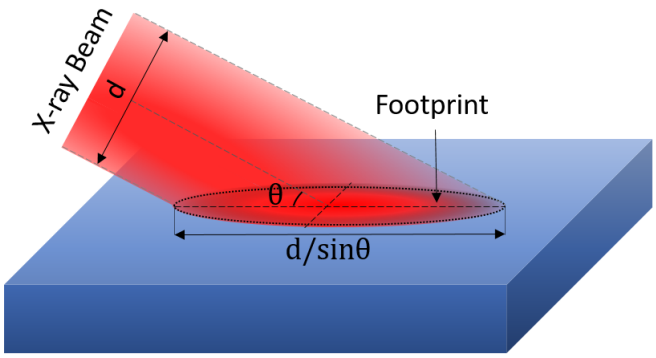

Figure 3.41: Illustration of the footprint of an X-ray beam on a mirror at grazing incident condition.

3.7.1 Single-Shot Damage

According to the previous sections, the mirror consists of silicon coated with a 50 nm layer of B_4C, and it operates under total reflection conditions at a grazing incidence angle of 9 mrad. The beam generates an evanescent wave just beneath the surface, which is absorbed by the coating layer. For calculations of refractive index, reflectivity, and penetration depth, the density is assumed to be 2.52 g/cm^3 based on data obtained from the CXRO website (Fig. 3.42) [68].

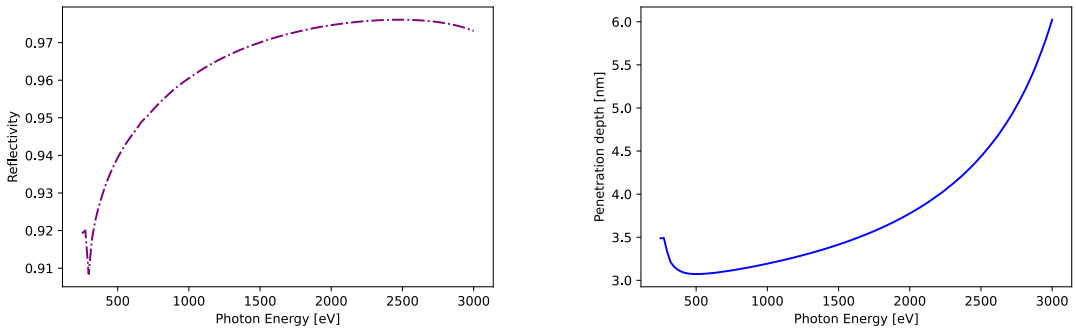

(a) Reflectivity.

(b) Penetration depth.

Figure 3.42: For B_4C at 9mrad, data sourced from CXRO [68].

Damage occurs when the local energy density in the material exceeds its melting threshold. Above this critical threshold, ablation occurs, and at sufficiently higher energy densities, phenomena like plasma formation and non-thermal melting may arise. To determine the pulse energy at which photon energy can damage the mirror, we use the following absorbed dose equation Eq.3.24 [26, 28, 84]. If the absorbed dose is below the melting threshold, the material remains intact; otherwise, damage occurs. The melting dose for B_4C is 0.62 eV/atom, according to Ref. [85].

$$D_{\text{absorbed}} = \frac{m_{\text{atom}}}{\rho}(1-R)\frac{E_{\text{pulse}}\sin\theta}{2\pi\sigma^2 Z_{\text{pen}}} \tag{3.24}$$

In this equation, $m_{\text{atom}} = \frac{A}{N_A}$, A is the atomic weight for B_4C (55.255/5 g/mol), N_A is Avogadro number, ρ is the density (2.52 g/cm^3), R is the reflectivity, θ is the grazing incidence angle, E_{pulse} is the pulse energy, σ is the beam size, and Z_{pen} is the penetration depth (discussed in Section 3.4.2). This calculation does not take into account electron collision length, which will be discussed in the next chapter.

Fig. 3.44 presents the relative absorbed dose (normalized to the dose at 90° incidence) as a function of grazing angle, calculated using the Eq. 3.24:

- **Below the critical angle ($\theta < \theta_c$):** At very small grazing angles, the penetration depth Z_{pen} remains nearly constant, and the footprint is large due to the shallow angle, and reflectivity is high (see Fig. 3.20 and Fig. 3.43). This combination results in a low absorbed dose. As the angle approaches the critical angle, the reflectivity decreases, causing the absorbed dose to increase. Around θ_c, $1-R$ rises sharply, but the increase in penetration depth Z_{pen} is less rapid, so the peak dose occurs slightly below θ_c . This shift occurs because the rate of change in Z_{pen} and $1-R$ do not align perfectly at θ_c.

- **Above the critical angle ($\theta > \theta_c$):** The reflectivity drops significantly, while the penetration depth Z_{pen} increases. At these higher angles, the absorbed dose stabilizes, as the smaller footprint compensates for the increased penetration depth, resulting in a relatively constant dose.

The source properties, including SASE divergence and the radiation spot size as a function of photon energy, are shown in Fig. 3.45a and Fig. 3.45b and listed in Table. 3.5. Using this information, and with a grazing angle of 9 mrad, the dose per atom can be estimated using Eq. 3.24 for different pulse energies. Fig. 3.45c shows the absorbed dose versus photon energy for three different pulse energies (500, 1000, and 2000 µJ), with the horizontal dashed line indicating the melting dose of B_4C, 0.62 eV/atom.

Photon energy [eV]	Divergence [µrad]	Radiation spot [µm]
250	14.9	77.4
500	10.6	55.3
1000	5.5	28.8
2000	3.0	15.5
3000	2.0	10.6

Table 3.5: Source properties.

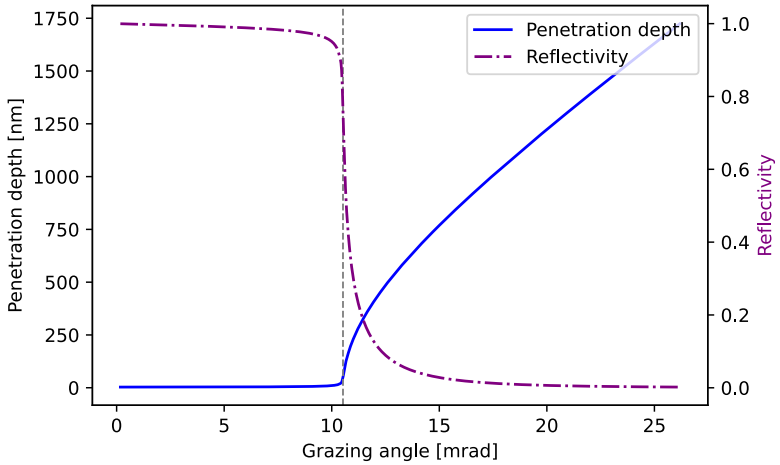

Figure 3.43: Penetration depth and reflectivity as functions of grazing angle for 3 keV photon energy. The vertical dashed gray line indicates the critical angle ($\theta_c = 10.5$ mrad) for B_4C at 3 keV. Below the critical angle ($\theta < \theta_c$), the penetration depth remains nearly constant, and reflectivity is high. Above the critical angle ($\theta > \theta_c$), the reflectivity decreases sharply, while the penetration depth increases.

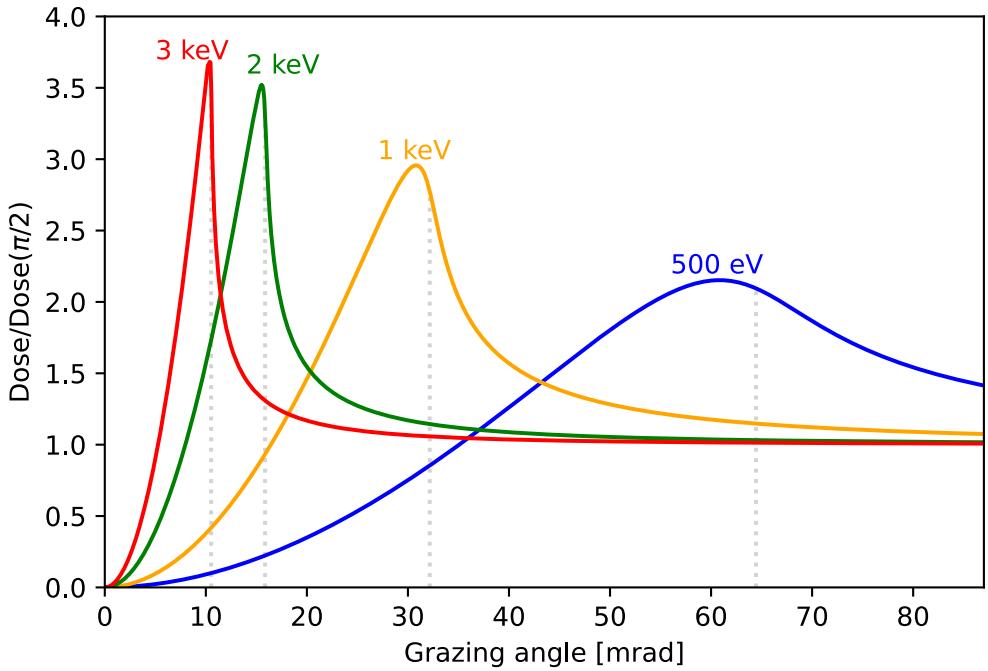

Figure 3.44: Relative absorbed dose for B_4C at various photon energies. The scale is normalized to the dose at normal incidence. The vertical dotted gray lines show the critical grazing angle corresponding to each photon energy.

At higher photon and pulse energies, the absorbed dose exceeds the melting threshold, resulting in damage to the mirror coating. To prevent this, we propose opening some undulator cells upstream of the ODL. This increases the distance

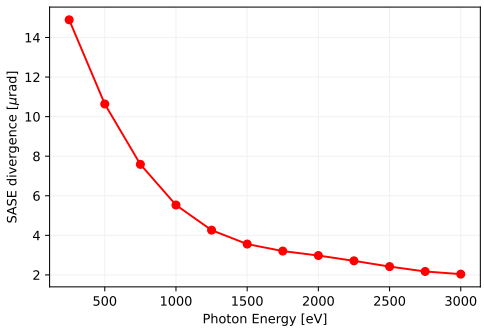

(a) SASE divergence.

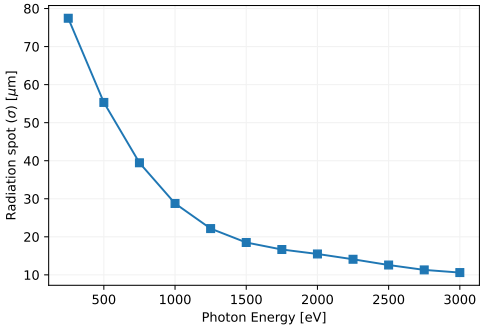

(b) Radiation spot size for the source-to-ODL distance of 5.2 m.

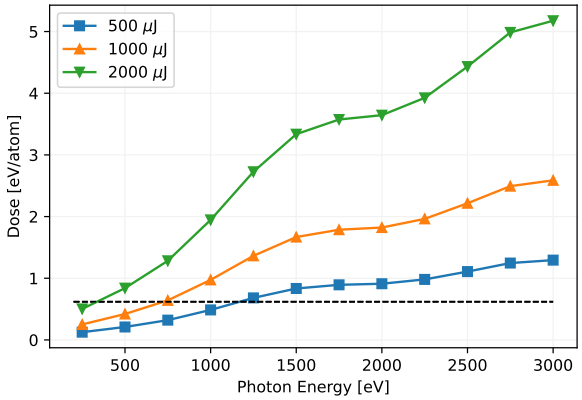

(c) Absorbed dose. The dashed line represents the melting threshold dose (0.62 eV/atom).

Figure 3.45: Source properties and calculated absorbed dose.

between the source and the mirror, leading to a larger footprint on the mirror, thereby reducing the energy absorbed per atom and preventing damage.

The distance between the last undulator cell and the ODL is 5.2 m, and each undulator cell has a length of 6.2 meters. Therefore, if one undulator cell is opened, the distance between the ODL and the radiation source will increase by $5.2 + 6.2 = 11.4$ m. As a result, the radiation spot size will increase.

$$\text{Source distance} = 5.2 + 6.2 \times \text{n}_{\text{unds\_open}}$$

$$\text{Radiation spot} = \text{Source divergence} \times \text{Source distance}$$

By opening undulators, the flux on the mirrors is reduced, allowing the optics to withstand higher pulse energies. Fig. 3.46 and Fig. 3.47 illustrate the radiation spot size and absorbed dose for different numbers of undulators opened and varying pulse energies. The plots confirm that opening undulators upstream of the ODL helps the optics tolerate higher flux levels without damage [86].

One important question arises with the opening of undulators: as the radiation spot increases and consequently extends the beam footprint on the mirror, is the

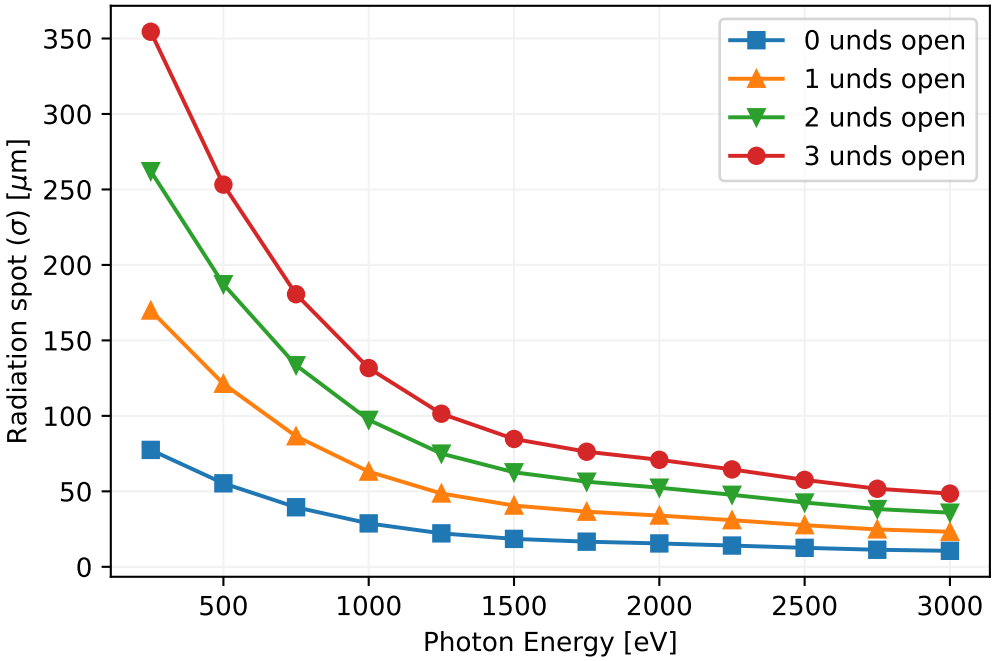

Figure 3.46: Radiation spot size for different numbers of undulators opened.

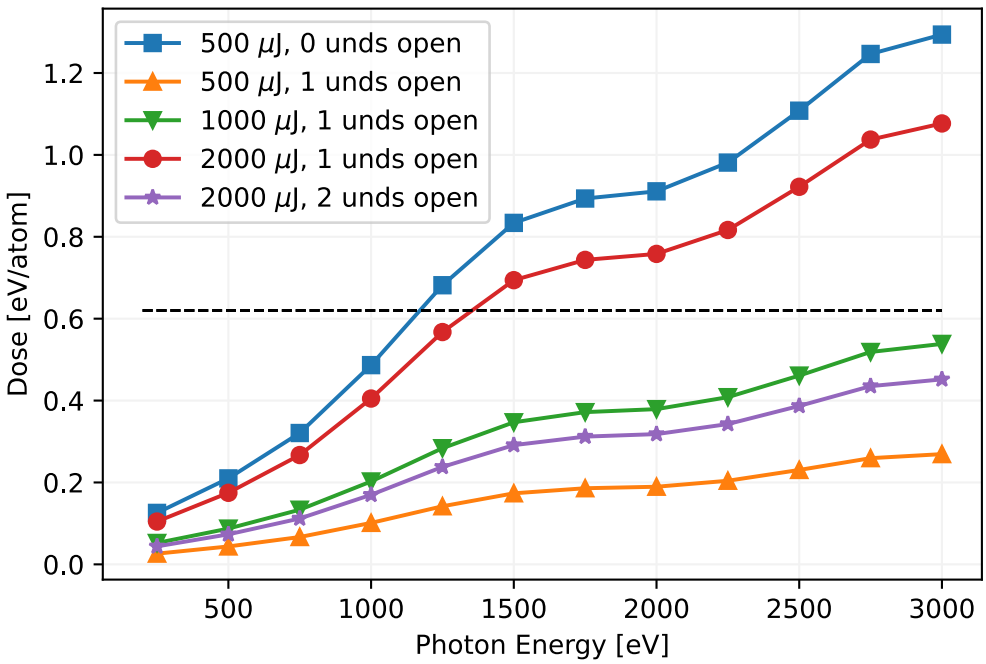

Figure 3.47: Absorbed dose for different pulse energies and varying numbers of undulators opened. Opening undulators upstream reduces the absorbed dose, allowing the optics to tolerate higher energies.

mirror length still sufficient? Given the limited space between the MC, the mirror length cannot be excessively extended. Therefore, we need to investigate this scenario. For the worst case, where two undulators are open upstream of the ODL and the photon energy is 250 eV-a condition with higher beam divergence-the footprint[3] can be calculated as follows:

$$\text{Source distance} = 5.2 + 6.2 \times 2 = 17.6\,\text{m}$$

$$\text{Radiation spot} = 14.9 \times 17.6 = 262\,\mu\text{m}$$

$$\text{Footprint} = \frac{4\sigma}{\sin\theta} = \frac{1049}{0.009} = 116\,\text{mm}$$

These calculations show that a mirror length of 140 mm is sufficient. Additionally, as shown in Fig 3.47, it is not necessary to open undulators for lower photon energies, such as 250 eV.

3.7.2 Multi-Pulse Damage

As discussed in Section 2.3, a pulse train at the European XFEL can consist of up to 2700 X-ray pulses, with a 222 ns spacing between pulses at a repetition rate of 4.5 MHz. In experiments using multi-pulse, if there is no efficient heat dissipation during the time between pulses, the temperature rise from each pulse may accumulate, potentially leading to material damage over the pulse train. Utilizing grazing incidence geometry for the optical elements reduces the X-ray penetration depth perpendicular to the surface, which creates a steeper temperature gradient and enhances heat flow. However, it is essential to investigate the maximum number of pulses and energy levels that the material can withstand before damage occurs [87, 88].

The energy conservation law in this case is represented by the heat balance equation [89, 90]:

$$c_p\rho\frac{\partial T}{\partial t} = -\nabla \cdot q + Q \tag{3.25}$$

where q is the heat flux (W/m^2), $c_p\rho$ is the heat capacity per unit volume (J/m^{3}K), Q is the external heat source (W/m^3), and T is the temperature (K). Based on Fourier law, heat flow is determined by the direction and magnitude of the thermal gradient:

$$q = -k\nabla T \tag{3.26}$$

where k (W/mK) is the thermal conductivity. Combining Equations (3.25) and (3.26) yields the classical heat diffusion equation (HDE):

[3] In this analysis, the beam size is approximated as 4σ to encompass the full beam.

$$c_p \rho \frac{\partial T(\mathbf{r},t)}{\partial t} - k\nabla^2 T(\mathbf{r},t) = Q(\mathbf{r},t) \tag{3.27}$$

which must be solved with the initial condition of $T(\mathbf{r},0) = T_0$.

The external heat source, Q, represents the absorption of an FEL pulse with a Gaussian spatial and temporal distribution [86, 90–92]:

$$Q_{absorbed}(x,y,z,t) = (1-R)\frac{E_{pulse} sin\theta}{(2\pi)\sigma_x\sigma_y Z_{pen}\sqrt{2\pi}\sigma_t} \cdot e^{-\frac{(x-x_0)^2 sin^2\theta}{2\sigma_x^2}} \cdot e^{-\frac{(y-y_0)^2}{2\sigma_y^2}} \cdot e^{-\frac{z}{Z_{pen}}} \cdot e^{-\frac{(t-\mu)^2}{2\sigma_t^2}} \tag{3.28}$$

where E_{pulse} is the pulse energy, σ_t and $\sigma_x\sigma_y$ are the pulse duration and beam size, respectively. R is the reflection coefficient and Z_{pen} is the penetration depth. The depth dependence follows Lambert-Beer law, with the exponential absorption term $e^{-z/Z_{\text{pen}}}$, where $Z_{\text{pen}} = 3.37\,\text{nm}$ is the radiation penetration depth at 1 keV and a 9 mrad grazing angle, based on Ref. [68]. The integration of this equation over space and time yields the total absorbed pulse energy, $(1-R)E_{\text{pulse}}$. The excitation geometry is depicted in Fig 3.48.

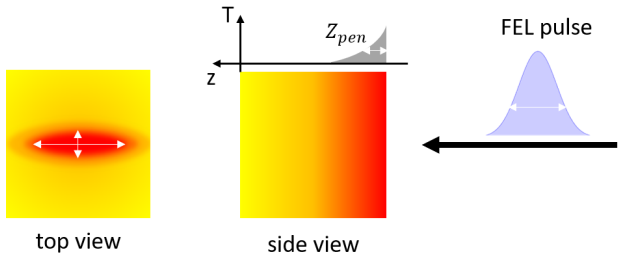

Figure 3.48: Schematic of excitation geometry: A Gaussian pulse with a certain width is absorbed at the sample surface.

To solve Eq. 3.27 and 3.28, Finite Element Analysis (FEA) using Comsol Multiphysics was performed to predict the temperature increase under the thermal load of the European XFEL beam [88, 93]. We modeled a 2D 50 nm B_4C layer on 0.2 mm silicon, considering a 1 keV X-ray pulse with a Gaussian distribution at a 4.5 MHz repetition rate, matching maximal European XFEL beam conditions. The initial temperature was set to 300 K. It was assumed that there was no heat transfer at the sample boundaries. Although the pulse duration is approximately 25 fs, the time scale for the source term was set to 1 ps to account for the characteristic electron-phonon coupling time, which represents the transfer of absorbed energy from electrons to the lattice [94]. All material parameters are temperature-dependent and are listed in Appendix A.1.

Fig. 3.49 shows the temperature profile at the center of the mirror, which represents the hottest point on the optic. The pulse energy used in this simulation was 500 µJ (see Table 3.6 for the parameters). This pulse energy was chosen as an example to demonstrate the methodology, and the same simulation procedure was followed for other pulse energies. The temperature curve features an initial rapid decrease, which results from heat transfer from the hot B_4C layer into the bulk of the silicon substrate. This is followed by a slower decline, indicating the transfer of accumulated heat from within the substrate to the edges. The maximum temperature after the first FEL pulse reaches 1464 K, which is well below the melting point of B_4C (2623 K), ensuring that the material remains undamaged.

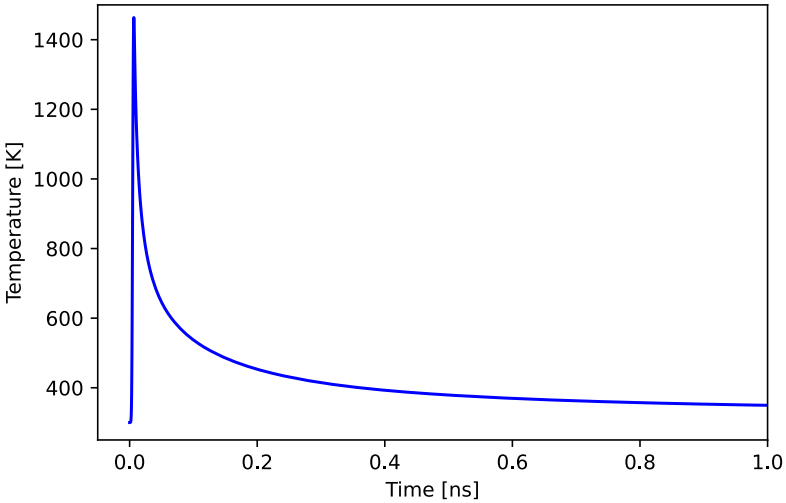

Figure 3.49: Temperature profile at the center of the mirror for 500 µJ.

Pulse energy (E_{pulse})	500 µJ
Photon Energy	1000 eV
Grazing angle (θ)	9 mrad
Penetration depth (Z_{pen})	3.37 nm
Reflectivity (R)	0.96
Time duration (σ_t)	1 ps
Beam size (σ_x, σ_y)	28.8 µm

Table 3.6: Parameters used in COMSOL simulations corresponding to 1 keV related to Fig. 3.49.

Fig. 3.50 illustrates the temperature profile over time at the center of the mirror during a train of 300 pulses. Fig. 3.50a displays the temperature for the first ten pulses, while Fig. 3.50b shows the temperature for the last ten pulses. After 300 pulses, the temperature reaches approximately 1640 K. It takes 29 hours to run this simulation. From the simulation, it is evident that the B_4C layer remains below its

melting point throughout the entire pulse train at this pulse energy.

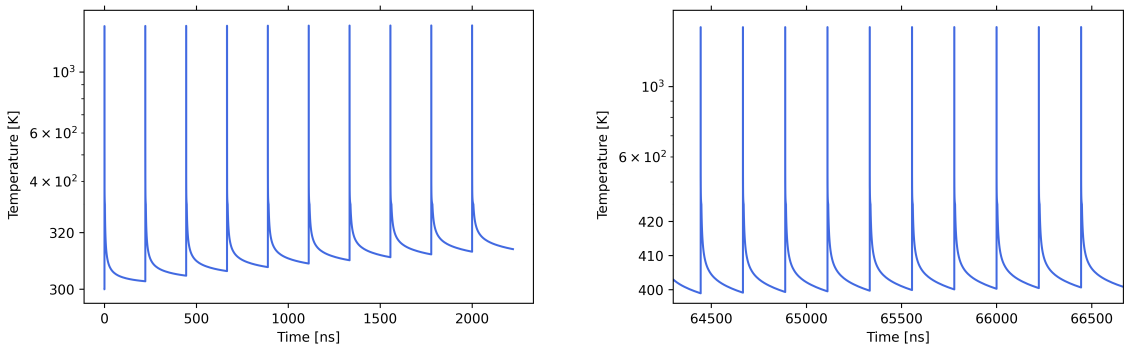

(a) First 10 pulses.

(b) Last 10 pulses.

Figure 3.50: Temperature accumulated over 300 pulses, for 500 µJ pulse energy.

The simulation continues with the temperature-depth distribution up to 50 ps after the absorption of single FEL pulse. To illustrate the behavior at higher energies, an example result for a pulse energy of 1000 µJ is shown in Fig. 3.51 (a time-depth plot where color indicates temperature). As illustrated, the temperature peaks at the surface immediately following the FEL pulse. Over time, the heat diffuses deeper into the material, but the majority of it is absorbed by the B_4C layer, as indicated by the temperature gradient.

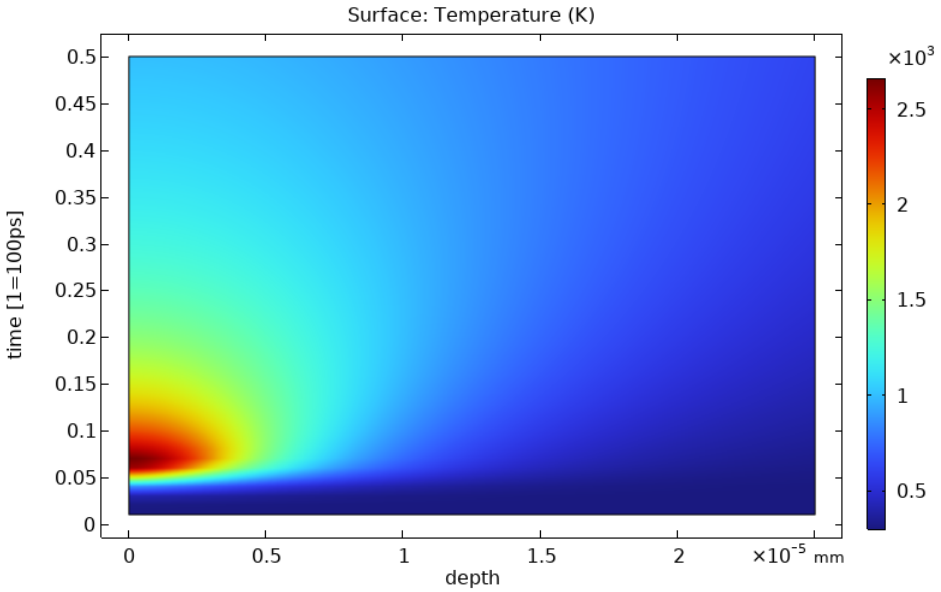

Figure 3.51: Temperature depth distribution up to 50 ps after absorption of 1000 µJ, showing the thermal response over time and depth. As illustrated, the temperature peaks at the surface immediately following the FEL pulse. Over time, the heat diffuses deeper into the material, but the majority of it is absorbed by the B_4C layer.

The comprehensive results for a range of pulse energies (100-900 µJ) are summarized in Fig. 3.52, which presents the maximum temperature on the sample surface

after each successive pulse. The dashed black line indicates the melting temperature of B_4C, which is 2623 K. When pulse energies approach this melting threshold, there is a risk of damage or degradation of the B_4C layer, which can impact the quality of the X-ray beam. For experiments, it is therefore essential to maintain pulse energies below this limit to ensure the longevity and stability of the mirrors. If higher pulse energies are required, it may be necessary to adjust the repetition rate or number of pulses to prevent overheating.

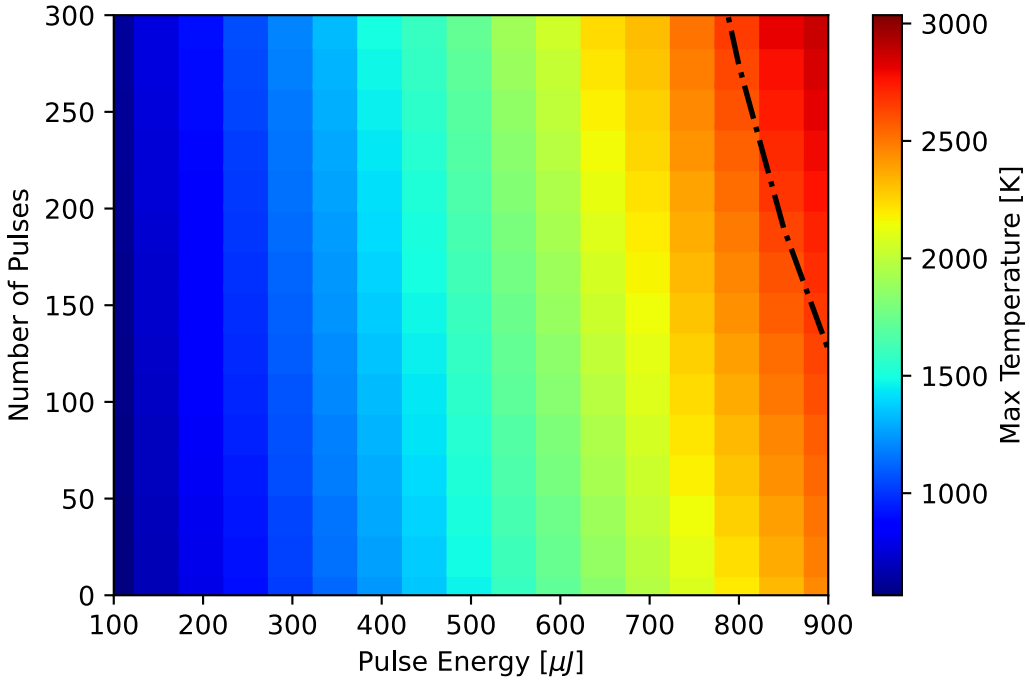

Figure 3.52: Cumulative temperature after pulses for different energy from 100 to 900 µJ. The dashed black line represents the B_4C melting temperature (2623 K).

Calculations show that when the next pulse arrives, a significant amount of heat remains on the sample surface from the previous pulse, indicating that heat accumulation occurs in multi-pulse conditions.

In this study, we have neglected the potential effects of non-thermal melting. In the presented case, heat accumulation occurs over several nanoseconds, and as such, the electrons and lattice remain in thermal equilibrium for most of the time.

3.8 Conclusion

In this chapter, we explored the benefits and necessity of the ODL in conjunction with the MC for achieving tunable temporal delays between two sources, ranging from -130 fs to several picoseconds. We detailed the mechanical specifications and

degrees of freedom for the movement of the ODL mirrors, emphasizing their importance for optimal alignment.

Using ray-tracing simulations in COMSOL, we assessed how mirror misalignment can affect the beam at the sample position. The analysis demonstrated how adjustments in mirror movement and rotation influence the beam shape and position, providing valuable insights for future users to align the mirrors effectively for optimal source positioning. We also introduced various methods for mirror alignment, confirming that the motorized movement available are sufficient to correct misalignments caused by transportation.

The optical properties of the ODL mirrors were also discussed, highlighting the reasons for selecting silicon as the substrate and B_4C as the coating material. We explained our choice of a 9 mrad grazing incidence angle, and investigated the dependence of reflectivity and penetration depth on photon energy and grazing angle.

Surface quality and roughness measurements of the mirrors indicated that they meet acceptable standards. Simulations using SRW and SHADOW on OASYS confirmed the good quality of the mirrors. We also addressed the cooling system for the first mirror, detailing its design and operation. The cooling system, which utilizes a nickel-coated copper bar mounted 100 µm from the mirror, effectively manages heat load to mitigate its impact on beam size. The first mirror is cooled with water, while the others remain uncooled, as most heat is absorbed by the first mirror.

Finally, we investigated the critical issue of damage thresholds for single and multi-pulse. For single-shot applications, users intending to employ high pulse energy and photon energy are advised to open some undulators upstream of the ODL to prevent potential damage. Given the proximity of the ODL mirrors to the source, thorough simulations of heat load and damage thresholds are imperative. Numerical solutions of the heat equation were performed using finite element analysis (FEA) in COMSOL Multiphysics to predict temperature increases due to the European XFEL beam. We analyzed the role of heat accumulation on multi-pulse damage to silicon coated with B_4C, exposing the mirrors to 300 pulses per train with different energies at a 4.5 MHz repetition rate. Our findings indicate that heat accumulation is a significant factor, particularly when the time duration between pulses is as short as 222 ns, leading to insufficient time for complete heat dissipation.

In the subsequent chapter, we will examine in more detail the damage thresholds for B_4C and silicon, offering a more comprehensive discussion on these critical aspects.

CHAPTER 4 Damage Investigation under Grazing Incident Angle Condition

4.1 Motivation

XFEL facilities provide a significant advantage compared to other X-ray sources by generating ultra-high-intensity X-rays in short pulses, making them suitable for a diverse range of scientific applications. These FEL pulses exhibit exceptionally high peak power and ultrashort durations, produced within a narrow wavelength band. At the European XFEL, up to 2700 X-ray pulses can be delivered in trains lasting 600 microseconds at a repetition rate of 10 Hz [26].

Despite their utility, such intense pulses pose a risk of damaging optical elements and degrading beam quality. The high fluence output and short pulse durations create considerable challenges for optical components. Consequently, it is crucial to comprehend the fluence thresholds of X-ray optical coatings. The use of intense X-ray pulses is dependent upon the ability of optics to withstand the full intensity of the XFEL beam. Therefore, optical elements for XFEL applications—such as monochromators, mirrors, focusing optics, and slits—must be of high quality and capable of tolerating these intense pulses. Experimental determination of the damage thresholds for these optical materials is essential for the effective design of XFEL beamline optics.

Investigating the damage thresholds of optical elements is particularly critical for Optical Delay Line (ODL) mirrors for two key reasons. First, ODL mirrors are positioned very close to the source (approximately 5 m), resulting in a significantly small beam size and high power on the mirrors. In contrast, other optical elements are located further from the source, often over a hundred meters away in the photon tunnel. Second, the clear aperture of the ODL mirrors is only 6 mm wide, located at the edge. If damage occurs in a line on the mirror, there is insufficient space to shift the mirror to a clean area, making replacement costly and time-consuming.

To address these concerns, we aimed to determine the damage threshold of B_4C coating on a silicon substrate when exposed to soft X-ray radiation at a grazing

incidence angle of 9 mrad. As discussed in the previous chapter, Boron carbide (B_4C) is the preferred coating material for reflective mirrors at the European XFEL due to its excellent thermal properties, high melting point, low density, and the use of low atomic number elements. These latter two properties enhance the attenuation length by distributing absorbed energy over a larger volume and increasing reflectivity. However, this comes at the cost of reducing the critical angle at which the mirror can operate. Our objective is to evaluate the performance of this material and determine the safe limits for utilizing the ODL. The findings from this chapter will be invaluable for the European XFEL database and beneficial for future users of the ODL.

4.2 Damage Threshold with Considering Electron Collision Length

It is possible to estimate the irradiation tolerance of optical materials by comparing the absorption dose with the melting dose. For the design of optical components, the melting dose serves as a reasonable reference point.

The fluence damage threshold for mirrors is higher than the values obtained under normal incidence conditions, primarily because a significant fraction of the pulse energy is reflected by the mirror. Moreover, in grazing incidence conditions, the beam footprint is considerably larger, which reduces the effective fluence compared to that observed under normal incidence.

As discussed in the previous chapter, the damage threshold fluence can be calculated from the melting dose D_{th} as follows [84, 95–102]:

$$F_{th} = \frac{D_{th}\rho N_A d}{A(1-R)sin\theta} \tag{4.1}$$

In this equation, ρ, N_A, A, R, and θ represent the density, Avogadro constant, atomic weight, reflectivity, and grazing angle, respectively. Boron carbide (B_4C) has an estimated melting dose D_{th} of 0.62 eV/atom [85]. In the section 3.7.1, we defined d as Z_{pen} (the penetration depth, indicating how deeply the beam penetrates the material, depending on the photon energy, material properties, and grazing angle). However, this description is not entirely accurate, as the variable d refers to the energy deposition depth, defined as follows:

$$d = \sqrt{d_e^2 + Z_{pen}^2} \tag{4.2}$$

Here Z_{pen} is the X-ray penetration depth which is calculated using equation (3.19) or from Ref. [68] and d_e is the electron collision length, resulting from charge

accumulation in the irradiated layer as a large number of electrons attempt to leave the thin layer in a short period of time. Thus, the energy deposition depth d is a function of Z_{pen} and d_e. Electron collision lengths typically range from 1 to 100 nanometers, depending on the material and the photon energy [95]. Under normal incidence, the Z_{pen} is on the order of several micrometers, while d_e is in the nanometer range, allowing us to neglect it. However, under grazing incidence, such as for B_4C at 1 keV, the Z_{pen} is approximately 3 nm, d_e is around 10 nm, becomes significant and plays an essential role in the calculation of threshold fluence under grazing conditions. Fig. 4.1 illustrates the effect of incorporating d_e into the calculation of d. In Fig. 4.1a, the penetration depth Z_{pen} is shown as a function of grazing angle, while Fig. 4.1b compares two cases: the red line represents $d = Z_{pen}$ (with $d_e = 0$), and the green line represents $d = \sqrt{d_e^2 + Z_{pen}^2}$. Below the critical angle (32 mrad for B_4C at 1 keV), the inclusion of d_e is essential and significantly affects the calculation of d. However, above the critical angle, Z_{pen} becomes significantly larger than d_e, rendering d_e negligible in the calculation of d.

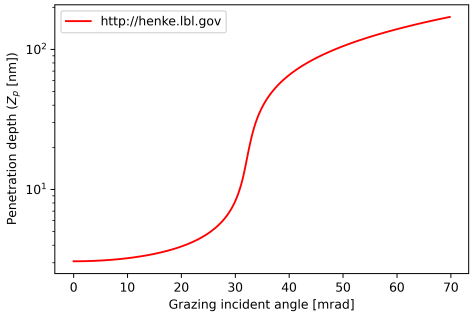

(a) Penetration depth versus grazing angle derived from Ref. [68]

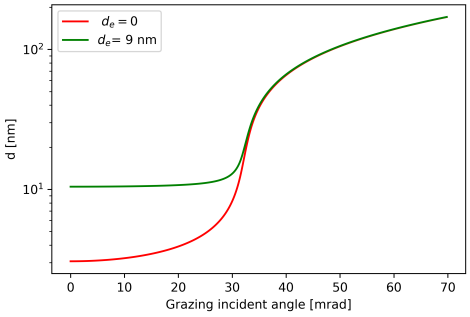

(b) Energy deposition depth with and without consideration of electron collision length.

Figure 4.1: Penetration depth and energy deposition depth as functions of grazing angle for B_4C at a photon energy of 1 keV. This figure demonstrates the importance of including d_e in damage calculations, particularly below the critical angle, where it significantly affects the energy deposition depth.

When an X-ray photon is absorbed by a material, it transfers its energy to the electrons, resulting in the creation of photoelectrons and subsequent Auger decay. In the process of photoabsorption, X-rays interact with inner-shell electrons, leading to photoionization. This process results in the emission of photoelectrons, which escape the atom, leaving behind a core hole. The kinetic energy of the emitted photoelectrons depends on the photon energy and the binding energy of the core electrons. Subsequently, an outer-shell electron fills this core hole, emitting energy; this extra energy is then utilized to ionize a second outer-shell electron, which also leaves the atom, a phenomenon known as Auger decay, as illustrated in Fig. 4.2. As a result, the ion retains two or more valence shell holes. The Auger processes

occur on the order of less than 10 femtoseconds, while the thermalization of the photo-ionized and Auger electrons takes around 20 femtoseconds. These free electrons interact with other neutral atoms, leading to their ionization, and also collide with other free electrons, causing the electrons to slow down and lose energy. The electrons eventually thermalize with the ions and neutral atoms within the material, and finally recombine with ions, a process that takes place over several hundred femtoseconds. During this time, the electrons reach a high temperature while the structure remains at a low temperature. The thermalization process between the electrons and the lattice extends over picoseconds until the thermal equilibrium is reached [85, 92, 97, 103, 104].

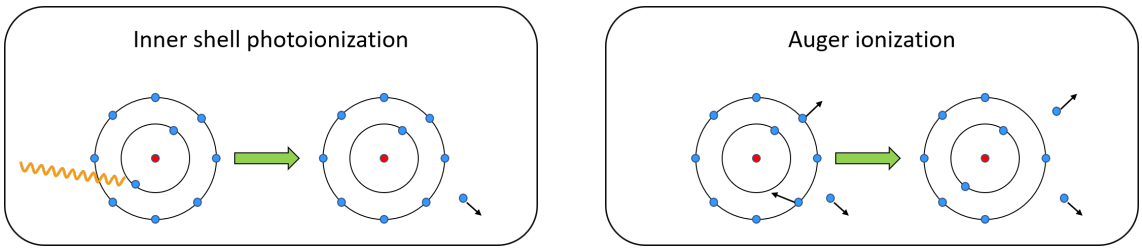

Figure 4.2: Fundamental mechanisms of X-ray and electron interactions in materials.

During femtosecond pulse events, the electron system can transport energy far beyond the absorption layer. Understanding the fundamental processes that contribute to increasing the damage threshold is crucial for designing optics capable of withstanding higher instantaneous power and optimizing scientific instruments for XFELs.

The only reliable methods to determine this parameter are Monte Carlo simulations, such as FLUKA, PENELOPE, and GEANT4, or experimental approaches [82, 96, 97, 105–109]. As of the time I am writing my thesis, there are no available results for extracting the electron collision length (d_e) for soft X-rays at 1 keV with a boron carbide (B_4C) coating. Consequently, we have decided to conduct damage tests to measure this parameter and investigate the benefits of using B_4C as a coating on silicon.

4.3 Damage Experiment at SQS Instrument

4.3.1 Experiment Setup

The experiment was conducted at the Small Quantum Systems (SQS) XFEL instrument in April 2023, under proposal number 900332. The facility delivered X-ray pulses with an average pulse energy of approximately 4.4 mJ and a pulse

duration of 25 fs, operating at a photon energy of 1 keV, which is commonly used for the upcoming ODL applications. The repetition rate during the experiment was 1.14 MHz, corresponding to a time interval of 877 ns between each pulse.

The samples analyzed in this study were polished silicon wafers with the dimensions of 29.8 mm in length, 19.8 mm in width, and between 1830 and 1870 µm in thickness. Two of these wafers were coated with a 50 nm thick layer of B_4C using DC magnetron sputtering, similar to the ODL mirrors coated at the Helmholtz-Zentrum Hereon in Geesthacht, Germany. The coating density was slightly less than that of bulk B_4C, at 2.37 g/cm^3 (approximately 94% of crystalline B_4C) [110]. One of the samples remained uncoated to compare the damage thresholds for silicon with and without B_4C coating.

Prior to the experiment, we examined the samples using a Keyence microscope and Scanning Electron Microscope (SEM) to identify any scratches or damage. Additionally, we assessed the surface roughness using a white light interferometer, both before and after coating, to ensure sample quality. Random measurements across the samples indicated an average roughness of 0.74 nm RMS. Fig. 4.3 illustrates the measurement setup along with an example of one roughness measurement.

The sample holder, depicted in Fig. 4.4, was designed to accommodate all samples and was constructed from stainless steel, which was mechanically polished to ensure a high level of flatness. The holder was then cleaned with isopropanol to maintain cleanliness in the vacuum.

Two imprint samples were used to analyze the beam profile by examining the damage spots under normal incidence conditions. These imprint samples were CVD (Chemical Vapor Deposition) diamonds in dimensions of 10 × 10 × 0.5 mm, coated with lead iodide (PbI_2) to a thickness exceeding 30 nm. This coating was chosen for its high X-ray absorption capacity, making it suitable for beam characterization and profile definition, as will be elaborated in the next section.

The schematic of the experimental setup is shown in Fig. 4.5. Utilizing an X-ray gas monitor (XGM), we were able to measure pulse energy (Appendix B.1 briefly explains the XGM). Two XGMs were employed: one located in the tunnel, which recorded the incident pulse energy for each damage measurement, with a maximum deliverable pulse energy of 5.5 mJ. The second XGM, positioned before the KB optics in the SQS instrument (referred to as the X-ray gas monitor detector, XGMD), allowed for additional monitoring [111]. A gas attenuator (ATT) was inserted after the first XGM to adjust the pulse energy and, consequently, the fluence (Appendix B.2 briefly explains the gas attenuator). Taking into account beamline transmission (42%) and KB transmission (80%), the maximum deliverable pulse energy to the samples was limited to 1.8 mJ. The beamline transmission was evaluated by comparing readings from the XGM in the tunnel and the XGMD before the KB mirrors

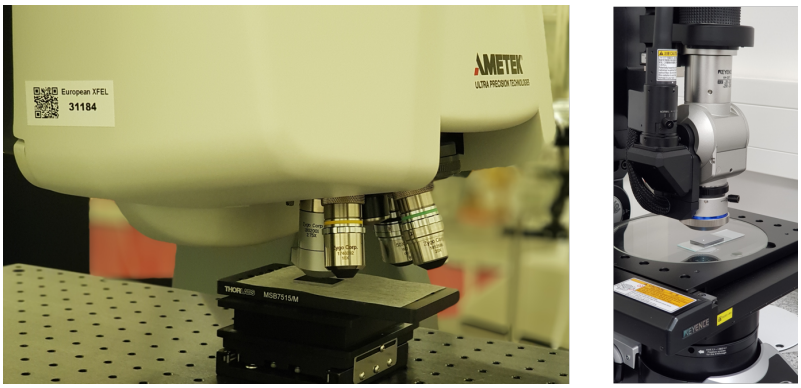

(a)

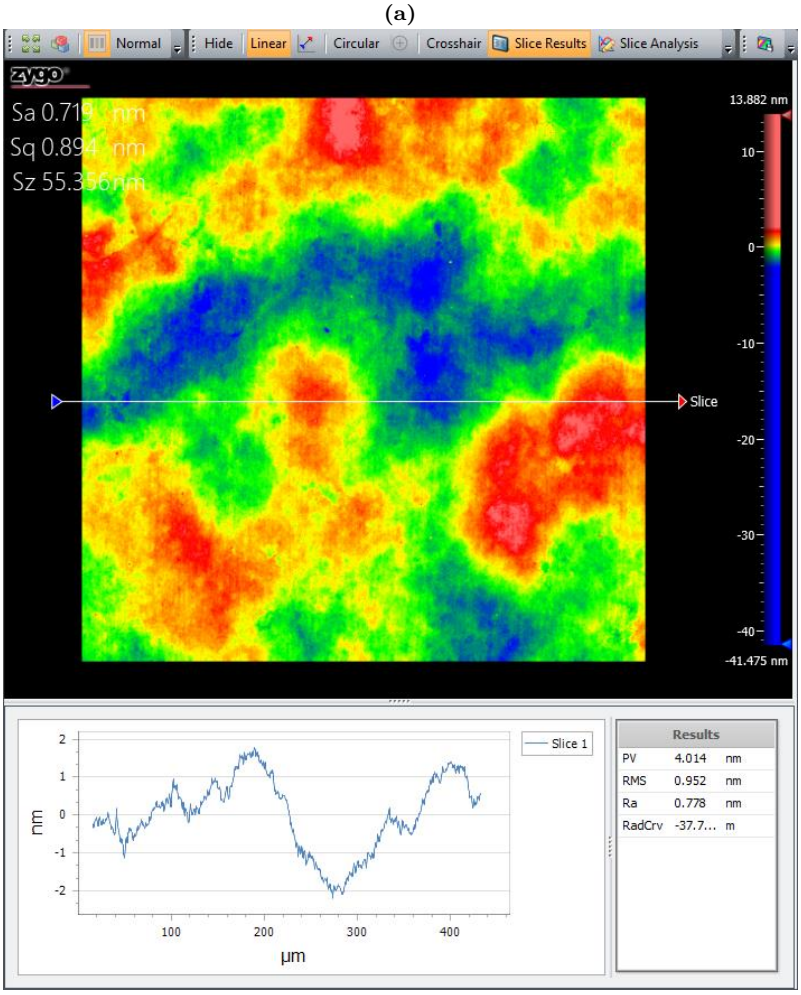

(b)

Figure 4.3: Overview of the measurement setup used to assess sample roughness and surface quality. In image (a), the left side shows the White Light Interferometer (Zygo), while the right side depicts the Keyence microscope. Image (b) shows an example roughness measurement of a silicon wafer coated with B_4C.

under conditions of empty gas attenuator settings (100% transmission) (Fig. 4.6)[1].

[1]The transmission of the photon beam from the undulator to the interaction region at SQS is influenced by the reflectivity of the mirrors and the geometric aperture of beamline elements. Mirrors typically achieve a reflectivity above 90%, but at photon energies below 1500 eV, the increasing divergence of the FEL beam can cause overfilling of the reflective surface. This can be mitigated

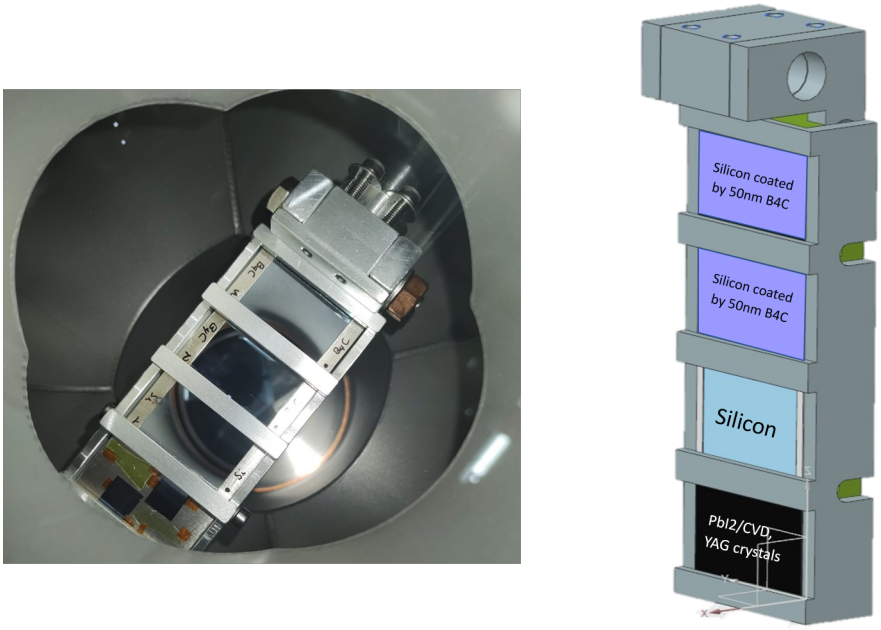

Figure 4.4: Sample holder.

The number of shots was controlled using a bunch pattern configurator. The vacuum pressure was maintained below 10^{-7} mbar (or 10^{-5} Pa).

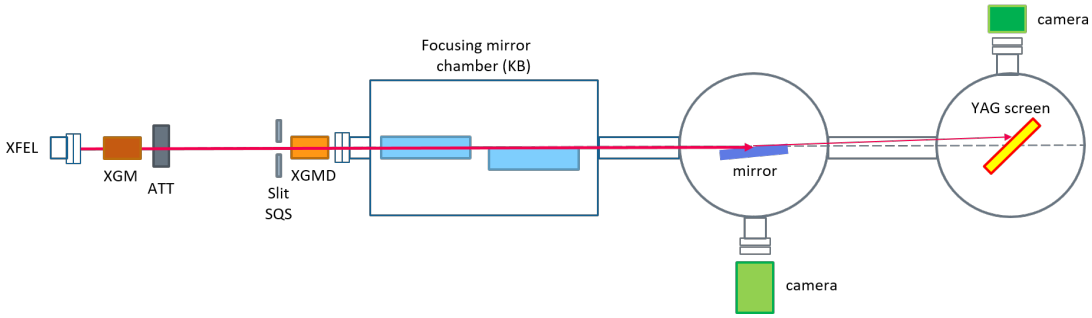

Figure 4.5: Schematic of the experiment setup. XGM: X-ray gas monitor, ATT: attenuator, XGMD: X-ray Gas Monitor Detector in SQS instrument.

A pair of KB optics was employed to focus the beam onto the samples. In addition to the imprint samples, a YAG screen was attached to visualize the beam. By adjusting the parameters of the KB optics, we achieved optimal focusing and gained preliminary estimations during the experiment prior to analyzing the imprint samples.

The experimental setup is depicted in Fig. 4.7, with the bottom image showing

by increasing the grazing angle to a maximum of 20 mrad for lower photon energies. Additional factors include the vacuum level throughout the beam transport and potential contamination or surface damage on mirrors like the Mirror3 (Fig. 2.7), which has experienced extensive beam use.[29, 112]

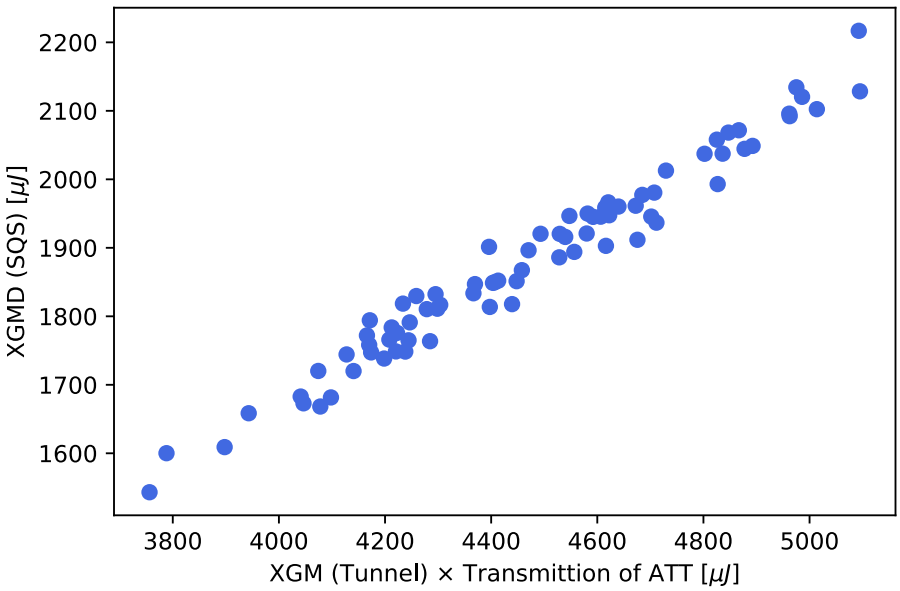

Figure 4.6: Comparing the XGM in the tunnel with the XGMD before the KB mirrors at 100% transmission of ATT, resulting in the beamline transmission 42% with a standard deviation of 0.006.

the other side of the arrangement. This setup featured two vacuum chambers: one for the mirrors and the other for the YAG screen and B_4C blocker. A rectangular YAG screen was affixed to the B_4C blocker for alignment purposes, while the B_4C block was used to prevent reflected beams from reaching the end of the beamline and causing unintended damage. Fig. 4.8 illustrates the YAG screen and B_4C blocker with their holder. The YAG screen was located 658.8 mm downstream of the mirror, allowing to track both the direct beam and its reflections. Two charge-coupled device (CCD) cameras were used for observing the mirror and YAG screen.

Alignment is performed as follows: Before inserting the mirror, the position of the directed beam on the YAG screen is measured and noted as point 'a'. After inserting the mirror, the position of the reflected beam is recorded as point 'b', and the distance between the mirror and the YAG screen is measured as 'c' (as illustrated in Fig. 4.9). Consequently, the grazing angle is calculated using the formula: $\tan(2\theta) = \frac{|a-b|}{c}$.

Additionally, the mirrors were mounted on high-precision stages (manipulator) with a motion range of 50 mm along both the X-ray beam axis and vertically to the beam, and 100 mm horizontally perpendicular to the X-ray axis. The rotation stage had a full range of motion from 0 to 360°, with an accuracy of 0.02 mrad. The mirrors were measured at grazing angles of 9 mrad, as well as angles of 15 and 19 mrad. At 1 keV, all these angles remain below the critical angle of 32 mrad [68].

In Fig. 4.10, one can see the B_4C mirrors after damage experiment, with the

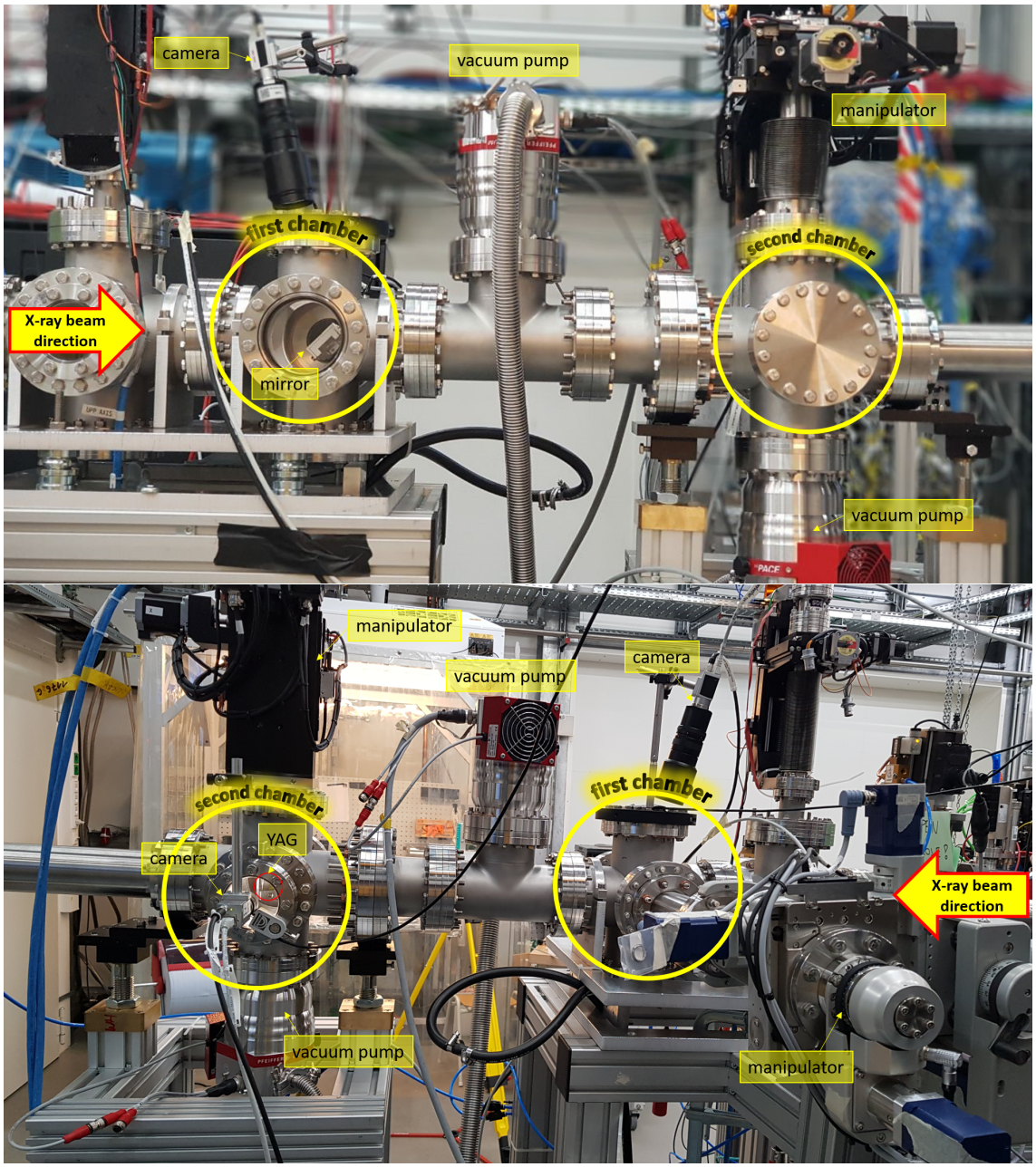

Figure 4.7: Experimental setup for X-ray beam alignment and damage test. In the upper figure, the setup is shown from the front, with the X-ray beam entering from the left. The first vacuum cross chamber holds the mirror, with a camera mounted above this chamber to observe the mirror and the damage lines. Following the mirror chamber, the second vacuum cross chamber holds the YAG screen. In the bottom figure, the setup is shown from the opposite side, with the X-ray beam entering from the right. A side-mounted camera on the second chamber observes the YAG screen.

right image captured using the Keyence microscope.

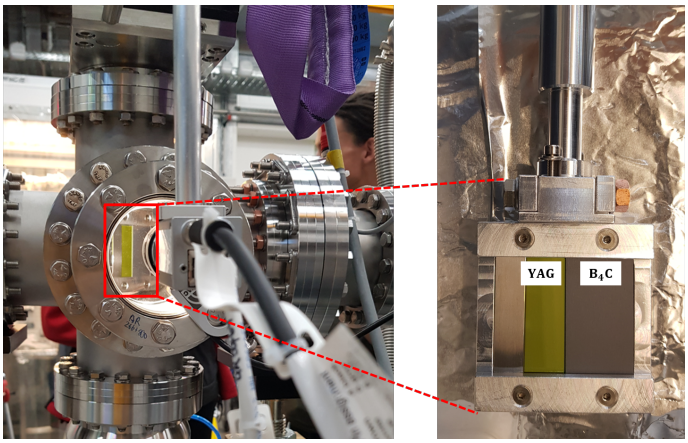

Figure 4.8: Illustration of the YAG screen and B_4C blocker used for mirror alignment and to prevent unwanted reflections. In the right image, the YAG screen and B_4C blocker are mounted on their respective holders. There is a thick layer of B_4C to act as a blocker, followed by a thin layer of YAG, which is clammed to the B_4C using an aluminum foil. In the left image, the YAG screen and B_4C blocker are shown inserted into the second chamber.

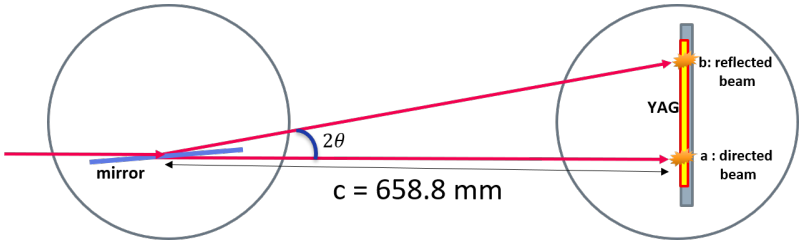

Figure 4.9: Schematic of the mirror alignment setup, showing the directed beam position (a) and the reflected beam position (b) on the YAG screen, with a separation distance (c) used to calculate the grazing angle θ.

4.4 Beam Profile

To determine the threshold fluence, defined as pulse energy divided by beam size, we measure the energy using the XGM, and thus knowing the exact size of the beam is crucial. While the beam can be observed on the YAG screen, precise measurements of its dimensions are challenging. To accurately characterize the beam profile, we inserted two imprint samples. The imprint samples consisted of PbI_2 deposited on a CVD diamond substrate, with a thickness of more than 30 nm. PbI_2 is commonly used for fluence scanning in X-ray laser beam profile characterization due to its high absorption capabilities. The samples were irradiated at normal incidence to determine the transverse profile of the incident beam. After the experiment, we analyzed the imprints using a Keyence microscope. The transverse profile of the incident beam can be derived from the shape of the ablative imprints created by individual X-ray pulses, as documented in references [113–119]. The method for determining the beam size is explained in the following section.

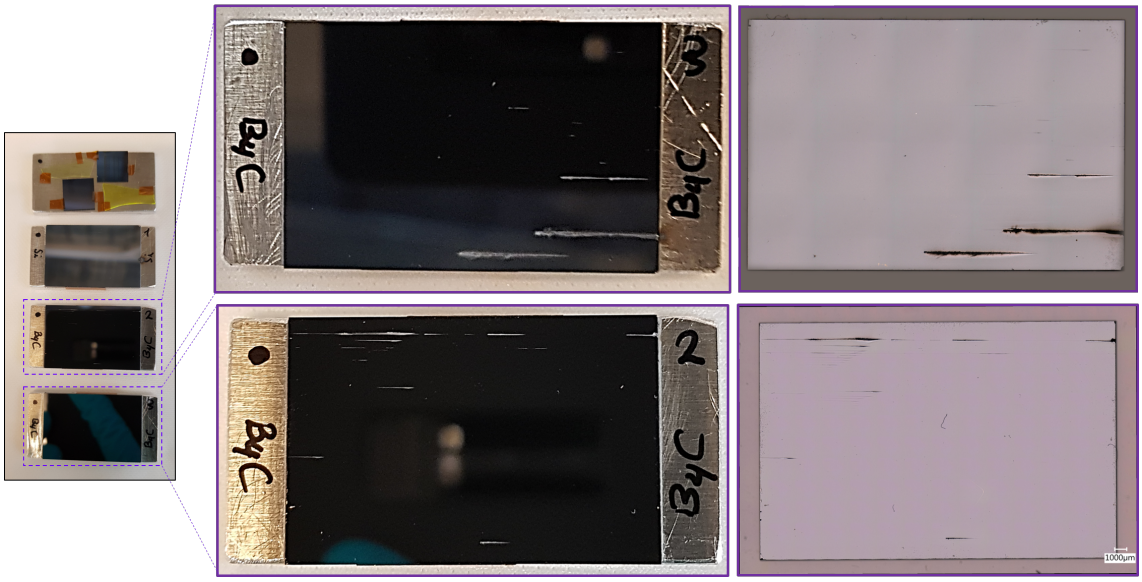

Figure 4.10: Images of B_4C-coated mirrors after damage test, mounted on their plate. The damage lines from higher pulse energies are clearly visible on the samples. The image on the right was captured using a Keyence microscope, providing a more detailed view. In the next sections, a zoomed-in view of the Keyence microscope image reveals additional damage lines from lower pulse energies.

It is noteworthy that, after the experiment, we discovered that the beam was not Gaussian, as illustrated in Fig. 4.11.

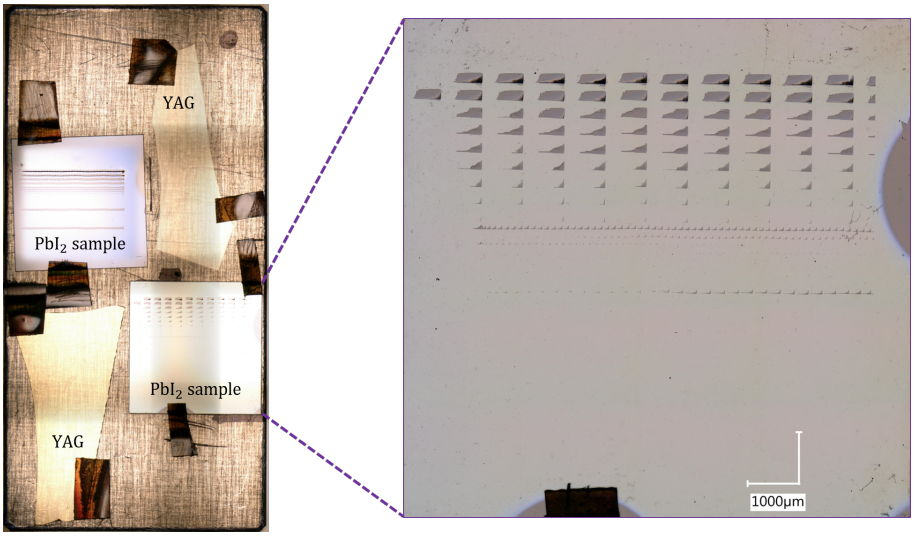

Figure 4.11: Imprint sample demonstrating a non-Gaussian beam profile. On the left, two PbI_2 imprint samples are shown after the damage test, attached to a plate with copper tape. The right image provides a close-up view of one imprint sample, captured with a Keyence microscope. Each spot represents an ablative damage site created by the X-ray beam, with each line corresponding to progressively lower pulse energies. The non-uniform shape of the spots indicates a non-Gaussian distribution in the beam profile.

4.4.1 Theory of Beam Profile Measurement

The method for determining the beam profile involves selecting an imprint sample with a known threshold fluence (F_{th}), the fluence level above which material damage occurs. The sample is positioned in front of the beam at normal incidence. A damage spot is created on the imprint sample using a single pulse. After each pulse, the sample is repositioned, and the process is repeated at various pulse energies to create additional damage spots. This process is referred to as a fluence scan (f-scan) in the transverse x and y directions, with the z-axis fixed along the beam propagation.

In a Cartesian coordinate system, the general spatial fluence distribution of a propagating beam can be expressed as [114, 120]:

$$F(x, y, z) = F_0(z) f(x, y, z) \tag{4.3}$$

Where, $F_0(z)$ represents the peak fluence and $f(x, y, z)$ denotes the normalized beam profile. Since we are only concerned with the transverse beam profile at a specific z-position, the z-coordinate is omitted in the following equations.

The pulse energy (E_{pulse}) can be calculated as a two-dimensional integral of $F(x, y)$ over the x and y coordinates in the transverse plane:

$$E_{pulse} = \iint F(x, y)\, dx\, dy = F_0 \iint f(x, y)\, dx\, dy = F_0 A_{eff} \tag{4.4}$$

Effective area (A_{eff}) establishes the relation between pulse energy and peak fluence.

$$A_{eff} = \frac{E_{pulse}}{F_0(z)} = \iint f(x, y)\, dx\, dy \tag{4.5}$$

This formulation applies to a general beam profile, whether Gaussian or non-Gaussian.

With a circular Gaussian beam defined as $f(x, y) = exp[\frac{-(x^2+y^2)}{2\sigma^2}]$, we obtain $A_{eff} = 2\pi\sigma^2$ which corresponds to the beam spot area at $1/e$ of the peak fluence.

To reconstruct the beam profile, we analyze the ablative imprints formed on the sample between the threshold fluence(F_{th}) and peak fluence (F_0).

By changing the pulse energy, we can modify the maximum intensity of the beam, and therefore peak fluence (F_0). Then we measure the beam cross-section, known as iso-fluence contours, for various ratios of the threshold fluence to the peak fluence, represented as $f = F_{th}/F_0$. Each ratio f corresponds to a different fraction of the maximum fluence. The values of the threshold-to-peak fluence ratio f always fall within a range from zero to one, representing normalized fluence. Normalization is essential for standardizing the fluence ratios, making them suitable for comparison. To achieve normalization, we need to determine the threshold pulse energy E_{th}, as

f can be calculated as $f = E_{th}/E_{pulse}$. Determining the threshold energy can be accomplished by fitting the ablation contour (area of damaged spot) to the logarithm of the pulse energy. The maximum pulse energy at which no damage occurs is identified by the point of intersection in the linear fit, and this energy is defined as the threshold energy [121, 122].

With the fluence ratios normalized, we plot them against the corresponding ablation contour areas S. This graphical representation yields a normalized fluence scan curve (f-scan), where the normalized fluence $f(S)$ varies with the size of the ablation area S. Fig. 4.12 illustrates a few iso-fluence contours as solid lines.

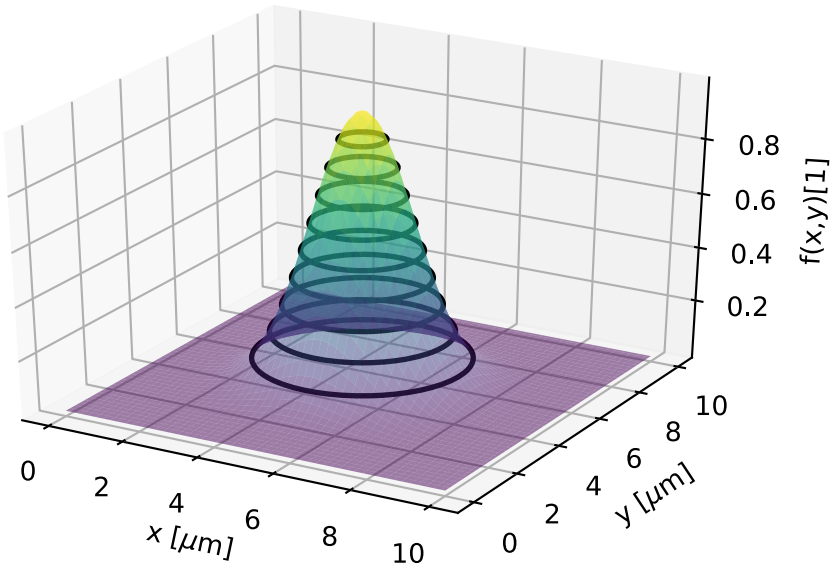

Figure 4.12: Representation of the normalized fluence profile for an ideal Gaussian beam. A few iso-fluence contours are highlighted as dark solid lines.

The relationships can be summarized as follows [114]:

$$\text{Gaussian beam:} \quad f_G(S) = \exp(-\frac{S}{A_G}) \tag{4.6}$$

$$\text{Non-Gaussian beam:} \quad f_{nG}(S) = f_1 \exp\left(-\frac{S}{A_1}\right)^{p_1} + f_2 \exp(-\frac{S}{A_2})^{p_2} \tag{4.7}$$

Here, $A_G = 2\pi\sigma^2$ is the beam cross-section area at $1/e$ of the maximum intensity, which equals the effective beam area ($A_{eff} = A_G$) for a Gaussian beam. f_1 and

f_2 specify the amplitudes of two mutually incoherent Gaussian modes in a non-Gaussian beam. Their sum must always equal unity $f_1 + f_2 = 1$ to satisfy the normalization condition. A_1 and A_2 are the respective mode cross-section areas at $1/e$ of the maximum intensity for each Gaussian mode.

The fluence distribution $F(s)$ is given by:

$$F(S) = F_0 f(S) = \frac{E_{pulse}}{A_{eff}} f(S) \tag{4.8}$$

The area below the curves fluence scan (f-scan) corresponds to the effective area:

$$A_{eff} = \int_0^\infty f(S)\, ds \tag{4.9}$$

$$E_{pulse} = F_0 A_{eff} = \int_0^\infty F(S)\, ds \tag{4.10}$$

This relationship links the beam profile, fluence scan, and effective area for characterizing non-Gaussian beams.

4.4.2 Analyzing Experiment Result of Imprint Sample

This section focuses on the experimental methods used to measure the transverse beam profile and spot size. To determine the transverse beam profile of the incident beam and, consequently, the effective area, imprint samples were irradiated at normal incidence. The resulting ablative imprints in PbI_2 are displayed in Fig. 4.13, arranged according to decreasing pulse energy.

Achieving a perfect Gaussian beam is challenging, if not impossible, as FEL beams often exhibit significant wavefront imperfections, particularly in the soft X-ray region. Additionally, the wavefront can be distorted by optical imperfections within the beamline. In our case, the beam is neither Gaussian nor homogeneous, as evidenced in Fig. 4.13. This non-Gaussian behavior may result from diffraction at the edges of the KB mirrors, or from distortions caused by SASE or misalignments of optical elements within the beamline.

To accurately define the beam profile for non-Gaussian beams, we first need to determine the threshold energy.

In fig 4.14 the ablation contours of the imprint samples, measured using a Keyence microscope, are plotted against the logarithm of the pulse energy measured by the SQS-XGM, taking into account the transmission through the KB mirrors. This plot illustrates the relationship between the contour area S resulting from ablation and the natural logarithm of the pulse energy $ln(E_{pulse})$, yielding Liu plot [121, 123].

To determine the threshold energy, we focus exclusively on the data from the

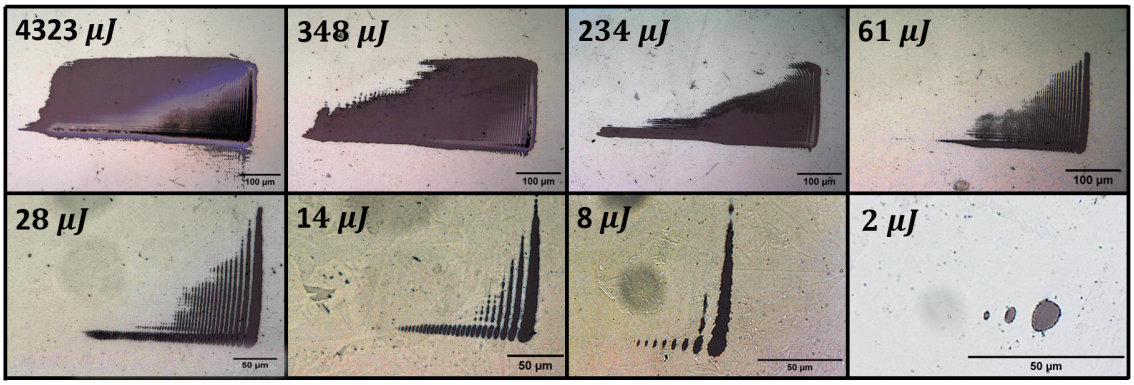

Figure 4.13: Ablative imprints in a PbI_2 sample. The PbI_2 sample was positioned normal to the beam, and imprints were created by a single X-ray shot. After each shot, the pulse energy was adjusted to create a new ablation spot. Each imprint corresponds to an individual X-ray shot. As an example, some of them are shown here with their pulse energies labeled for reference. The images are displayed in order of decreasing pulse energy, demonstrating that higher pulse energies produce larger ablation areas. The irregular shapes and sizes of the imprints reflect the non-Gaussian beam profile.

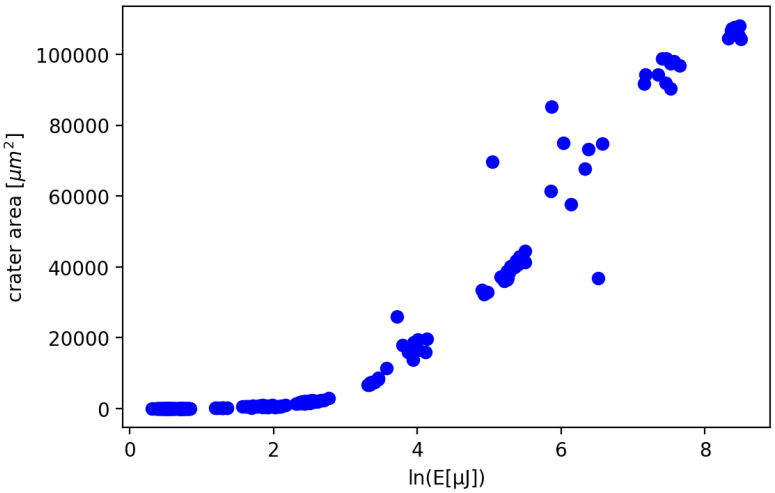

Figure 4.14: Ablation contour area S versus the logarithm of pulse energy $ln(E_{pulse})$.

lower area, specifically the "low-intensity" region, which is close to the area of interest [124]. We select the smallest imprints to observe when the damage begins to disappear. The threshold energy E_{th} can be calculated by extrapolating $S(ln(E_{pulse}))$ linearly until we reach an ablation contour area of zero, indicating that no damage occurs (i.e., $S = 0\,\mu m^2$). This results in a threshold energy of $E_{\mathrm{th}} = 1.45 \pm 0.05 \mu J$ (Fig. 4.15).

After determining the threshold energy, the beam profile is derived by fitting Eq. 4.7 to the experimental data and finding the fitting parameters shown in Fig. 4.16a. It appears that the beam has diffracted, resulting in fringe patterns, prompting

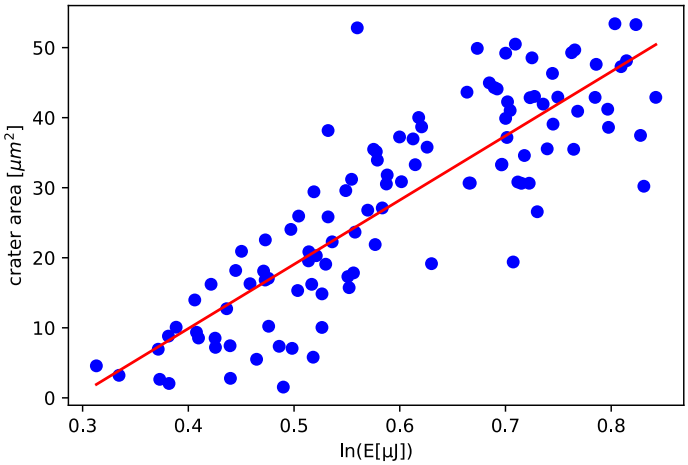

Figure 4.15: Fitted area versus logarithm of pulse energy, indicating the threshold energy.

calculations for both the entire beam and the first fringe for comparative analysis and being more accurate (Fig. 4.16). We measured the ablation contour for the first fringe and performed similar calculations. Consequently, we have beam profiles considering the entire beam and those focused solely on the first fringe.

$$f_{\text{whole}}(S) = (0.268)\exp\left(-\frac{S}{2959}\right)^{0.524} + (1-0.268)\exp\left(-\frac{S}{139}\right)^{0.698} \tag{4.11}$$

$$f_{\text{first}}(S) = (0.445)\exp\left(-\frac{S}{522}\right)^{0.641} + (1-0.445)\exp\left(-\frac{S}{97}\right)^{0.875} \tag{4.12}$$

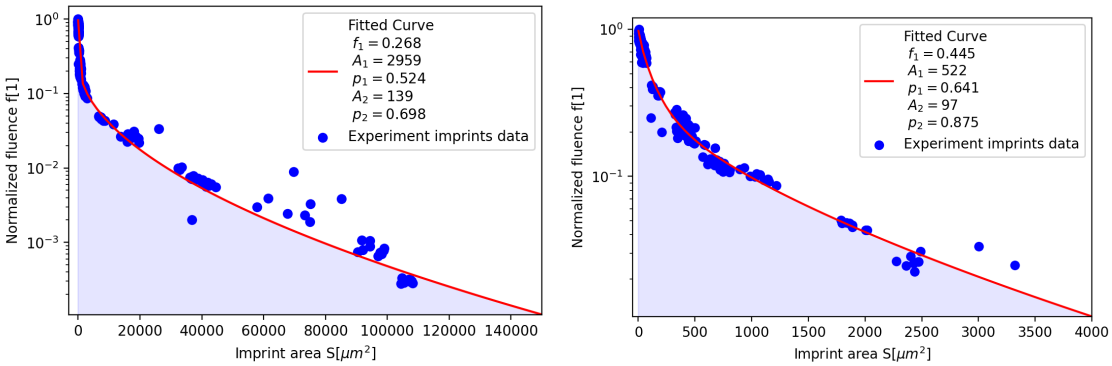

(a) Whole beam.

(b) First fringe.

Figure 4.16: Normalized fluence scan f(S) fitted with two Gaussian function.

Based on Eq. 4.9, the effective area can be calculated directly as a numerical integral of the transverse beam profile. For the entire beam profile, $A_{\text{eff}}(\text{whole}) = 1589\,\mu\text{m}^2$ and for the first fringe, $A_{\text{eff}}(\text{first}) = 380\,\mu\text{m}^2$. For grazing angles, the beam

profile is adjusted by dividing A_1 and A_2 by $\sin(\theta)$ [125].

4.5 Single-Shot Damage Experiment

To obtain the threshold fluence, the first step is to determine the corresponding damage energy threshold [98, 126]. We have performed single-shot irradiation at three different grazing angles and different pulse energy levels. As described in section 4.3.1 the pulse energy was controlled by changing the gas pressure in a gas attenuator. The average incoming FEL pule energy before the gas attenuator was on the order of 4.4 mJ. We damaged one line on the mirror at a specific attenuation level, then moved the mirror horizontally to a fresh location to create a new damage line at the next attenuation level. The pressure of the gas attenuator was changed over the range of 0.05 - 100%, corresponding to pulse energy on the sample from 750 µJ to 1.8 mJ. This attenuation range was sufficient to observe the damage threshold.

We measured the area of the damaged spot for this purpose. A total of 68 single-shot damage measurements were obtained under various fluence conditions along with 104 measurements of energy with no visible damage to the sample.

4.5.1 Single-Shot Damage of B_4C at Grazing Angle of 9 mrad

We performed single-shot irradiation for B_4C coated at a grazing angle of 9 mrad, which is below the critical angle. A representative set of damage craters captured by the Keyence microscope is shown in Fig. 4.17.

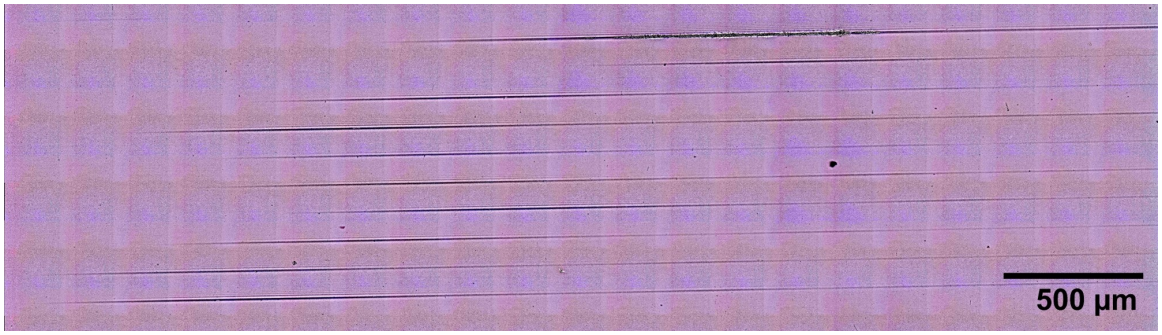

Figure 4.17: Representative single-shot damage craters at 1 keV photon energy with average pulse energy of 1.6 mJ at 9 mrad grazing angle for B_4C coating.

The beam profile is established through examination of the ablation imprints in PbI_2 explained in section 4.4.2. The grazing beam profile can be obtained by dividing A_1, A_2 by $\sin(\theta)$ as shown in the following equations:

$$f_{\text{whole}}(S) = (0.268)\exp\left(-\frac{S}{2959/\sin\theta}\right)^{0.524} + (1-0.268)\exp\left(-\frac{S}{139/\sin\theta}\right)^{0.698} \quad (4.13)$$

$$f_{\text{first}}(S) = (0.445)\exp\left(-\frac{S}{522/\sin\theta}\right)^{0.641} + (1-0.445)\exp\left(-\frac{S}{97/\sin\theta}\right)^{0.875} \quad (4.14)$$

We measured the area of the damage lines for each shot along with the corresponding pulse energy (E_{pulse}). The threshold energy E_{th} was determined by minimizing the spatial deviation of the experimental data points ($f = \frac{E_{th}}{E_{pulse}}$) from the reference beam profile. In Fig. 4.18 the normalized fluence is plotted against the damage area. The red curve represents the reference beam profile derived from imprint samples, while the black data points correspond to experimental measurements. By adjusting E_{th}, the experimental data points were aligned as closely as possible to the reference beam profile, ensuring an accurate estimation of the threshold energy.

The final values obtained were $549 \pm 116\,\mu J$ for the whole beam and $124 \pm 35\,\mu J$ for the first fringe. To account for the entire beam, we measured the area of all the fringe lines, striving for precision.

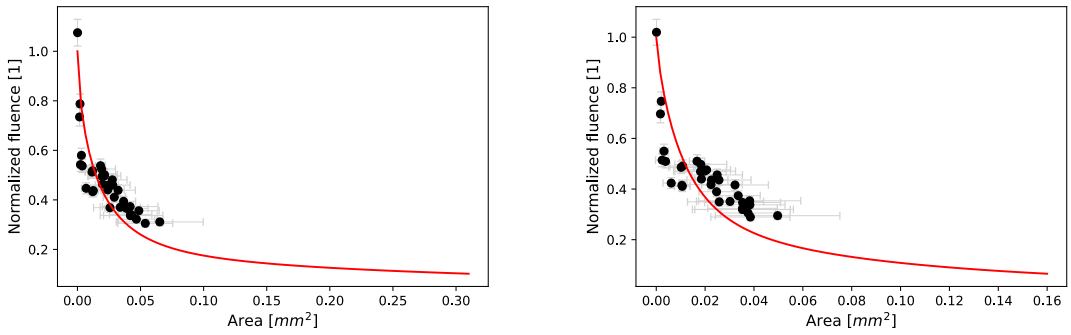

(a) Whole beam, $E_{\text{th}} = 549\,\mu J$.

(b) First fringe , $E_{\text{th}} = 124\,\mu J$.

Figure 4.18: Normalized fluence for B_4C coating at 9 mrad grazing angle.

4.5.2 Single-Shot Damage of B_4C at Grazing Angle of 15 mrad

As mentioned above, we conducted this experiment at three different grazing angles. we followed the same procedure to determine the threshold energy as we did for the 9 mrad angle, and here we present the results for 15 mrad. At 15 mrad, the threshold energy values are $E_{\text{th}} = 232 \pm 46\,\mu J$ for the whole beam and $E_{\text{th}} = 55 \pm 15\,\mu J$ for the first fringe. Fig. 4.19 shows representative single-shot damage craters at 1 keV photon energy with a 15 mrad incident angle for B_4C coating, where the fringes of each damage line are also visible.

In Fig. 4.20 illustrates the normalized fluence against area for damaged experiment data points represented by black dots, along with the fitted beam profile shown

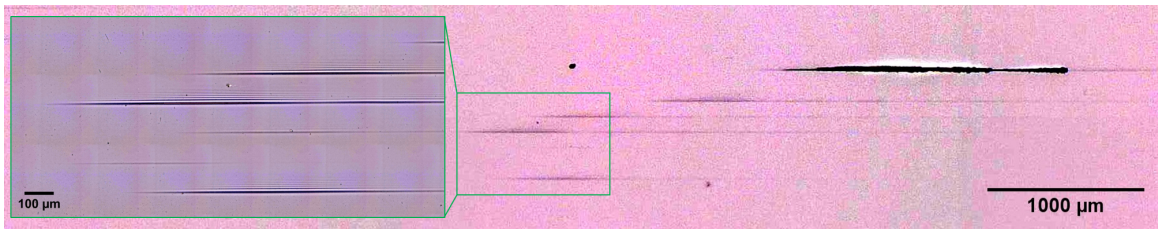

Figure 4.19: Representative single-shot damage craters at 1 keV photon energy at 15 mrad for B_4C coating.

as a red line for both the whole and first fringe of the beam. This fitting is used to determine the threshold energy.

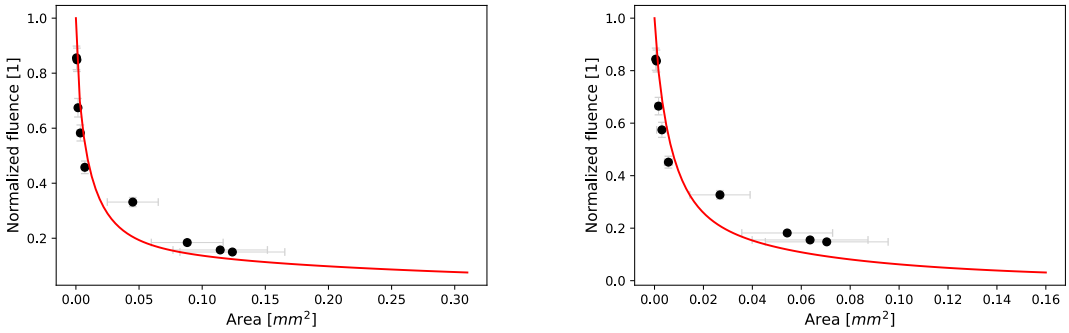

(a) Whole beam, $E_{\text{th}} = 232\,\mu\text{J}$.

(b) First fringe , $E_{\text{th}} = 55\,\mu\text{J}$.

Figure 4.20: Normalized fluence for B_4C coating at 15 mrad grazing angle.

We measured one of the highest pulse energies and transmissions using a Confocal microscope, where the damage line was distinctly visible, to assess the depth of the damage. This line was created by an incident pulse energy of 4.6 mJ (XGM), with a gas attenuator transmission of 96.09% and a pulse energy reaching the sample of 1474 µJ, at a grazing angle of 15 mrad. The depth of the first fringe was measured to be approximately 10–20 nm, indicating that the damage occurred in the B_4C coating and not in the silicon substrate (Fig. 4.21). Although we attempted to measure other lines, the narrow depth of damage made it challenging, and noise levels interfered more significantly than the actual depth. Fig. 4.22 shows this damage line as measured with the Keyence microscope.

4.5.3 Single-Shot Damage of B_4C at Grazing Angle of 19 mrad

Here, we present the results for the case of 19 mrad. At this angle, the threshold energy is $104 \pm 18\mu$J for the whole beam and $22 \pm 4\mu$J for the first fringe. Fig. 4.23 displays representative single-shot damage craters at 1 keV photon energy with a 19 mrad incident angle for the B_4C coating. Fig. 4.24 illustrates the normalized fluence versus area for both the first fringe and the whole beam. Detailed experi-

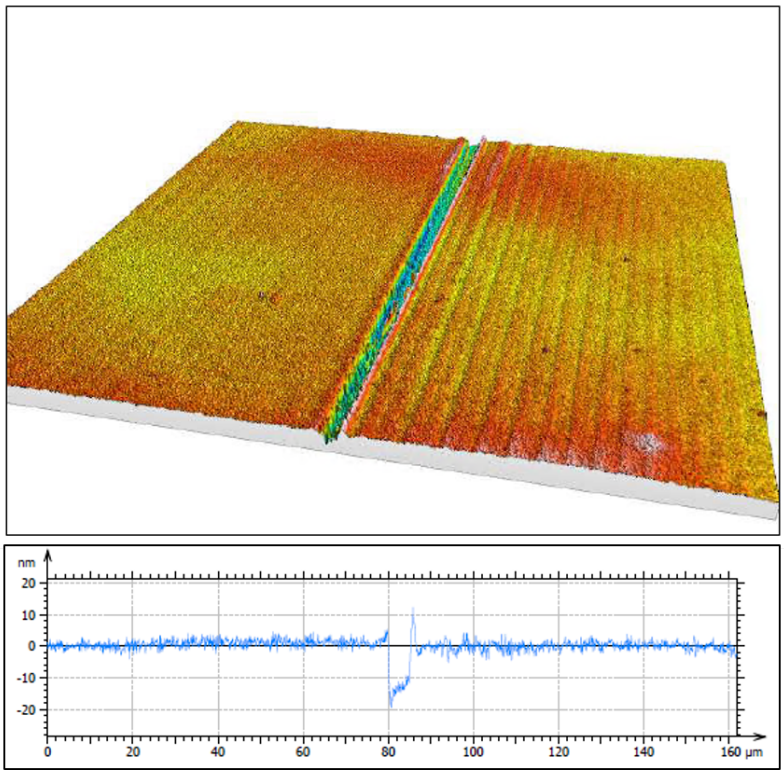

Figure 4.21: Depth measurement of damage line for $E_{\text{pulse}} = 1474\,\mu\text{J}$, θ=15 mrad using a Confocal microscope. While fringes were detected with the Keyence microscope, they are not distinctly visible here due to resolution and noise constraints.

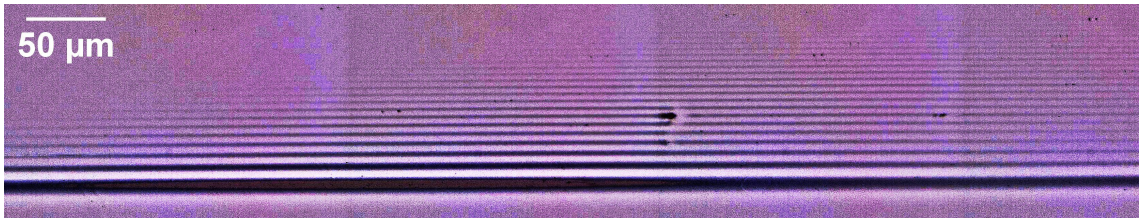

Figure 4.22: Keyence microscope image of the damage line for $E_{\text{pulse}} = 1474\,\mu\text{J}$, $\theta = 15\,\text{mrad}$.

mental data, including pulse energy and gas attenuator for each shot, can be found in Appendix B.6, which also includes data from shots without causing any visible damage.

4.5.4 Single-Shot Damage of Si and Compare to B_4C

One of our samples was an uncoated silicon substrate, for which we conducted experiments exclusively at a grazing angle of 9 mrad. The main goal of this study is to compare the damage threshold of Silicon and B_4C. The methodology employed to calculate the threshold energy was consistent with previous approaches, resulting in values of $E_{\text{th}} = 261 \pm 29$ µJ for the whole beam and $E_{\text{th}} = 60 \pm 12$ µJ for the first fringe.

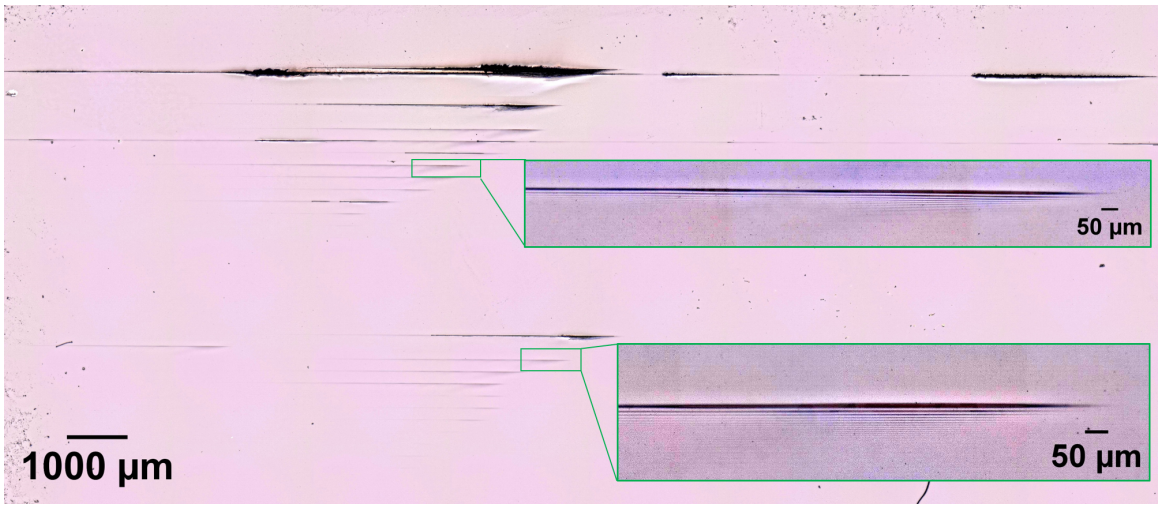

Figure 4.23: Representative single-shot damage craters at 1keV photon energy at 19 mrad incident angle for B_4C coating.

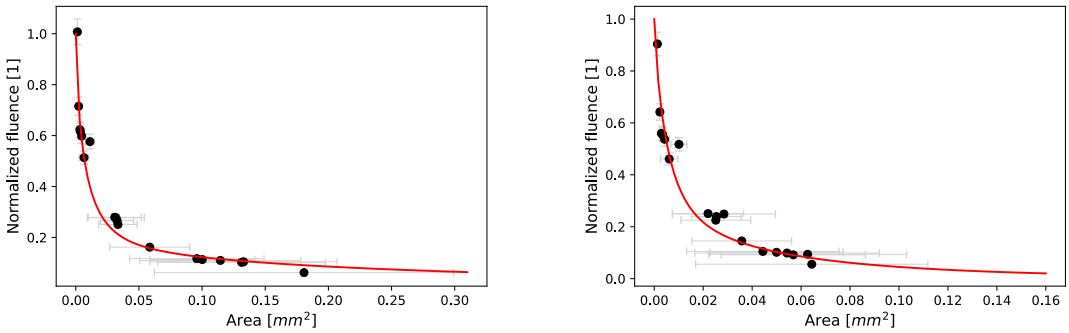

(a) Whole beam, $E_{\text{th}} = 104\,\mu\text{J}$.

(b) First fringe , $E_{\text{th}} = 22\,\mu\text{J}$.

Figure 4.24: Normalized fluence for B_4C coating at 19 mrad grazing angle.

Fig. 4.25 shows representative single-shot damage craters with a 9 mrad incident angle for the uncoated silicon. Fig. 4.26 illustrates the experimental data points (black dots) alongside the fitted beam profile (red curve).

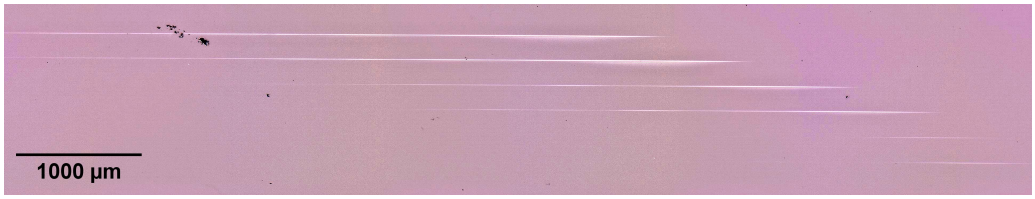

Figure 4.25: Representative single-shot damage craters at 1keV photon energy at 9 mrad incident angle for Si without coating.

In contrast, the threshold energies for the B_4C-coated samples were $E_{\text{th}} = 549\,\mu\text{J}$ for the whole beam and $E_{\text{th}} = 124\,\mu\text{J}$ for the first fringe. Consequently, the threshold fluences ($F_{th} = \frac{E_{th}}{A_{eff}}$) were calculated as $0.16\,\mu\text{J}/\mu\text{m}^2$ for silicon and $0.34\,\mu\text{J}/\mu\text{m}^2$ for B_4C, considering both the whole beam and the first fringe. As expected, boron

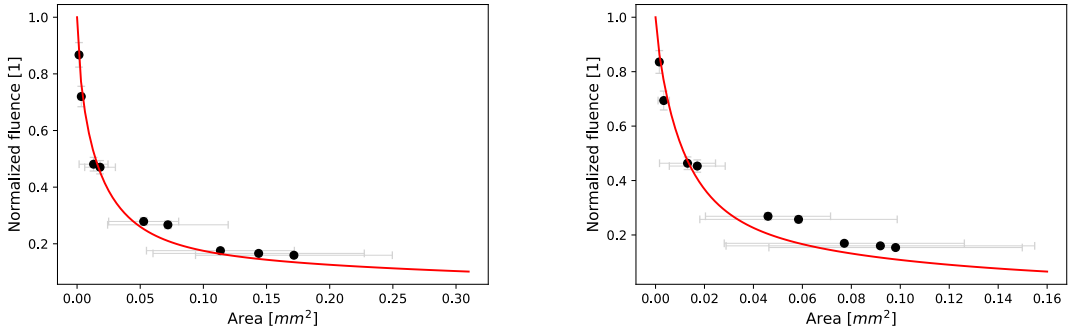

(a) Whole beam, $E_{\mathrm{th}} = 261\,\mu\mathrm{J}$. **(b)** First fringe , $E_{\mathrm{th}} = 60\,\mu\mathrm{J}$.

Figure 4.26: Normalized fluence for Si without coating at 9 mrad grazing angle.

carbide (B_4C) exhibits a damage threshold approximately twice that of silicon (Si), demonstrating the benefits of using B_4C as a coating on silicon.

4.6 Electron Collision Length

By obtaining the threshold energy for three different grazing angles, we can calculate the threshold fluence in each case ($F_{th} = \frac{E_{th}}{A_{eff}}$). Table 4.1 shows the threshold fluence at 1keV based on a measurement of the whole beam or the first fringe.

θ [mrad]	$F_{th(whole)}$ [$\mu J/\mu m^2$]	$F_{th(first)}$ [$\mu J/\mu m^2$]
9	0.35	0.33
15	0.15	0.14
19	0.06	0.06

Table 4.1: Measured grazing angles and the threshold fluences at 1keV for B_4C coating.

A plot of threshold fluence against grazing angle is presented in Fig. 4.27. The red points represent the experimentally extracted threshold fluences for grazing angles of 9, 15, and 19 mrad. The dashed red curve illustrates the threshold fluence as a function of grazing angle, based on Eq. 4.1 without considering electron collision length. We fitted the Eq. 4.1 to the experimental data points, assuming a value of $D_{\mathrm{th}} = 0.62\,\mathrm{eV/atom}$ [85, 127]. The parameter d_{e} was treated as a fitting variable, yielding values of $d_e = 8.6\,\mathrm{nm}$ for the whole beam measurement, and $d_e = 8.1\,\mathrm{nm}$, based on the measurement of the first fringe. The solid green line in Fig. 4.27 indicates the threshold fluence curve with considering of electron collision length (d_{e}).

As depicted in Fig. 4.27, the electron collision length significantly influences damage reduction at grazing angles below the critical angle. Energetic photoelec-

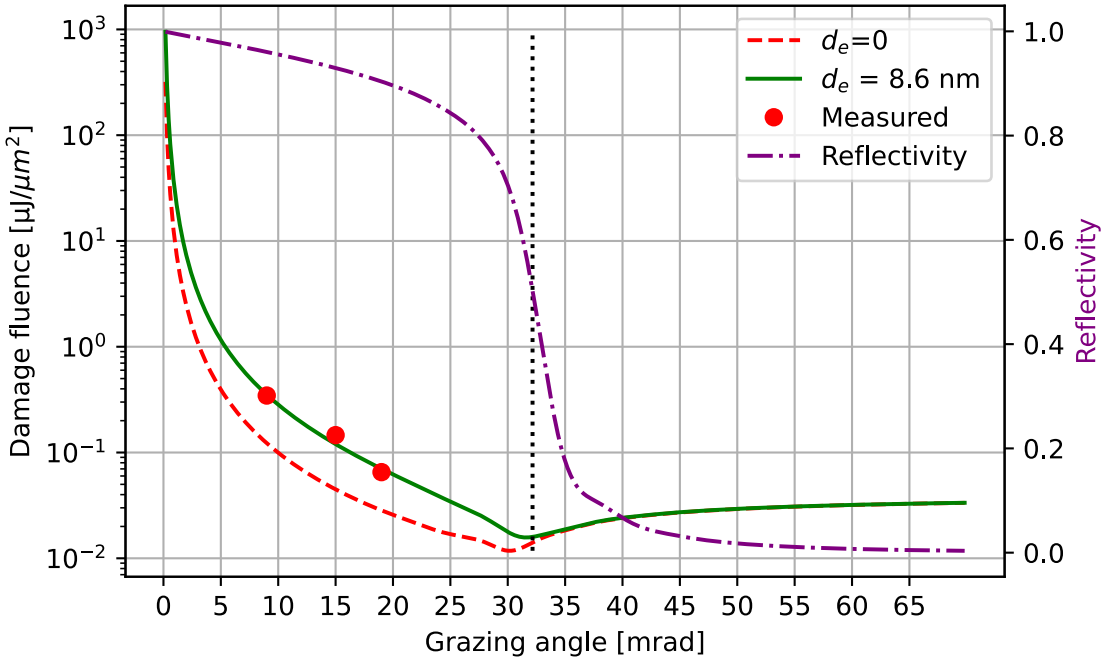

Figure 4.27: Damage fluence of B_4C at the irradiation with 1keV photon energy, plotted as a function of the grazing angle, circles indicate the measured values. Solid and dashed lines show the threshold fluence with and without considering the electron collision length. The dashed-dotted line indicates the reflectivity (right y-axis). The critical angle is indicated with the dotted vertical line.

trons generated in the X-ray interaction regions of the samples convey deposited energy into the material structure.

Fig. 4.28 presents the relative absorbed dose (dose/dose at 90° incidence) as a function of grazing angle, calculated using the Eq.3.24. The black line represents the scenario with $d_e = 0$, while the green line corresponds to $d_e = 8.6\,\text{nm}$. At normal incidence, the collision length is generally disregarded [128]; however, at grazing incidence, it significantly reduces radiation damage.

4.7 Multi-Pulse Damage Experiment

Optical components intended for XFELs must be capable of withstanding multi-pulse high-fluence irradiation. To evaluate the damage caused by multi-pulse irradiation, we conducted an experiment. Based on the electron bunch charge, the pulse duration was approximately 25 fs (FWHM), with a pulse spacing of 877 ns, corresponding to a repetition rate of 1.14 MHz. In each irradiated train, 30 or 300 single pulses were accumulated. The XGM in the tunnel recorded pulse energies for each shot. Fig. 4.29 illustrates pulse energy fluctuation during this experiment. In

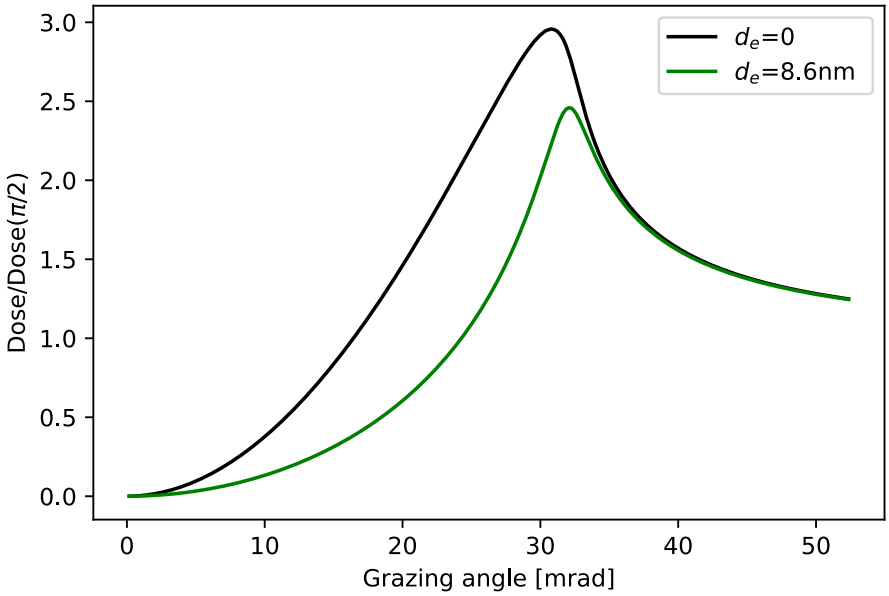

Figure 4.28: Absorbed dose for B_4C at 1keV. The scale is normalized to the dose at normal incidence, with the black line representing without d_e and the green line representing $d_e = 8.6\,\text{nm}$.

the multi-pulse damage test, the average pulse energy was 4788 µJ, with a maximum of 6385 µJ, and an energy variation of approximately 9%. The gas attenuator was used to control the mean energy of pulse trains.

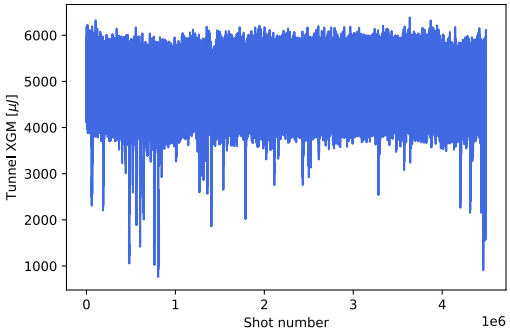

Figure 4.29: Pulse energy fluctuation for multi-pule damage test.

We conducted damage experiments for both silicon and B_4C coatings. The fluences applied were well below the single-shot irradiation damage threshold, with exposure durations of 10 seconds and 5 minutes. Table 4.2 summarizes the damage threshold fluences in experiment for B_4C coating, detailing the pulse energies and attenuator settings at which damage occurred. The experiment was performed for B_4C under four different gas attenuator parameters at different irradiation durations. In the damage column, "Yes" indicates discoloration observed on the sample surface,

signifying damage. For 30 pulses per train at an attenuator transmission (ATT) of 3% (fluence of 0.03 µJ/µm^2), damage was observed three times, but one instance showed no visible damage. This may be due to the fact that the damage threshold fluence is close to this value.

Pulse/train	Time of shootin	ATT [%]	E_{pulse} on sample [µJ]	Fluence [µJ/µm^2]	Damage
30	10 sec	10	149.45	0.09	Yes
		3	48.16	0.03	No
		3	47.61	0.03	Yes
		1	15.11	0.009	No
		0.3	4.48	0.003	No
	5 min	10	165.83	0.1	Yes
		3	47.25	0.03	Yes
		3	48.49	0.03	Yes
		1	15.12	0.009	No
		0.3	4.57	0.003	No
300	10 sec	10	170.29	0.11	Yes
		3	47.27	0.03	Yes
		3	47.33	0.03	Yes
		0.3	3.81	0.002	No
	5 min	3	45.06	0.03	Yes
		3	46.46	0.03	Yes
		1	14.83	0.009	Yes
		0.3	4.54	0.003	Yes

Table 4.2: Parameters for B_4C multi-pulse at grazing angle 9 mrad.

Fig. 4.30 illustrates a map of pulses per train as a function of fluence for B_4C at a grazing angle of 9 mrad. Green circles denote instances where no damage was detected in 30 or 300 pulses per train, while red triangles indicate observed damage. Any noticeable surface changes were classified as damage [103]. Notably, a lower damage threshold was associated with a higher number of pulses. For B_4C, damage was observed after both 300 and 30 pulses irradiation, below the single-pulse threshold fluence.

For 30 pulses per train, the damage threshold ranged between 0.009 µJ/µm^2 (no damage) and 0.03 µJ/µm^2 (damage observed), while for 300 pulses per train, it was below 0.002 µJ/µm^2. Comparatively, the single-shot damage threshold for B_4C, (0.34 µJ/µm^2) was approximately 170 times higher than the multi-pulse damage threshold for 300 pulses per train (0.002 µJ/µm^2).

For silicon, with 30 and 300 pulses per train, at the transmission of 3% and an irradiation duration of 5 minutes, where the pulse energy reaching the sample was 45 µJ, corresponding to a fluence of 0.03 µJ/µm^2, no damage was observed.

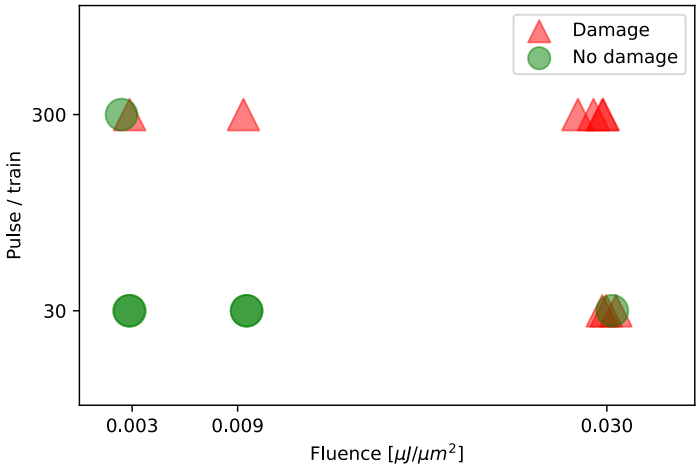

Figure 4.30: Damage map for B_4C coating at 9 mrad grazing angle. Green circles represent cases where no damage was observed, while red triangles indicate damage. The data highlight that the damage threshold decreases significantly as the number of pulses per train increases.

4.8 Simulations

4.8.1 Monte Carlo Simulation

As discussed in Section 4.2, the energetic photoelectrons and secondary electrons emitted from the mirror surface penetrate deeply into the material or even the substrate. This process significantly influences the energy deposition depth, which can be estimated using Monte Carlo simulations.

The Monte Carlo method is a widely used computational approach for modeling fundamental interactions between X-rays and electrons. It is a stochastic simulation technique based on probability and statistical theory, employing random numbers to solve the dynamic processes involved in the evolution of a system. One of its primary applications is the simulation of particle transport and collision processes within matter. The core procedure of the Monte Carlo simulation involves treating particles in a classical state, with their step sizes determined by the mean free path or total scattering cross section. Each scattering event was regarded as another random step, while the changes in angle and energy during scattering are governed by the corresponding scattering cross sections.

Several programs are available for conducting these simulations, including FLUKA, PENELOPE, and Geant4. In this study, we utilized FLUKA, a comprehensive Monte Carlo simulation package extensively employed in high-energy experimental physics and engineering. FLUKA is applicable in various fields, including shielding, detector and telescope design, cosmic ray studies, dosimetry, medical physics, and

radiobiology [129]. The FLUKA Monte Carlo method simulates the interactions of electrons, positrons, and photons with matter. The simulation begins with a source definition that specifies the primary particles (photons), their energy, and incident angles, as well as material data and geometries. We utilized the user-friendly graphical interface "Flair" for our simulations.

In the FLUKA simulation, we accounted for all effects related to photoionization, Auger processes, and fluorescence, as well as secondary electron cascades, using a substantial initial photon count of 10^7 to simulate the energy deposited and absorbed dose along the depth. Each simulation comprised 10 runs, and the results were averaged over these runs and across all primary photons. This number of initial primary photons and runs was sufficient to mitigate deviations caused by statistical fluctuations. Each simulation took approximately 45 minutes to complete.

The spatial distribution of the photons followed a Gaussian profile with $\sigma = 15.91\,\mu m$, corresponding to an effective area of $1589\,\mu m^2$ (Eq. 4.6 $A_{eff} = 2\pi\sigma^2$). The photon energy was set at 1 keV with a grazing angle of 9 mrad, and the chosen material was B_4C. The density of the material was referenced to standard conditions at room temperature, with the bulk density of B_4C being $2.52\,g/cm^3$. With the release of the updated version of FLUKA (FLUKA 2024.1, Flair-2.3-0e) on May 6, 2024, the software now computes reflection probabilities for X-rays on thick mirrors as a function of the incidence angle [130], employing a precise 3D geometry for mirror configurations. We used several option cards in FLUKA, specifically 'BEAMPART', 'ENERGY', and 'DOSE'.

Fig. 4.31 illustrates the distribution of photons within the material, as generated using the BEAMPART card.

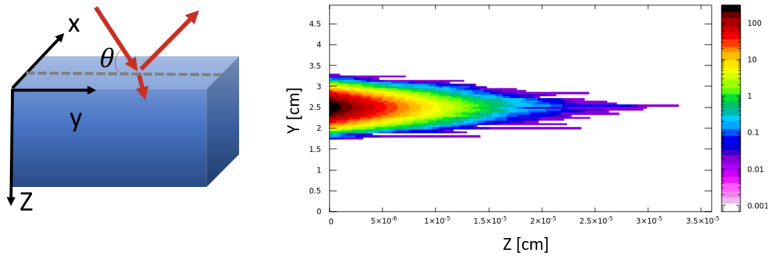

Figure 4.31: Photon distribution in the material obtained using the BEAMPART card. The left image illustrates the coordinate system used in FLUKA simulations, with the grazing angle of incidence beam denoted by θ. The right image shows the photon beam distribution in the mirror.

4.8.1.1 Absorbed Energy Fraction

The absorbed energy fraction (AEF) is defined as the ratio of deposited energy per unit depth to the total absorbed energy. Based on the Beer-Lambert equation,

the theoretical expression for AEF(z) is given as follows [131]:

$$|\frac{dI}{dz}| = \frac{1}{Z_{pen}} e^{(-\frac{z}{Z_{pen}})} \tag{4.15}$$

The X-ray penetration depth (Z_{pen}) can be calculated using Eq. 3.19.

FLUKA provided the deposited energy distribution [GeV/cm^3 per primary[2]] (Fig. 4.32a), averaged over the scoring transverse area (x, y). We multiplied this by the transverse area and divided by the total deposited energy to obtain AEF(z). Fig. 4.32b displays the AEF(z) for B_4C at 1 keV with a grazing incidence angle of 9 mrad, derived from the "ENERGY" card of FLUKA. This figure shows that the simulation results indicate the beam penetrates the material significantly deeper than predicted by Eq. 4.15, with a energy deposition depth approximately 8 times greater.

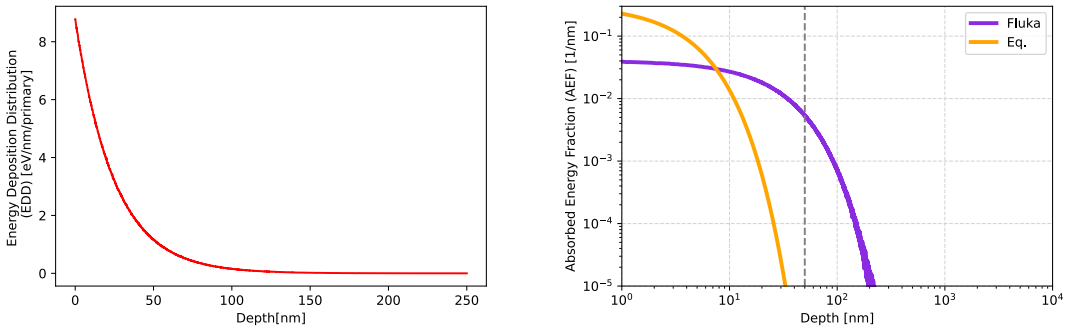

(a) Deposited energy distribution.

(b) Absorbed energy fraction AEF(z).

Figure 4.32: Energy deposition analysis for B_4C irradiated at 1 keV with a grazing angle of 9 mrad. (a) Deposited energy distribution versus depth, showing an exponential decrease as predicted by the Beer-Lambert law. (b) Absorbed energy fraction (AEF) as a function of depth. The purple curve represents the simulation results obtained from FLUKA, while the orange curve corresponds to Eq. (4.15), which considers only the penetration depth (Z_{pen}). The comparison illustrates that when accounting for the electron collision length in the simulation, the energy penetrates deeper into the material than predicted solely by the Beer-Lambert law. The vertical dashed gray line marks the 50 nm depth from the material surface, corresponding to the thickness of the B_4C layer.

4.8.1.2 Absorbed Dose

To estimate the damage to the XFEL X-ray optics, the dose distribution obtained from FLUKA simulations in units of GeV/g/primary needs to be converted to eV/atom. The conversion is performed using the formula $D = D_{FLUKA} \times 1o^9 \times N \times m_{atom}$, where N is the number of photons given by $N = \frac{E_{pulse}}{E_{photon}}$ and $m_{atom} = \frac{A}{N_A}$.

[2]Photon

Here, A is the atomic weight of B_4C is (55.2547/5 g/mol) and N_A is Avogadro constant (6.022×10^{23} atom/mol).

Fig. 4.33a shows the maximum dose of transverse area (x, y) versus depth z, while Fig. 4.33b illustrates the absorbed dose (averaged over the x-axis) versus depth Z.

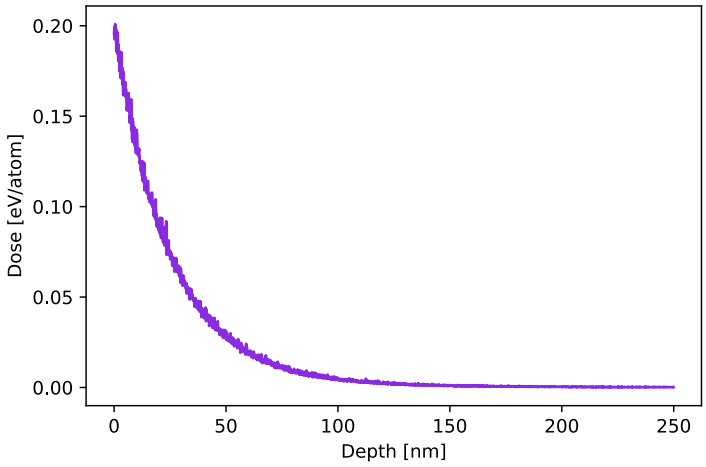

(a) Maximum dose distribution versus depth.

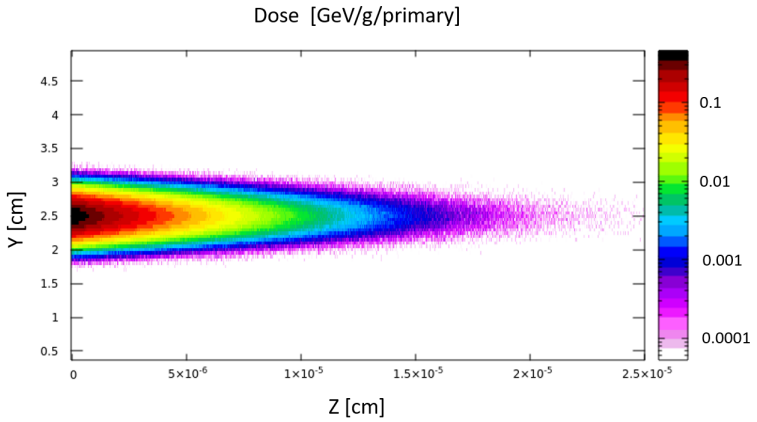

(b) Absorbed dose.

Figure 4.33: Dose calculations for B_4C. (a) Maximum dose distribution as a function of depth, showing the dose distribution peak at the surface and decreases exponentially with depth. (b) Absorbed dose map in the yz-plane, illustrating the spatial distribution of the absorbed dose within the material. The dose is averaged over the x-axis. This figure demonstrates that 85% of the beam is absorbed within the 50 nm of the mirror.

4.8.2 FEA Simulation for Multi-Pulse

In this study, we employed COMSOL Multiphysics to predict the temperature resulting from multi-pulse irradiation. The procedure followed the methodology

outlined in Section 3.7.2 and Eq.3.28. The material under investigation is 50 nm of B_4C deposited on a silicon substrate. We simplified the model to a two-dimensional heat transfer representation.

In Fig.4.34a illustrates the temperature profile versus time for a fluence of $F = 0.13\,\mu J/\mu m^2$ (with $E_{pulse} = 200\,\mu J$ and $\sigma = 15.9\,\mu m$), serving as a representative example of all COMSOL simulations, detailed in Table 4.3. Additionally, Fig. 4.34b shows the temperature distribution along the depth at $t \approx 7\,ps$.

Photon Energy	1000 eV
Pulse energy (E_{pulse})	200 µJ
Beam size (σ_x, σ_y)	15.91 µm
Fluence (F)	$0.13\,\mu J/\mu m^2$
Grazing angle (θ)	9 mrad
Penetration depth (Z_{pen})	3.37 nm
Reflectivity (R)	0.96
Time duration (σ_t)	1 ps

Table 4.3: Parameters used in COMSOL simulations related to Fig. 4.34.

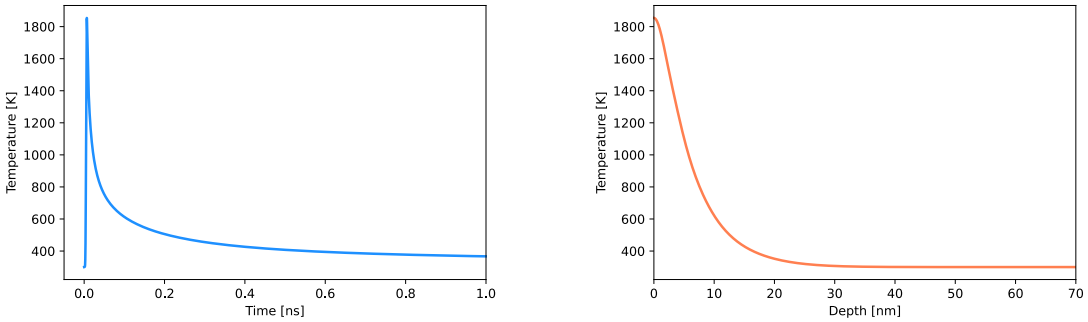

(a) Temperature versus time.

(b) Temperature versus depth.

Figure 4.34: COMSOL simulation for parameter Table 4.3. (a) Temperature versus time, showing a sharp initial rise due to beam irradiation, followed by a rapid decrease and a slower cooling phase. (b) Temperature distribution versus depth at $t \approx 7\,ps$, illustrating energy deposition within the (B_4C) and silicon layers, with the maximum temperature observed in the (B_4C) coating.

Fig. 4.35 presents a map of the number of pulses as a function of fluence, with a dotted black line indicating the melting temperature of B_4C (2623 K). In this simulation, the repetition rate is set at 1.14 MHz, resulting in approximately 877 ns between each pulse.

The time- and depth-dependent heat source equation 3.28 can be modified as follows [97, 105, 132]:

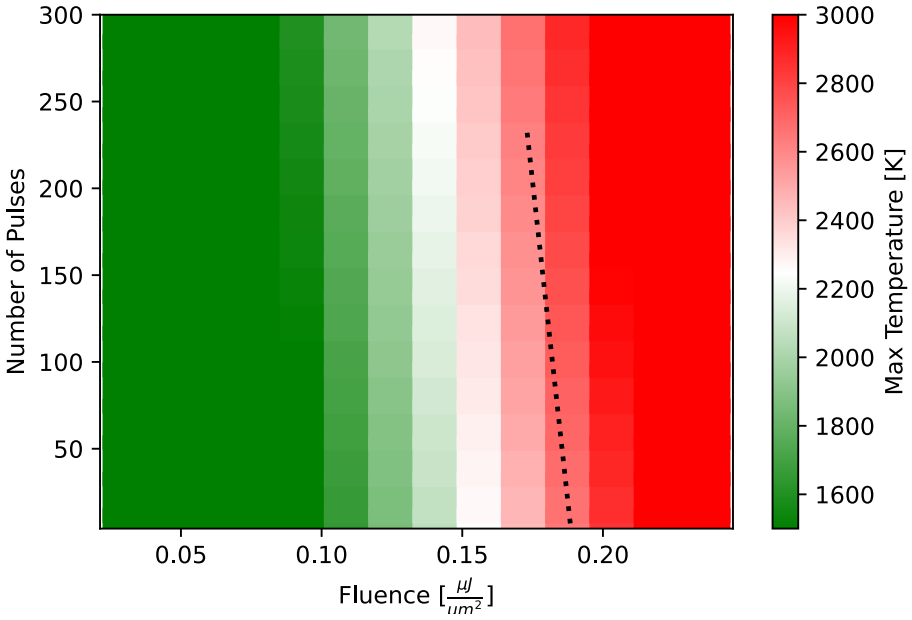

Figure 4.35: Number of pulses versus fluence, with the maximum surface temperature of the mirror represented by the color bar. The dotted line indicates the melting temperature of B_4C (2623 K). Regions in red correspond to conditions where the temperature exceeds the melting point, indicating potential damage to the mirror surface.

$$Q_{absorbed}(x,y,z,t) = (1-R)\frac{E_{pulse}\sin\theta}{(2\pi)\sigma_x\sigma_y\sqrt{2\pi}\sigma_t}\cdot e^{-\frac{(x-x_0)^2\sin^2\theta}{2\sigma_x^2}}\cdot e^{-\frac{(y-y_0)^2}{2\sigma_y^2}}\cdot e^{-\frac{(t-\mu)^2}{2\sigma_t^2}}\cdot AEF(z) \tag{4.16}$$

In this equation, AEF(z) represents the absorbed energy fraction obtained from Monte Carlo simulations, as discussed in Section 4.8.1.1. Fig. 4.36a illustrates the temperature versus time for simulations that take into account AEF (using Eq. 4.16). Additionally, Fig. 4.36b shows temperature along the depth of the material.

Fig. 4.37 compares the heat distribution in the material for the two approaches mentioned.

4.9 Discussion

The damage threshold of the B_4C/Si-sub at a grazing angle of 9 mrad was experimentally determined to be 0.34 µJ/µm^2 for single-shot damage. Additionally, we extracted an electron collision length of $d_e = 8.6$ nm.

As discussed in Section 4.8.1, the results are presented in Fig. 4.38, which compares the absorbed energy fraction as a function of depth between FLUKA sim-

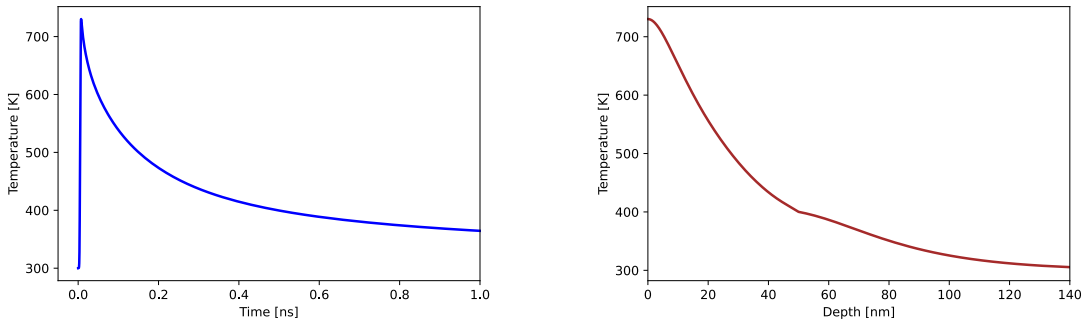

(a) Temperature versus time.

(b) Temperature versus depth.

Figure 4.36: Temperature distribution with using AEF(z) derived from FLUKA simulation.

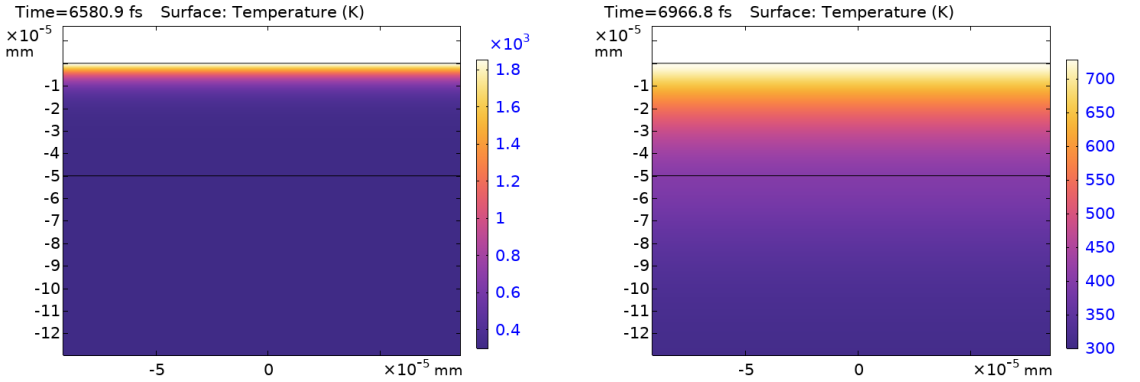

(a) Heat distribution without AEF consideration, using Eq. 3.28.

(b) Heat distribution with AEF consideration, using Eq. 4.16.

Figure 4.37: Comparison of heat distribution in the material with using result of FLUKA simulaiont.

ulations, and the energy deposition depth derived from experimental data. Fig. 4.39 illustrates a comparison of the dose between the FLUKA simulations and experimental results. Notably, the simulated energy deposition depth is approximately three times greater than the experimentally observed values. The electron collision length derived from the FLUKA simulation is about $d_e\,(FLUKA) = 24\,\text{nm}$, whereas the experimental data indicate an electron collision length of approximately $d_e\,(Exp) = 9\,\text{nm}$.

When we consider the COMSOL simulations discussed in Section 4.8.2, the comparison between FLUKA results and experimental data is illustrated in Fig. 4.40. Specifically, Fig. 4.40a shows the temperature versus time for simulations that incorporate the absorbed energy fraction (AEF) using Eq. 4.16, compared with the electron collision length derived experimentally (using Eq. 3.28). Additionally, Fig. 4.36b displays a comparison of these parameters along the depth of the material.

The discrepancies between simulation and experimental results may arise from several factors. In the experiments, the beam was not a perfect Gaussian profile,

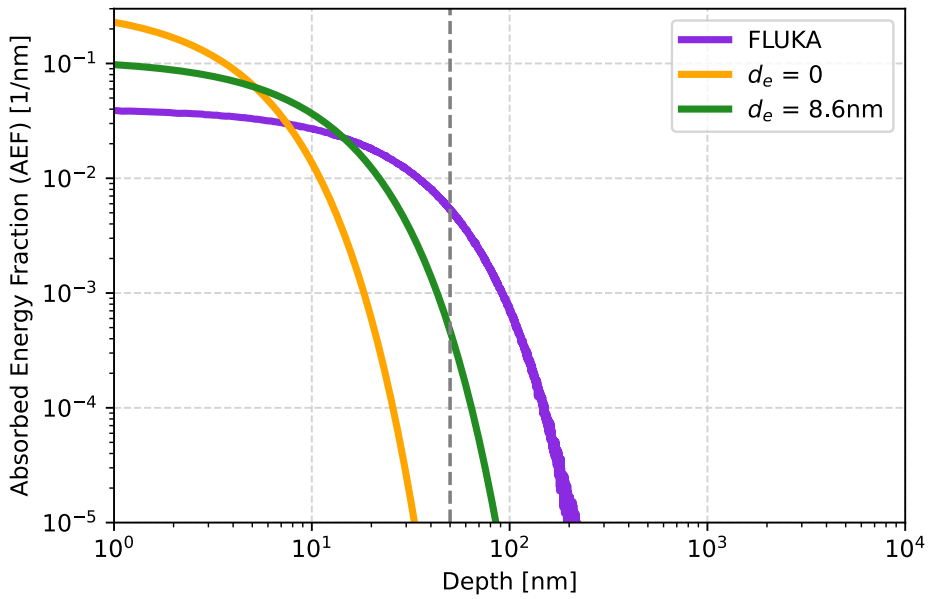

Figure 4.38: Comparison of the absorbed energy fraction (AEF) as a function of depth for different approaches. The purple line represents FLUKA simulations with an electron collision length of d_e(FLUKA)=24 nm. The orange curve corresponds to calculations using Eq. 4.15 without considering d_e, relying only on the penetration depth (Z_{pen}). The green curve represents calculations that include d_e(Exp)=8.6 nm, derived from experimental data. The dashed vertical gray line marks a depth of 50 nm, corresponding to the thickness of the B_4C layer.

whereas our simulations assumed an ideal Gaussian distribution. Additionally, in the COMSOL simulations, we employed the thermal properties of bulk B_4C; however, in the experiments, we were dealing with a thin layer of B_4C. The damage mechanisms in thin films can differ significantly from those in bulk materials or thicker films, as mechanical damage may occur prior to phase transitions [98]. Furthermore, in the assessment of multi-pulse damage, we considered discoloration as a form of damage, however, it is possible that the chemical structure of B_4C remained intact, and the material had not yet melted. More experiments in the future, along with additional data and more accurate results, will make it possible to compare simulations and experimental results in a more precise manner.

4.10 Conclusion

The primary objective of this chapter was to determine the damage threshold of B_4C on a silicon substrate and the electron collision length. These findings are crucial for identifying materials suitable for XFEL optics. Understanding the interactions between FEL beams and matter is essential for estimating potential damage

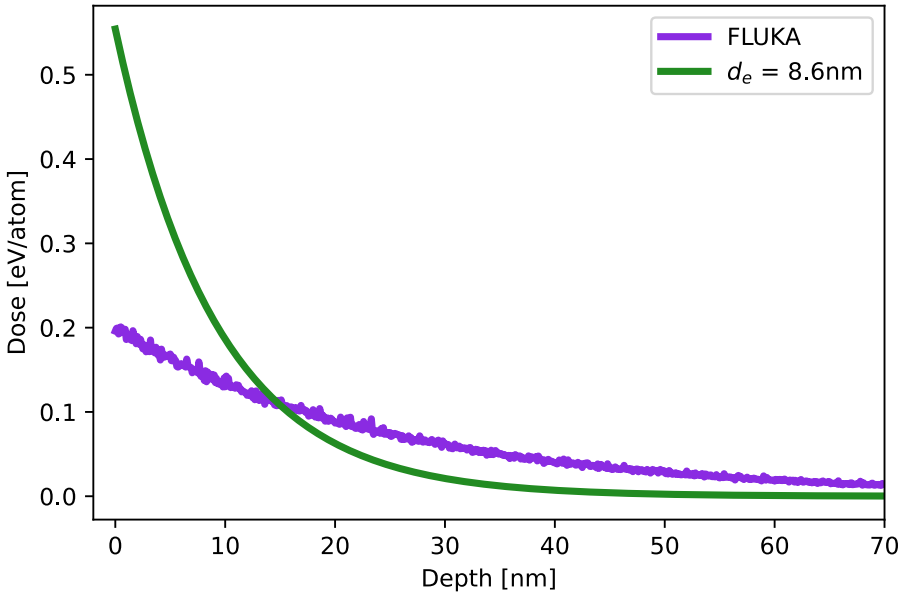

Figure 4.39: Comparison of the dose distribution as a function of depth between FLUKA simulations (purple curve) and data derived from experimental results (green curve).

to optics elements.

We conducted damage experiments on B_4C (50 nm)/Si-sub at grazing incidence angles of 9, 15, and 19 mrad at the European XFEL facility in the SQS beamline, using 1 keV photon energy. The measured damage fluences at these angles were found to be 0.34, 0.15, and 0.60 µJ/µm^2, respectively, with an effective area of 1589 µm^2. Notably, melting occurred only at the surface layer of the B_4C film, specifically within the top few nanometers, as the absorbed energy is mainly deposited within this coating. The threshold fluence was established at 0.16 µJ/µm^2 for silicon without coating at 9 mrad grazing angle. As anticipated, B_4C exhibits a damage threshold approximately twice that of silicon, demonstrating the advantages of utilizing B_4C as a coating on silicon substrates. These findings are instrumental for designing optics and instill greater confidence in employing B_4C as a coating material.

From our experimental data, we determined the electron collision length to be $d_e = 8.6$ nm. Our experiments demonstrated that a fraction of the incoming photon beam is absorbed through photoionization and Auger decay processes within the top layer of the surface. Photoelectrons are primarily ejected in a direction nearly normal to the mirror surface. The transport of energetic electrons increases the energy deposition depth, enhancing the damage resistance of X-ray mirrors, especially under grazing incidence conditions. At grazing angles, the X-ray penetration depth into the material is minimal, allowing photoelectrons to effectively distribute the dose to

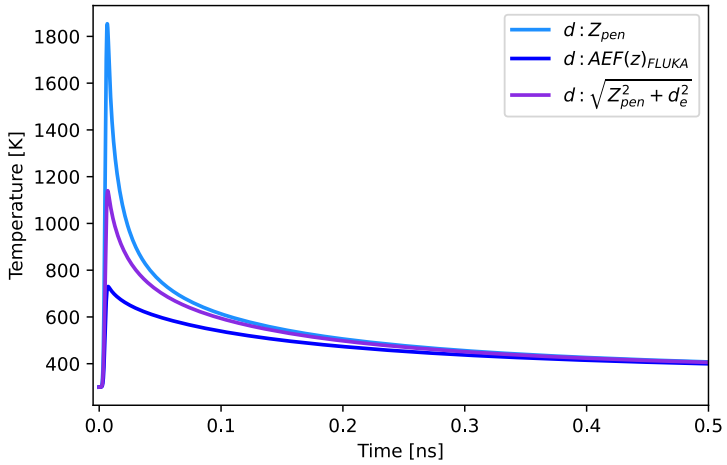

(a) Temperature versus time.

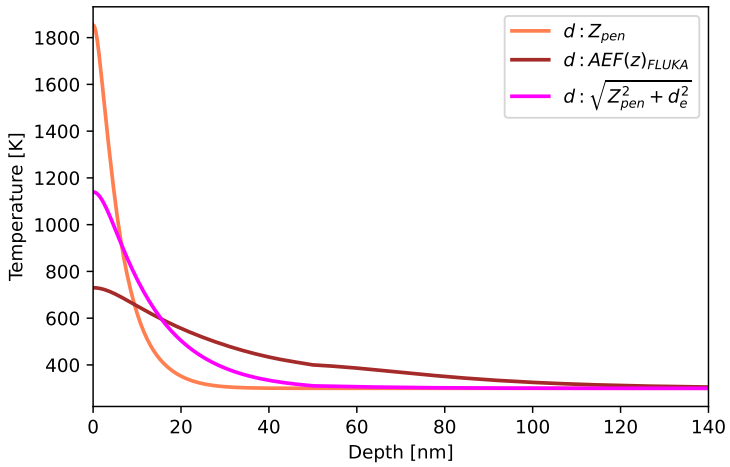

(b) Temperature versus depth.

Figure 4.40: Comparison of temperature profiles of COMSOL simulations between FLUKA and experimental data.

deeper layers and reduce localized damage.

Furthermore, our multi-pulse experiments, conducted at a repetition rate of 1.14 MHz, aimed to determine the damage threshold and revealed that the damage threshold decreases with an increasing number of pulses. The single-shot damage threshold for B_4C was approximately 170 times higher than that observed for 300 multi-pulse irradiation (0.34 µJ/µm^2 compared to 0.002 µJ/µm^2).

In this study, we proposed a simple model based on Monte Carlo simulations to evaluate the absorbed energy fraction, taking into account all electron-matter interactions, such as Auger decay and photoionization. We also utilized finite element analysis (FEA) through COMSOL simulations to assess the temperature increase over multi-pulse irradiation, with a photon energy of 1 keV. The simulation results indicate that the transport of photoelectrons may lower the dose by spreading it to

deeper layers of the material, significantly reducing damage at grazing angles below the critical angle.

Future experiments, along with additional data and more accurate results—particularly with improved Gaussian beam shapes—will allow for a better comparison between simulations and experimental outcomes.

For practical applications using ODL mirrors with B_4C coatings at SASE3, the beam fluence on the ODL corresponding to a beam size of $\sigma = 28.8\,\mu m$ and a pulse energy of $E_{pulse} = 100\,\mu J$ at 1 keV is approximately $F = 0.02\,\mu J/\mu m^2$, which is below the established threshold level. Fig. 4.41 shows the absorbed dose as a function of the photon energy (discussed in the previous chapter). The colored faded lines represent absorbed dose for E=500, 1000 and 2000 µJ, while the absorbed dose with considering $d_e = 8.6\,nm$ is indicated by solid points for 1 keV.

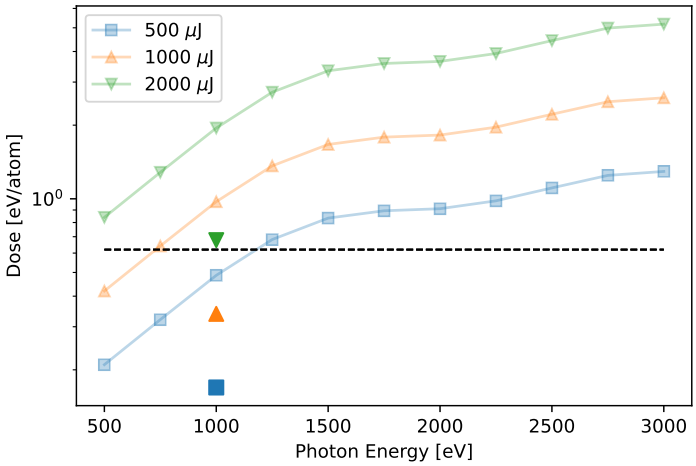

Figure 4.41: Absorbed dose as a function of photon energy for the ODL. The faded lines represent the absorbed dose calculated without considering d_e, while the solid points include the experimentally determined d_e for 1 keV. The figure highlights that incorporating d_e in damage threshold calculations indicates that for certain pulse energies, such as 1 mJ, it may not be necessary to open upstream undulators to prevent damage to the ODL.

These insights not only advance our understanding of the damage mechanisms in optical materials but also pave the way for improved design and utilization of optics in high-intensity X-ray applications.

CHAPTER 5 Overview, Implementation, Future Outlook

5.1 Overview

The two-color X-ray pump X-ray probe experiment is one of the most significant ultrafast experiments conducted at the European XFEL. The specific configuration of the SASE3 undulator allows for the generation of two different X-ray wavelengths. However, users of the setup currently face limitations in achieving zero or negative temporal delays between these wavelengths. This thesis addresses this challenge by employing an Optical Delay Line (ODL), consisting of four Silicon mirrors coated with 50 nm B_4C, capable of generating time delays ranging from negative 130 femtoseconds to a few positive picoseconds. In this study, we investigate the performance of ODL from both mechanical and optical perspectives.

Mechanically, the ODL provides sufficient movement to align the mirrors during the commissioning period, and optically, it exhibits excellent reflectivity within the photon energy range of 250-3000 eV, relevant to the operation of the SQS instrument. Detailed surface quality measurements indicate that the mirrors maintain a high level of quality, ensuring not degradation of the beam.

A critical concern regarding the ODL mirrors is their durability under higher fluences and photon energies. This thesis utilizes COMSOL simulations to assess the energy ranges in which the mirrors can safely operate. Given the significance of this issue—since damage to the mirrors could result in substantial time and cost implications—we performed a damage experiment at 1 keV.

The damage experiment demonstrated a threshold fluence of $0.34\,\mu J/\mu m^2$ for B_4C/Si at a grazing angle of 9 mrad. Notably, the B_4C/Si structure has a threshold fluence twice that of uncoated Si, underscoring the advantages of using B_4C coating. The experiment further confirmed that energy deposition within the material could be influenced by phenomena such as Auger decay and photoionization, resulting in an energy deposition depth of approximately 9 nm within the B_4C coating layer. For a deeper understanding of this process, we performed Monte Carlo simulations

using FLUKA and finite element analysis (FEA) simulations with COMSOL. Additionally, these simulations can provide better estimates of damage thresholds for other parameters, such as different photon energies.

5.2 Experimental Insights

An example of utilizing the pump-probe technique at SQS can be seen in a recent experiment conducted at the European XFEL under proposal number 3456 in February 2023 by Principal Investigator Fernando Martin, titled "Few-Femtosecond-Resolved Two-Color Pump-Probe Measurements of Hydrogen Migration and Roaming in Small Alcohols." This experiment aimed to explore the crucial role of hydrogen migration and roaming in various biochemical and photochemical processes.

By employing time-resolved electron diffraction imaging, utilizing molecular photoelectrons as probes, researchers aimed to trace hydrogen migration processes in ethanol and propanol molecules in real-time. The rapid motion of one or more hydrogen atoms, accompanied by chemical bond rearrangements, occurs on the femtosecond timescale. Reported timescales for such nuclear dynamics range from a few femtoseconds to several hundred femtoseconds, achievable using ultrashort FEL pulses [133].

During hydrogen migration, certain parts of a molecule can separate and interact weakly with other parts—a phenomenon known as roaming. This roaming fragment may further extract other atoms from the remaining molecular structure.

However, to directly image the dynamics generated by an ultrashort pulse, a second ultrashort probe pulse is essential to capture the molecular structure at different delay times. This experiment focused on measuring hydrogen movement in different alcohols (e.g., ethanol, propanol, and isopropanol) during ionization.

The researchers aimed to identify both single and double hydrogen movements and examine how these processes compete. The use of the European XFEL was critical, as it provides the unique combination of high energy and short pulse duration necessary for effective study of these rapid processes.

In this pump-probe experiment, the photon energies used were 555 eV and 660 eV (pump and probe, respectively), with pulse durations of approximately 10 fs and pulse energies around 100 µJ. The delay range extended to 150 fs. The spot size was around a few micrometers, with 50 pulses per train and a pulse train length of 400 µs, resulting in a repetition rate of 0.125 MHz.

If the ODL were to be utilized in this context with the pulse energy on the mirror approximately 100 µJ and as illustrated in Fig. 3.45c and Fig. 5.1, this energy would be well below the damage threshold, indicating that the ODL is safe in this scenario. The fluence on the beam is calculated as $F = \frac{100}{2 \cdot \pi \cdot 51^2} = 0.006 \mu J/\mu m^2$, with a time

interval of 8 µs between pulses, allowing sufficient cooling time before the subsequent pulse arrives.

In another experiment conducted under proposal number 5731, titled "Lifetime Determination of Key Astrophysical Transitions in Fe XVII Using the Two-color X-ray Pump-probe Technique," led by Principal Investigator Thomas Baumann and conducted in March of 2024, The researchers aimed to investigate ultra-short lifetimes of highly charged ions (HCIs) to enhance astrophysical diagnostics and validate atomic physics models.

In nature, most baryonic matter[1] exists in an ionized state. In massive galaxy clusters, this matter primarily takes the form of hot gas (20–100 million Kelvin) bound by a dark matter halo. Galaxies within these clusters account for only about 10% of the baryonic mass, but their interactions drive critical astrophysical phenomena, observable through X-ray emissions.

These X-ray emissions, originating from HCIs, provide essential data on the temperature, density, chemical composition, and opacity of the gas. A key diagnostic technique involves comparing the strengths of two strong emission lines from He-like and Ne-like states. To interpret these spectra accurately, precise measurements of oscillator strengths, collision strengths, and excited-state lifetimes are crucial [134–136].

Recent studies have attempted to resolve longstanding differences between measured and predicted intensity ratios of specific transitions. Despite advances using ultrahigh-resolution monochromators, uncertainties remain due to technical limitations. Addressing these challenges requires new, more accurate methods for measuring lifetimes and natural linewidths of HCIs.

The proposed experiment employed the two-color mode of the SASE3 undulator at the European XFEL. This mode enables time-resolved measurements of femtosecond (fs) dynamics in a pump-probe setup. Target ions are prepared in controlled charge states using a compact Electron Beam Ion Trap (EBIT), recently operational at the SQS instrument. These ions are then exposed to soft X-ray FEL radiation.

In this method, the first X-ray pulse (pump pulse) excites the ion to a specific energy state. The second pulse (probe pulse), tuned to a lower photon energy, further ionizes the excited ion. At long delays between the two colors, the excited state radiatively decays to the ground state. By varying the time delay between the two pulses and monitoring fluorescence emission and charge-state distributions, the excited-state lifetime can be determined. This time-domain technique offers excellent statistical precision, precise control over charge states and excitation pathways,

[1] A baryon refers to a heavy subatomic particle made up of three quarks, such as protons and neutrons. Astronomers use the term "baryonic matter" broadly to encompass all normal atomic matter, disregarding the negligible mass contribution of electrons.

and significantly reduced systematic uncertainties. Unlike traditional methods, this approach directly measures femtosecond lifetimes without relying on complex line profile modeling.

At this moment, no other facility can enable such an experiment. The European XFEL is uniquely suited for this experiment due to its high pulse energies, short pulse durations, flexible photon energy tunability, and MHz repetition rate.

For this experiment, the pump source parameters included a photon energy of 822 eV, a pulse duration of 25 fs, and a pulse energy of 400 µJ, with a spot size of a few micormeters, 200 pulses per train, and a pulse train length of 200 µs, resulting in a repetition rate of 1 MHz. The probe source exhibited similar characteristics, with a photon energy of 855 eV.

If the ODL is incorporated into this experiment with a positive delay, meaning the pump is generated by U1, the fluence arriving at the ODL would be approximately $F = \frac{400}{2 \cdot \pi \cdot 36^2} = 0.05 \mu J/\mu m^2$, which it is again below the damage threshold of the mirror in single-pulse condition.

In any case, if higher pulse energy or photon energy is required, it would be necessary to open some undulators upstream of the ODL. Fig. 5.1 indicates how many undulators should be opened upstream of the ODL to prevent damage on the mirror. In this figure, the electron collision length is not considered. Based on experimental results at 1 keV, with the electron collision length considered, the damage threshold is approximately three times higher.

5.3 Future Outlook

The optical components of the ODL are ready, with two mirrors coated and the remaining mirrors planned for coating in the next few months. The mechanical parts are currently being manufactured by FMB-Berlin and are expected to be completed by early 2025. During a planned six-month shutdown of the European XFEL in the second half of 2025, we will install the ODL in the tunnel alongside the magnetic chicanes. Following installation, mirror alignment will be performed, and the system will be prepared for user access.

It would be beneficial to develop a feature that alerts users about the safe operational limits of the ODL, ensuring they do not exceed the threshold energy and thereby prevent damage to the mirrors.

For improved comparison between experimental data and simulations, conducting another experiment with a better Gaussian beam and yielding more precise results would be advantageous. Our findings indicate that the electron collision length increases at higher photon energies, suggesting that experiments at 2 or 3 keV would yield more definitive insights into damage thresholds. Furthermore, multi-pulse

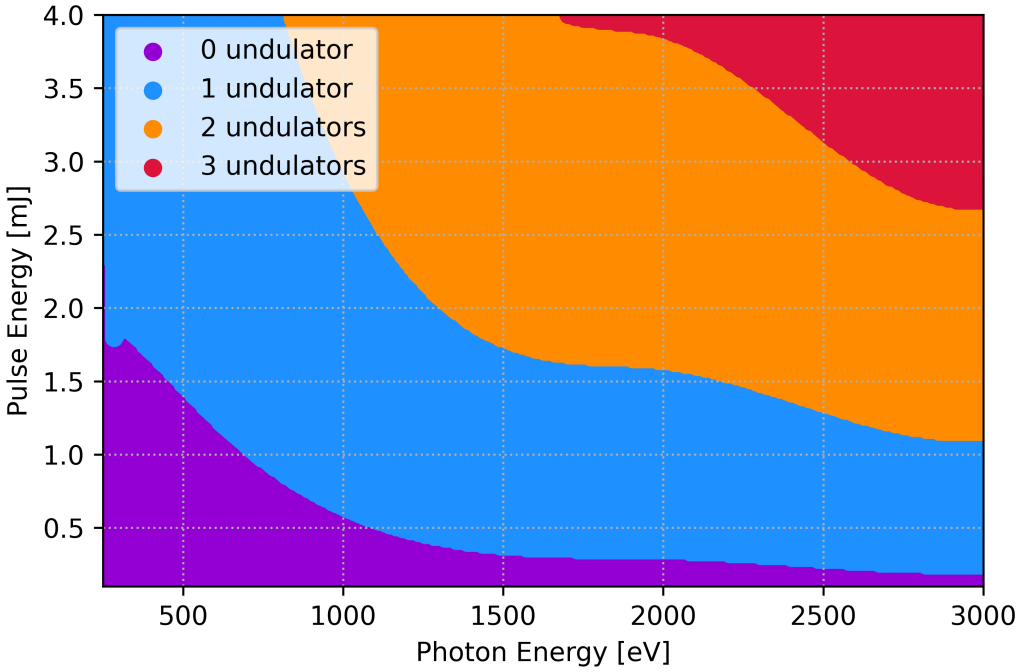

Figure 5.1: Number of undulators to open upstream of the ODL to avoid damage. The electron collision length is not considered. For photon energy at 1 keV, the damage threshold increases approximately three times when considering electron collision length.

damage experiments would be beneficial in gathering more comprehensive data.

List of Abbreviations

AEF	Absorbed Energy Fraction
CVD	Chemical Vapour Deposition
DESY	Deutsches Elektronen SYnchrotron
EuXFEL	European X-ray Free Electron Laser
EDD	Energy Deposition Distribution
FEA	Finite Element Analysis
FEL	Free Electron Laser
FEM	Finite Element Method
FWHM	Full Width at Half Maximum
HZG	Helmholtz-Zentrum Geesthacht
KB	Kirkpatrick–Baez
MC	Magnetic Chicane
ME	Mechanical Engineering
OASYS	OrAnge SYnchrotron Suite
ODL	Optical Delay Line
RMS	Root Mean Squared
SASE	Self Amplified Spontaneous Emission
SEC	Sample Environment and Characterization
SPF	Simulation of Photon Fields
SQS	Small Quantum Systems
SRW	Synchrotron Radiation Workshop
STD	Standard Deviation
WLI	White Light Interferometry
XFEL	X-ray Free Electron Laser
XGM	X-ray Gas Monitor
XPD	X-ray Photon Diagnostics
XRO	X-Ray Optics
YAG	Yttrium Aluminium Garnet

CHAPTER A | Appendix: Optical Delay Line

A.1 Thermal-Dependent Properties of Si and B_4C

It is necessary to consider the temperature-dependent properties of the material when studying the heat transfer on the mirror. Fig. A.1 displays the thermal properties of silicon [137], while Fig. A.2 illustrates the thermal properties of B_4C. The temperature-dependent parameters of thick B_4C were measured at the Fraunhofer Institute on our behalf.

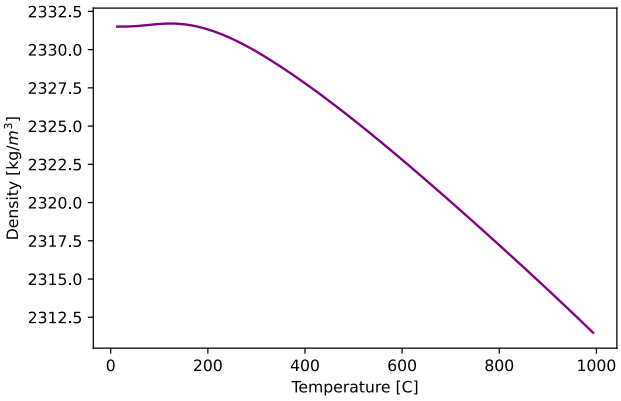

(a) Density.

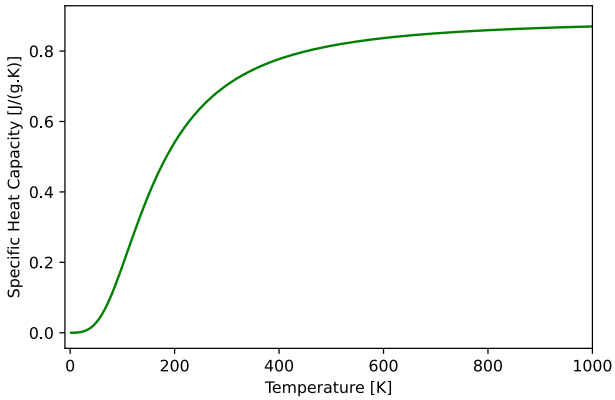

(b) Specific heat capacity.

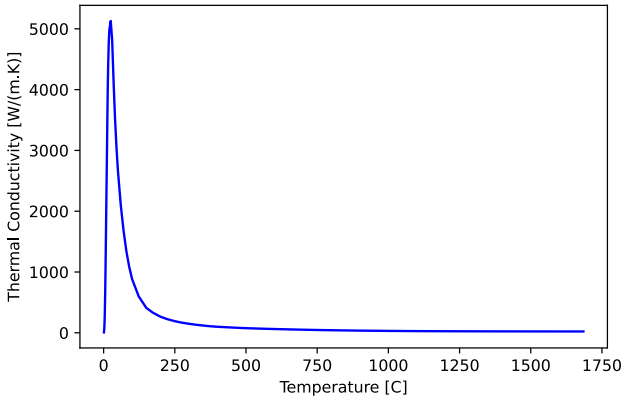

(c) Conductivity.

Figure A.1: Temperature-dependent properties of silicon.

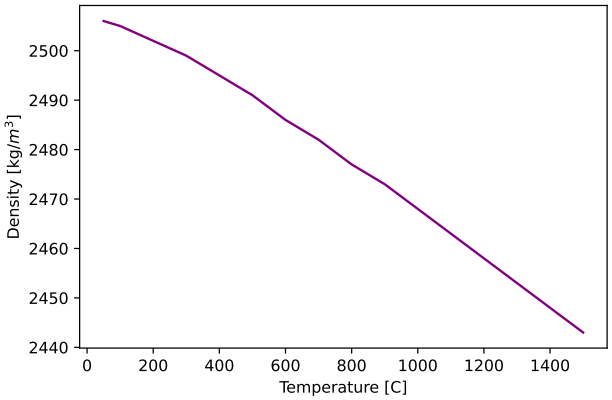

(a) Dencity.

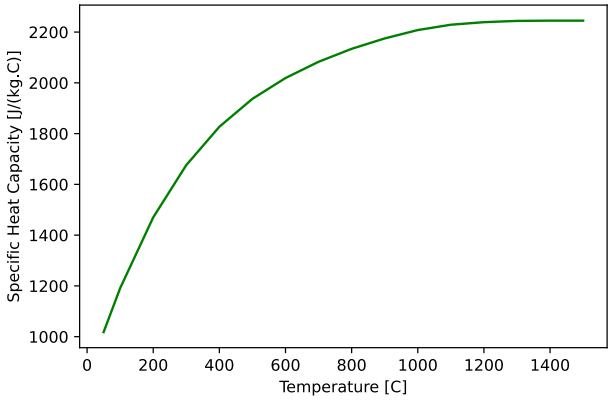

(b) Specific heat capacity.

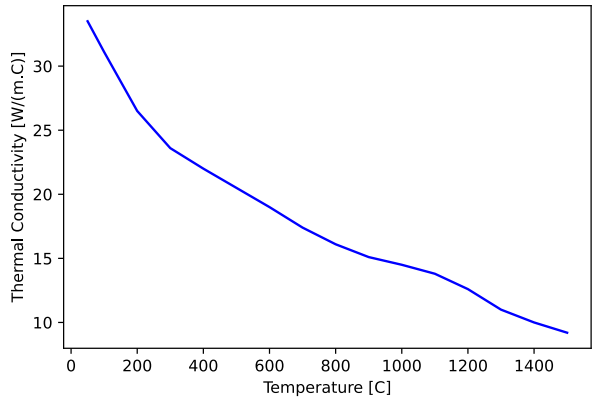

(c) Conductivity.

Figure A.2: Temperature-dependent properties of B_4C.

A.2 Fizeau Interferometer

A Fizeau interferometer is a laser interferometer configuration commonly used for measuring the surface shape and flatness of optical surfaces. It was invented by Armand Fizeau, a French physicist, in the 19th century.

This interferometer relies on the principle of interference, where light waves superimpose to produce a pattern of fringes that can reveal detailed surface information. Fizeau interferometry is a relative measurement technique that compares a test surface to a high-quality reference surface. The system typically consists of a laser source, a beam splitter, a reference mirror, and a camera, as depicted in Fig. A.3 [70, 138, 139].

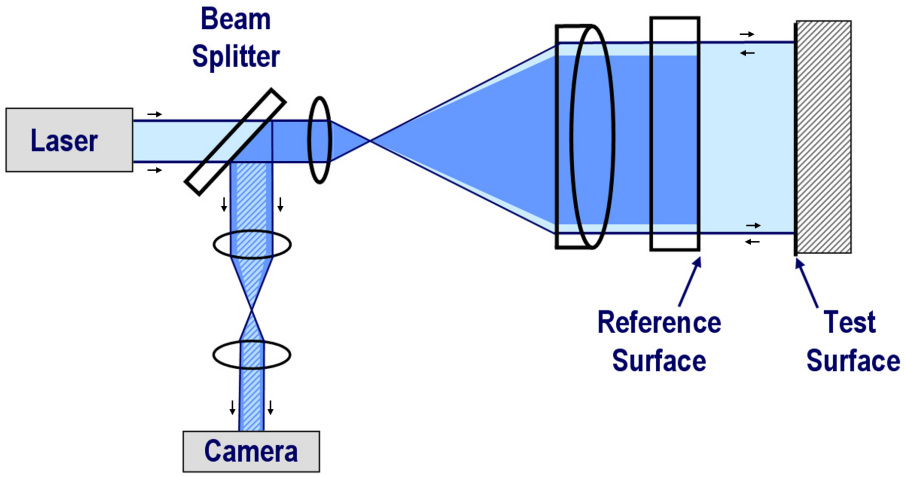

Figure A.3: Schematic arrangement of Fizeau interferometer [140].

The setup relies on interference between the test surface and a nearby reference surface. The reference surface, usually the right surface of an optical flat, possesses extremely high flatness and surface quality. The process involves a monochromatic light beam, such as from a laser, directed through a pinhole and a converging lens to produce parallel rays. Then some of the incident light is transmitted through the reference mirror while a portion is reflected by it. This part of the beam is reflected by a high-quality reference surface, while the transmitted beam is reflected by the surface under examination. Both beams return to the beam splitter, recombine, and interfere due to differences in optical path lengths, creating an interference pattern recorded by a sensor or imaging device.

The interference pattern consists of bright and dark fringes, corresponding to constructive and destructive interference, respectively. During the measurement process, a piezo is used to vary the optical path, making these fringes moving across the field of view. By combining several frames of acquired fringe patterns, one can

measure the heights of all points on the test surface, or quantify the change in wavefront caused by the beam passing through the optic. This pattern reveals critical information about the surface under test, including surface height and flatness.

We utilized a 12-inch large aperture Fizeau Zygo interferometer to measure the surface quality of the ODL mirrors (Fig. A.4).

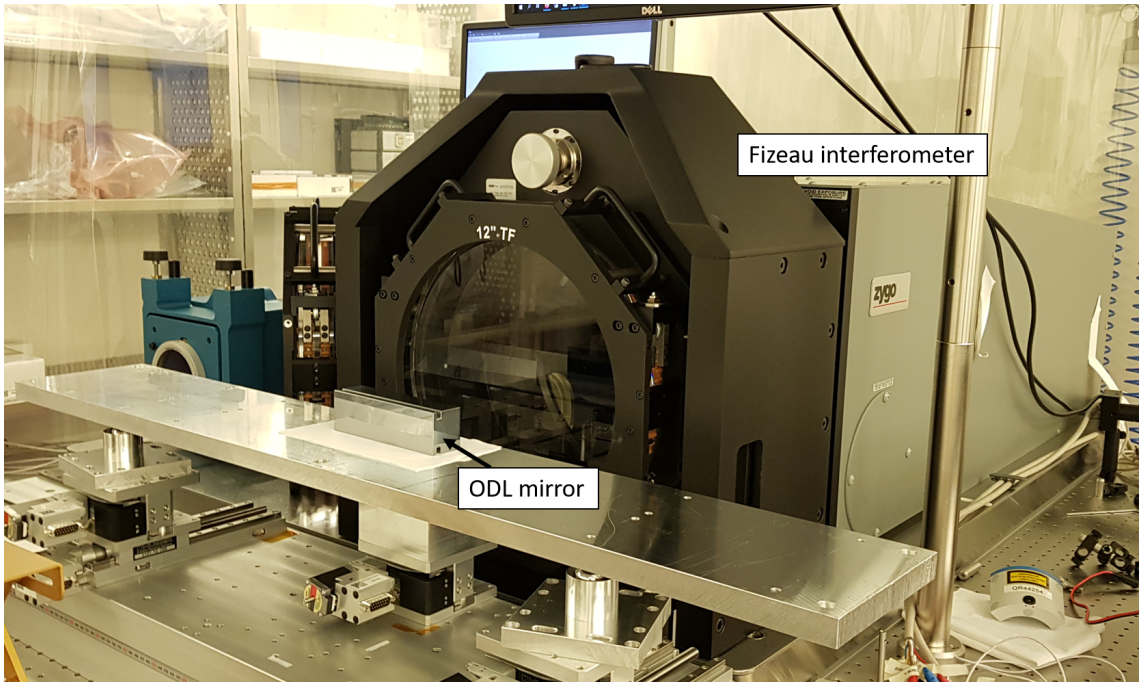

Figure A.4: Large aperture Fizeau Zygo interferometer used for mirror surface quality assessment at European XFEL.

A.3 White light interferometry (WLI)

Accurate surface characterization is essential in a wide range of scientific and industrial applications, such as ensuring the quality of optical components. High surface roughness on mirrors can significantly compromise beam quality. White Light Interferometry (WLI) is a powerful, non-contact optical technique that provides nanometer-scale precision in measuring surface roughness. This method analyzes surface profiles and detects variations with exceptional accuracy, making it ideal for assessing the quality of optical components.

Fig. A.5 shows the schematic setup of a White Light Interferometer device. A broadband light source, commonly referred to as "white light", is split into two paths: one directed toward a reference mirror with a fixed optical path length and the other toward the test sample. Variations in the sample surface height alter the optical path length of the reflected beam. The reflected beams from the reference and sample are then recombined, producing an interference pattern that is detected by a CCD sensor.

The interference arises from the phase difference between the two beams:

- **Constructive interference** occurs when the waves are in phase, amplifying the resulting signal.
- **Destructive interference** occurs when the waves are out of phase, canceling each other out.

This interference pattern encodes information about the surface height variations on the sample.

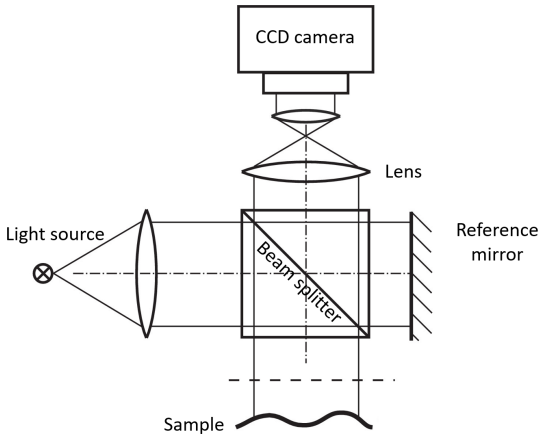

Figure A.5: The schematic setup of a White Light Interferometer typically includes: light source, beam splitter, reference mirror, lens and collimator, CCD image sensor [141].

The system is designed so that the optical path lengths of the reference and sample are identical at the CCD sensor when the sample surface is flat. Any asperities on the test surface cause path length differences, forming an interference pattern. These patterns are translated into peaks and troughs corresponding to the surface heights. The lens is moved by a piezo to adjust the phase condition, and the corresponding phase and intensity are acquired and later converted into a surface profile [142–145].

WLI can be equipped with various microscope lenses to achieve high magnification. A commonly used objective lens in such setups is the Mirau objective, which integrates a miniaturized reference mirror and beam splitter into the objective lens. This configuration minimizes shadowing effects and allows for precise measurement of fine surface details, even at high magnifications. For our roughness measurements, we used the Zygo White Light Interferometer NexView (Fig. A.6).

Figure A.6: Zygo White Light Interferometer NexView

A.4 Fizeau Measurments

The surface quality of the ODL mirrors is presented here. Measurements were performed using the 12" large-aperture Fizeau interferometer at the European XFEL, with a digital mask (7 mm wide) in the software set slightly larger than the clear aperture. The edge of the mirror is shown on the minimum of Y-axis. The large heights observed at the edge are not real; they are noise caused by the sharp edge of the mirror.

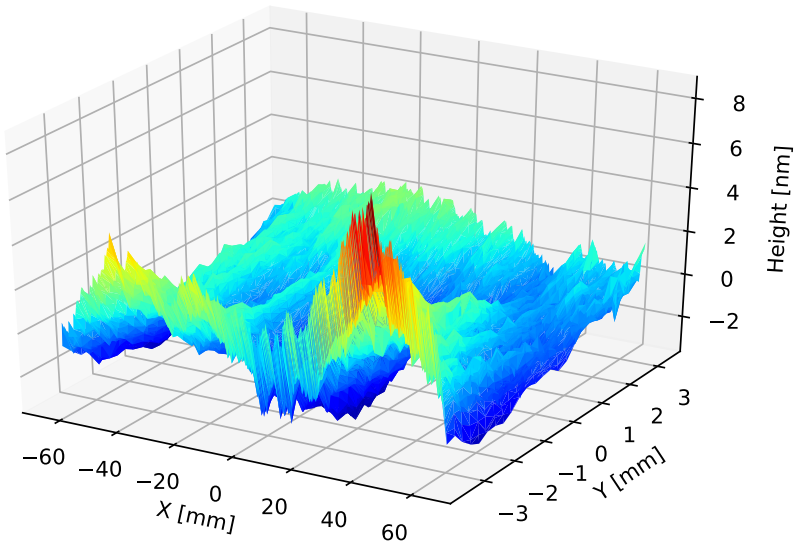

(a) 3D map.

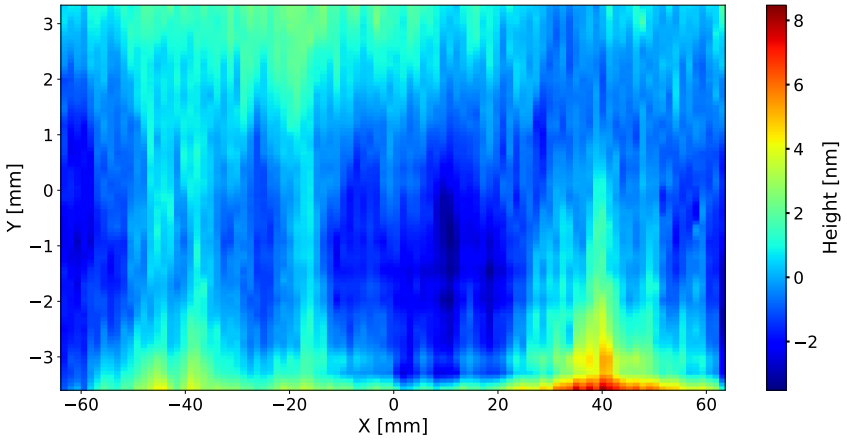

(b) 2D map (P-V: 11.9nm; rms:1.39nm).

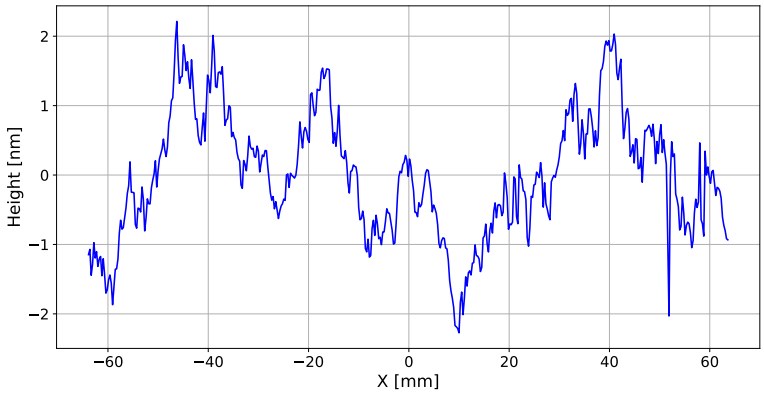

(c) Central profile (P-V: 4.5nm; rms:0.89nm).

Figure A.7: Fizeau measurement of mirror M1 before coating, with the best-fit tilt and parabola removed. The edge of the mirror is shown at the minimum of the Y-axis.

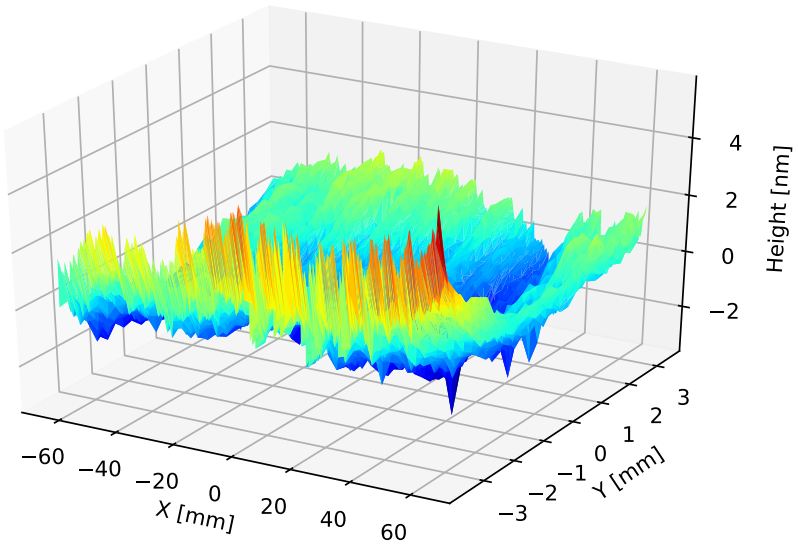

(a) 3D map.

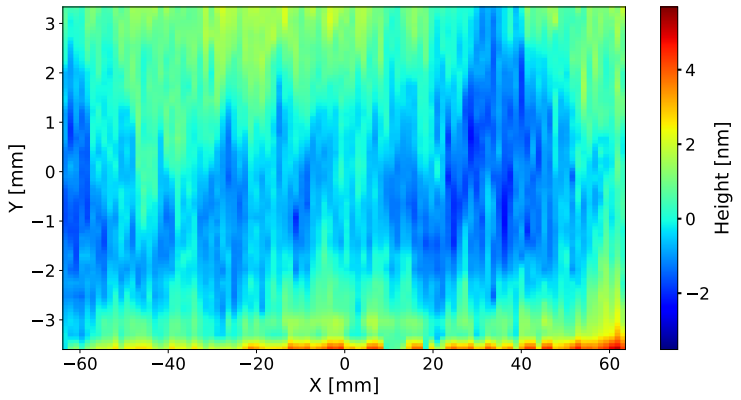

(b) 2D map (P-V: 9.2nm; rms:1.02nm).

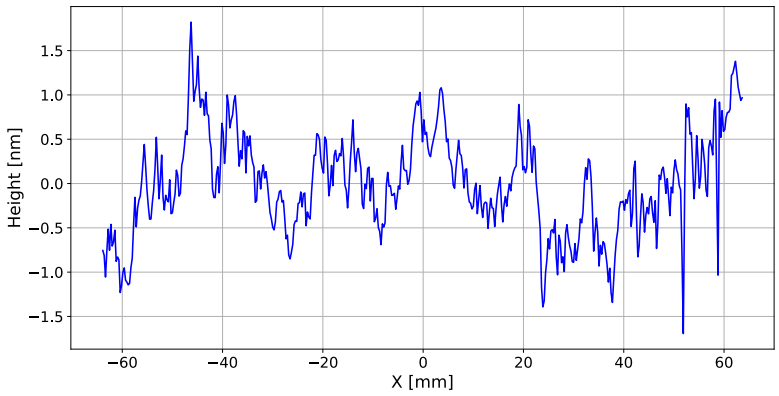

(c) Central profile (P-V: 3.5nm; rms:0.56nm).

Figure A.8: Fizeau measurement of mirror M2 before coating, with the best-fit tilt and parabola removed. The edge of the mirror is shown at the minimum of the Y-axis.

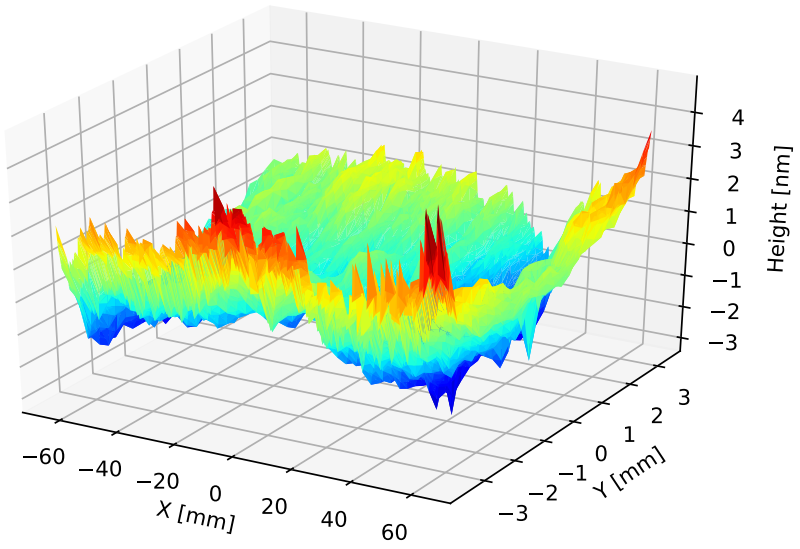

(a) 3D map.

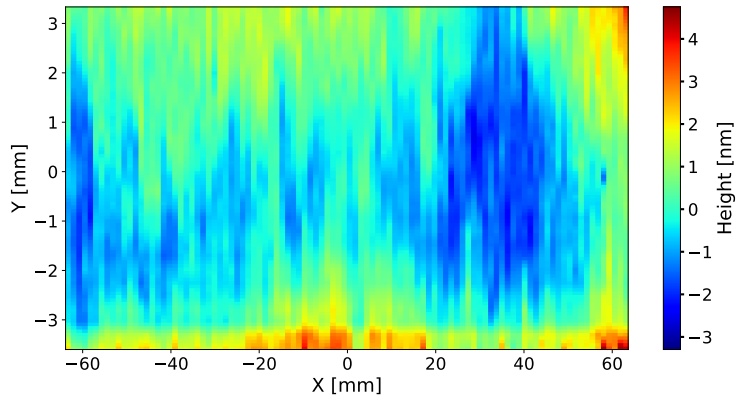

(b) 2D map (P-V: 8.1nm; rms:1.02nm).

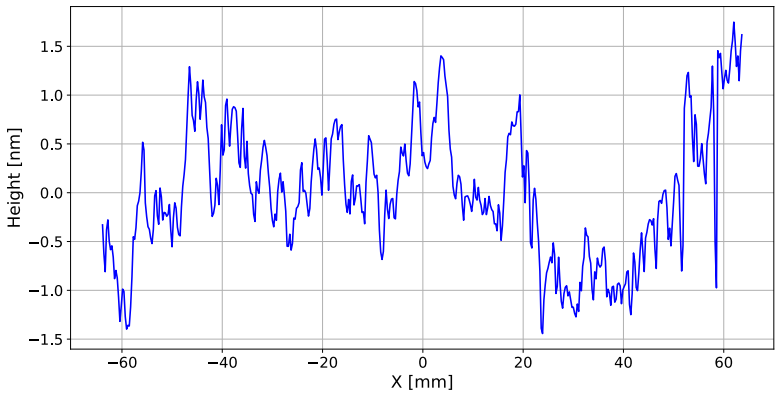

(c) Central profile (P-V: 3.2nm; rms:0.67nm).

Figure A.9: Fizeau measurement of mirror M3 before coating, with the best-fit tilt and parabola removed. The edge of the mirror is shown at the minimum of the Y-axis.

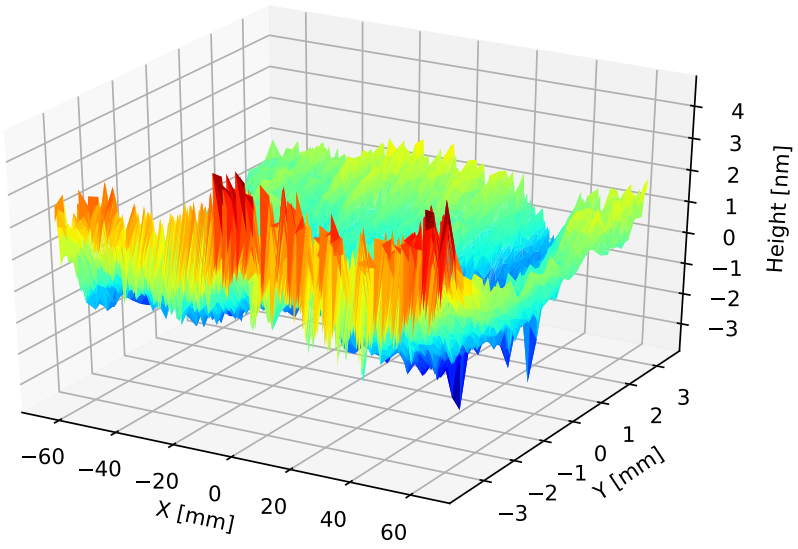

(a) 3D map.

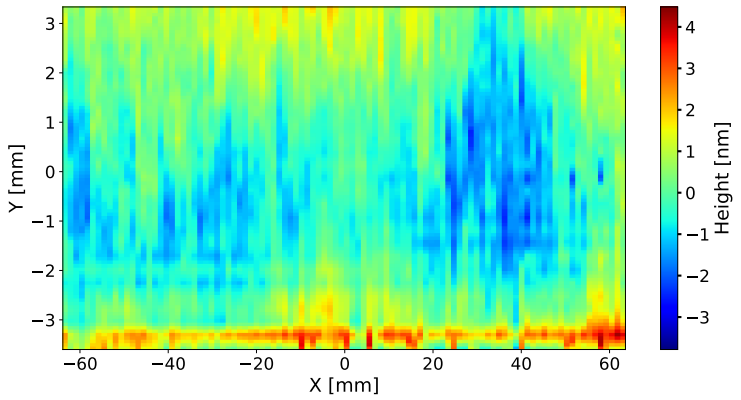

(b) 2D map (P-V: 8.3nm; rms:0.99nm).

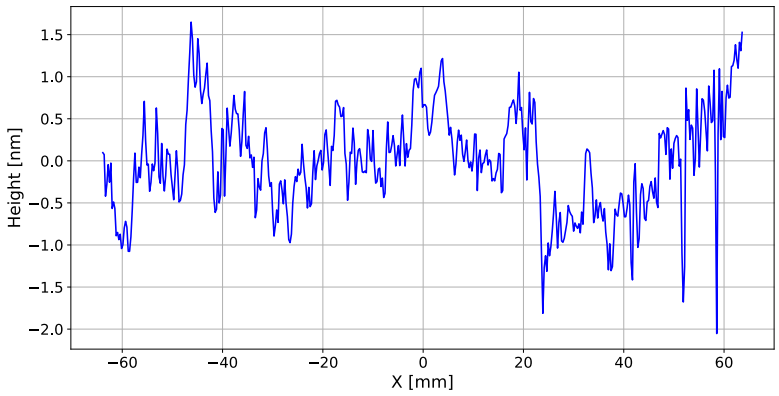

(c) Central profile (P-V: 3.7nm; rms:0.60nm).

Figure A.10: Fizeau measurement of mirror M4 before coating, with the best-fit tilt and parabola removed. The edge of the mirror is shown at the minimum of the Y-axis.

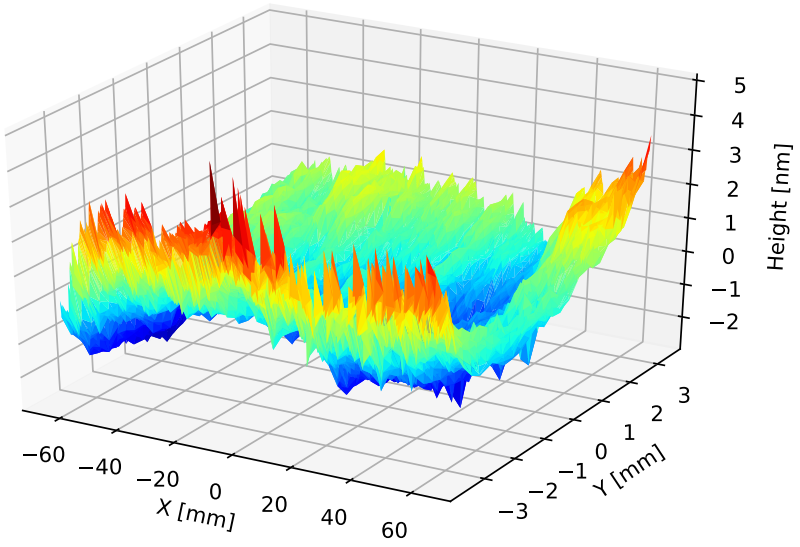

(a) 3D map.

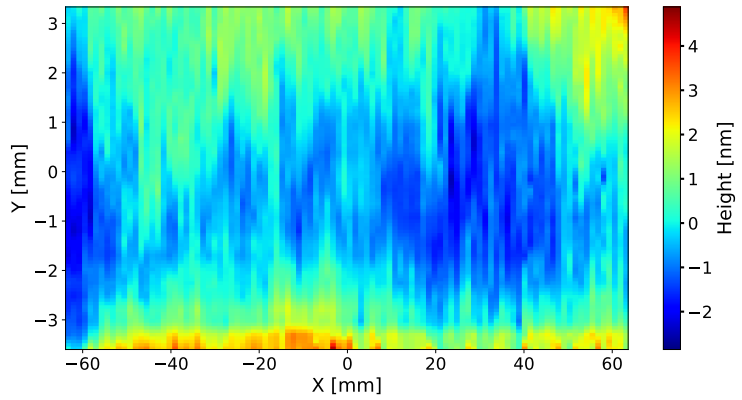

(b) 2D map (P-V: 7.7nm; rms:1.01nm).

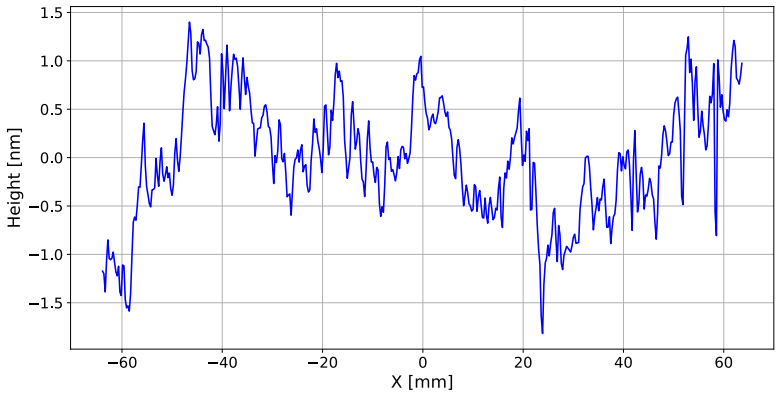

(c) Central profile (P-V: 3.2nm; rms:0.62nm).

Figure A.11: Fizeau measurement of mirror M5 before coating, with the best-fit tilt and parabola removed. The edge of the mirror is shown at the minimum of the Y-axis.

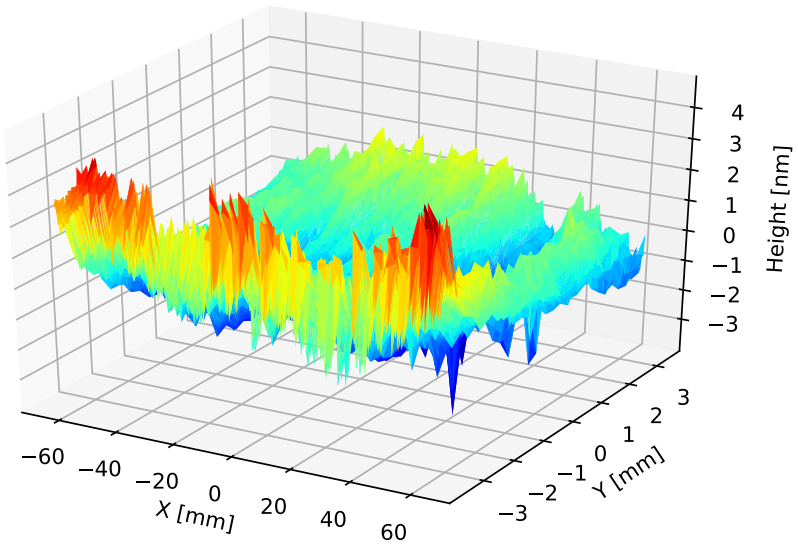

(a) 3D map.

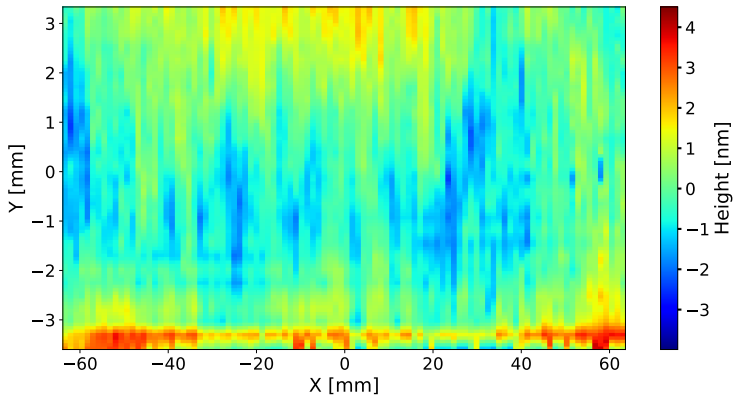

(b) 2D map (P-V: 8.5nm; rms:0.97nm).

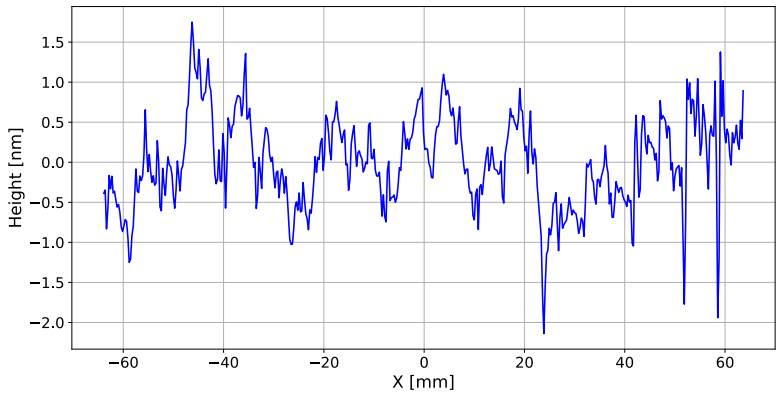

(c) Central profile (P-V: 3.9nm; rms:0.57nm).

Figure A.12: Fizeau measurement of mirror M6 before coating, with the best-fit tilt and parabola removed. The edge of the mirror is shown at the minimum of the Y-axis.

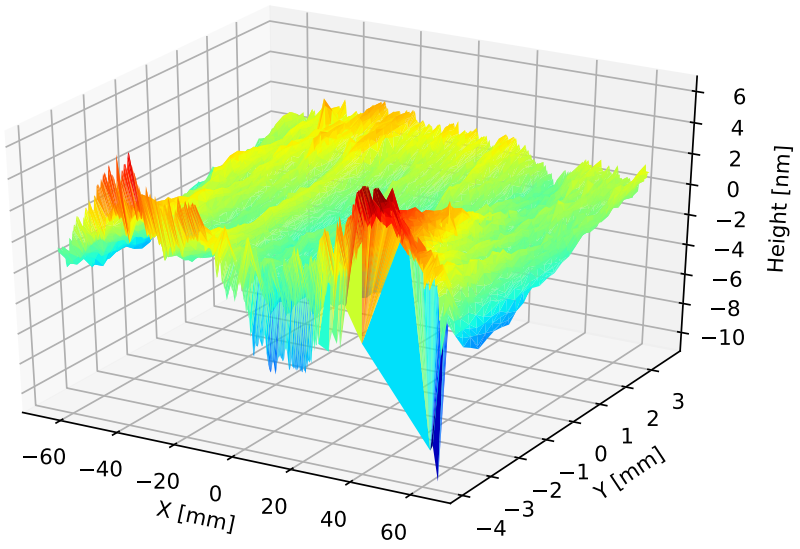

(a) 3D map.

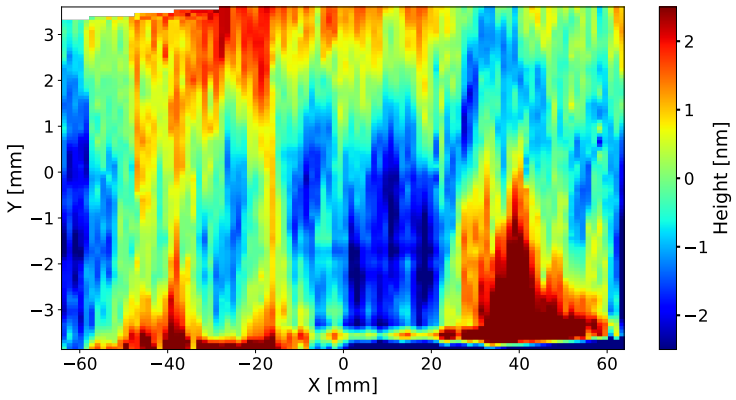

(b) 2D map (P-V: 17.5nm; rms:1.39nm).

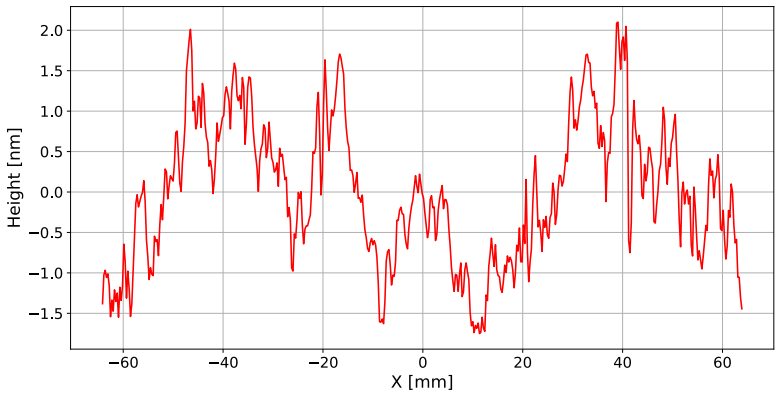

(c) Central profile (P-V: 4.5nm; rms:0.89nm).

Figure A.13: Fizeau measurement of mirror M1 after coating, with the best-fit tilt and parabola removed. The edge of the mirror is shown at the minimum of the Y-axis.

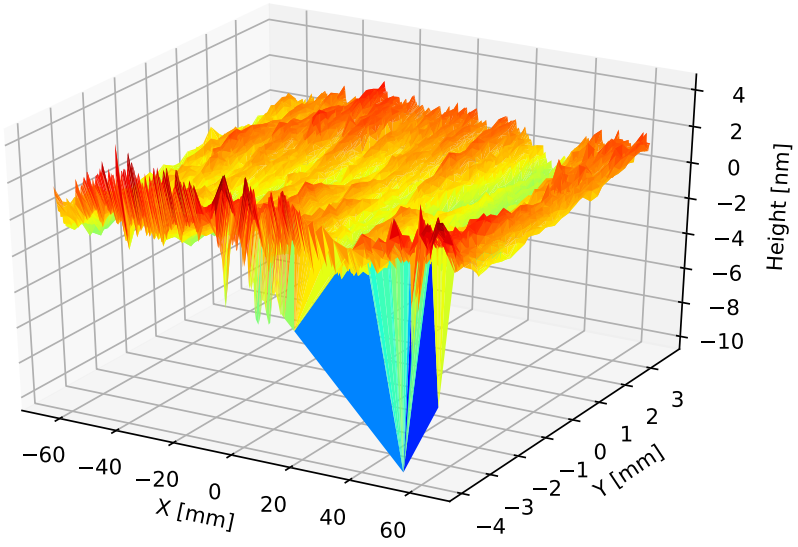

(a) 3D map.

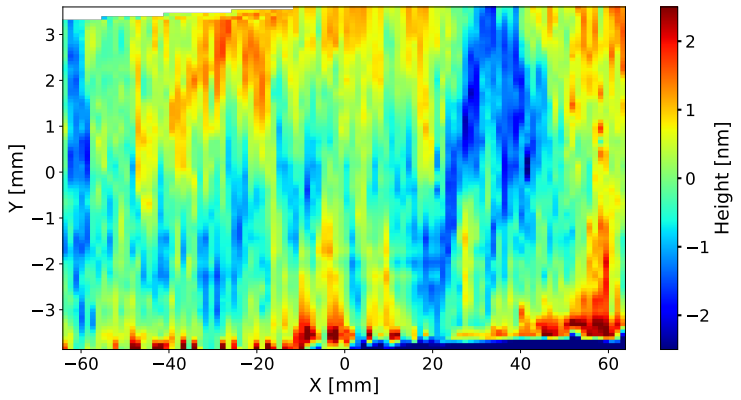

(b) 2D map (P-V: 15.0nm; rms:0.88nm).

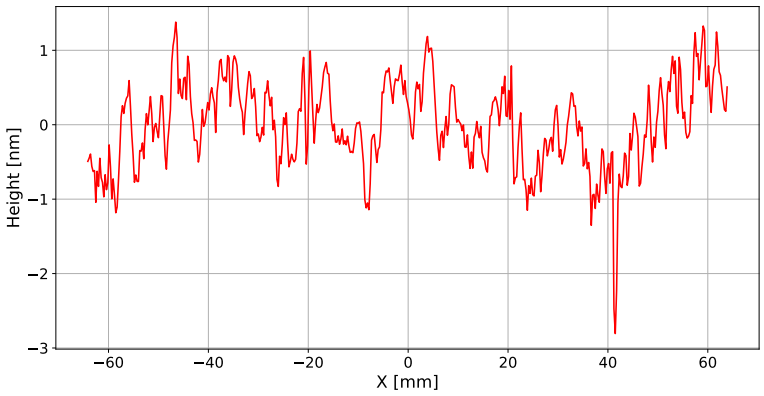

(c) Central profile (P-V: 3.2nm; rms:0.67nm).

Figure A.14: Fizeau measurement of mirror M3 after coating, with the best-fit tilt and parabola removed. The edge of the mirror is shown at the minimum of the Y-axis.

CHAPTER

B Appendix: Damage Test

B.1 X-Ray Gas Monitor

The X-Ray Gas Monitor (XGM) is an essential diagnostic tool at the European XFEL, designed for precise single-shot pulse energy measurements and average beam position monitoring, a critical need due to the intensity fluctuations caused by the self-amplified spontaneous emission (SASE) process. The primary purpose of XGMs is to provide accurate, non-destructive measurements of the FEL pulse intensity for each shot, supporting users in obtaining stable experimental conditions and reliable data.

The XGM chamber contains a target gas, typically neon (Ne), argon (Ar), or krypton (Kr), at a pressure of about 10^{-5} mbar, which is almost transparent to the FEL pulse. Transparency allows the FEL beam to continue unaltered toward the experimental hutches. When the FEL beam passes through the chamber, it ionizes the rare gas atoms, generating ions and electrons as reaction products. These ions and electrons are then separated and directed toward different sections of the detector by using an electric field. The field, created by two high voltages applied to the extraction electrodes, pulls the ions upward and the electrons downward to dedicated detection areas within the XGM (see Fig. B.1).

The ions are collected at the upper section of the XGM by a large Faraday cup electrode. The current signal from the electrode is recorded by an electrometer, but before reaching the electrometer, the signal is integrated in a custom circuit. This integration reduces potential errors in current measurement caused by the pulsed structure of the FEL signal. This measurement provides a direct correlation to the FEL bunch intensity, making it a reliable indicator of beam intensity.

In addition to the Faraday cup, an ion time-of-flight spectrometer is installed on the ion side. The ions can pass through a hole in the faraday cup electrode and enter a commercial ETP 14880 ion detection system with an electron multiplier. The resulting signal is then amplified and digitized to determine the charge-state distribution of ions produced in the interaction. This information is critical for cal-

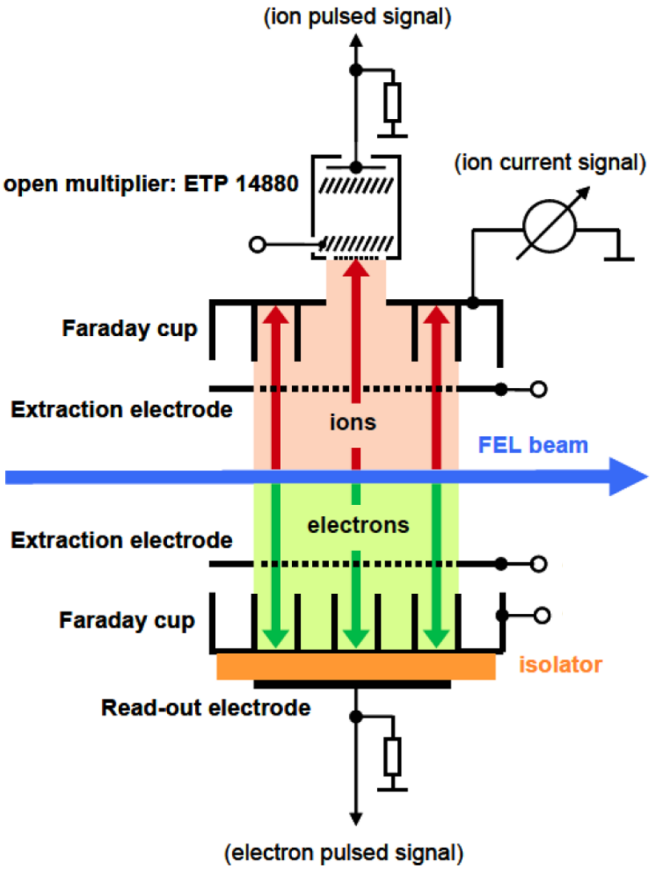

Figure B.1: Schematic diagram of the X-Ray Gas Monitor (XGM). The FEL beam ionizes a target gas, creating ions and electrons. The ions are directed upward to a Faraday cup, where their current signal is measured to determine pulse energy. Electrons are directed downward to another Faraday cup, where the signal is amplified and digitized for monitoring [111, 146].

culating a correction factor for FEL intensity measurements, enhancing the accuracy of pulse energy readings on the 4.5 MHz pulse time scale. The measured ion current is thus proportional to the total FEL beam energy, making it possible to accurately determine energy output.

At the bottom section of the XGM, electrons are collected by another Faraday cup, where the signal is capacitively coupled, amplified, and sent to a digitizer. Although this signal is not used directly for intensity calculations, it is essential for monitoring during commissioning or maintenance.

The XGM also includes a position intensity monitor. This system, using a HAMP (Huge Area Open Multiplier) detector, is configured to measure both the horizontal and vertical positions of the beam by passing the FEL pulse in between two split-electrode plates, allowing the pulse-resolved determination. This XGM provides accurate, high-resolution intensity monitoring while preserving beam integrity, which is indispensable for achieving reliable and reproducible experimental results [147,

148].

A variant of the XGM, known as the X-ray Gas Monitor Detector (XGMD), is installed in the SQS instrument at European XFEL. This detector provides sub-200 ns temporal resolution for online, pulse-resolved photon flux measurements across a broad photon energy range (250 eV to 12.4 keV), with an absolute uncertainty of less than 10% for intensity determination and a relative standard uncertainty for pulse-to-pulse intensity instabilities of 1% for more than 10^{10} photons per pulse. The XGMD is located upstream of the KB mirror system enabling precise monitoring of intensity delivered to the experiment station on a single-shot basis, after the beam has passed optical elements like off-set mirrors, apertures, and an optional soft X-ray monochromator [111, 146, 149].

B.2 Gas Attenuator

Gas attenuators are essential beamline components within XFEL facilities, where they provide a controlled reduction in X-ray beam intensity to protect sensitive downstream components and support various experimental requirements. Due to the extremely high peak intensity of FELs, unattenuated beams can cause significant damage to equipment such as mirrors. Therefore, gas attenuators allow for safe, flexible operations. This controlled modulation is crucial during mirror alignment and other setup processes, enabling users to gradually increase beam intensity without risk to the equipment. In various experiments, where intensity scanning is required, it allows researchers to vary the beam intensity without adjusting the accelerator or undulator, which is particularly advantageous for high-repetition-rate FELs like the European XFEL. In cases requiring fine-tuning, combining a gas attenuator with a solid attenuator provides enhanced control over beam attenuation [150, 151].

The gas attenuator functions by attenuating the FEL beam through controlled gas absorption. This functionality is achieved with a gas-filled tube, also known as a "gas absorption cell". The attenuation level within the gas attenuator depends on factors like the gas density, interaction length, and type of gas used. Commonly, Nitrogen or Argon is typically used as the filling gas, with pressure adjustments allowing precise control over the attenuation. This relationship between gas pressure and attenuation is described by a first-order approximation of the Beer-Lambert law (Fig. B.2):

$$I = I_0 e^{-\mu \rho d} \tag{B.1}$$

where I_0 is the initial beam intensity, I is the intensity after photoabsorption, μ represents the mass absorption coefficient (depending on the material and photon

energy), ρ is the material density (pressure- and temperature-dependent for gases), and d is the total effective attenuation path length. By adjusting gas pressure, the system controls the density within the gas cell, modulating the beam intensity accordingly [152, 153].

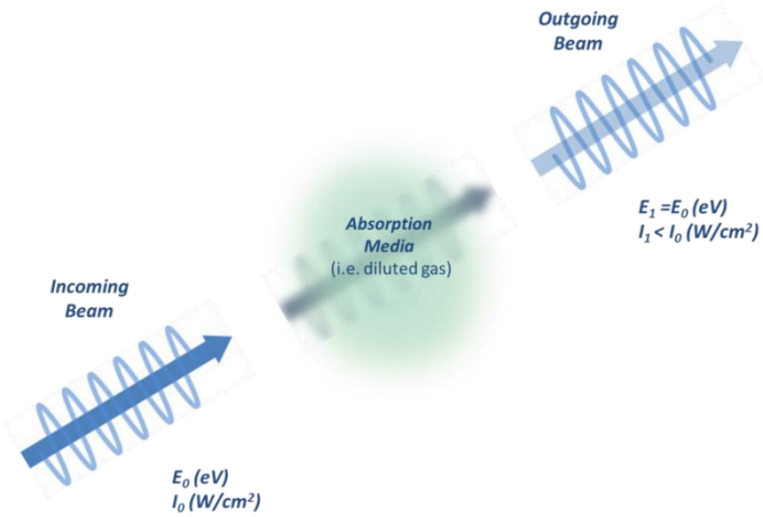

Figure B.2: Illustration of gas attenuator function, where an incoming X-ray beam is attenuated by passing through a gas-filled absorption medium [153].

The European XFEL operates at an ultra-high repetition rate of up to 4.5 MHz, which creates specific challenges for the gas attenuator. First, the attenuator must withstand high peak intensities, requiring a gas-based attenuation medium for soft X-rays. Additionally, it must dissipate the absorbed energy swiftly to reset between pulses. For instance, at 4.5 MHz, pulses arrive every 0.22 µs, so the gas volume must return to its initial state quickly to maintain consistent attenuation.

The XFEL gas attenuator is a windowless tube filled with nitrogen, with differential pumping sections on each end to maintain ultra-high vacuum conditions outside the attenuator. The nitrogen filling provides a controllable transmission range from 1.10^{-12}% to 100%, adjustable based on the photon wavelength, gas species, and pressure. The device also allows for precise pressure control, with the minimum controllable pressure during injection at 0.001 mbar and a maximum allowable pressure of 35 mbar [25, 152, 153].

B.3 Si, Single-Shot Damage Test at Grazing Angle 9 mrad, Observed Damage

Sample	**line No.**	**XGM** $[\mu J]$	**ATT** [%]	$\mathbf{E_{pulse}}[\mu J]$ **reached to sample**
Sample 1	1	4816.1	97.12	1571.6
	2	4550.6	97.13	1485.1
	3	4800.5	60.60	977.4
	4	4614.4	60.38	936.2
	5	4554.4	35.46	542.6
	6	4679.0	35.30	555.0
	7	4376.2	20.47	301.0
	8	5127.2	21.04	362.5
	31	5083.5	95.75	1635.5

Table B.1: Parameters for Si single-shot damage test at grazing angle 9 mrad.

B.4 B_4C, Single-Shot Damage Test at Grazing Angle 9 mrad, Observed Damage

Sample	**line No.**	**XGM** $[\mu J]$	**ATT** [%]	$\mathbf{E_{pulse}}[\mu J]$ **reached to sample**
Sample 2	42	4564.1	97.19	1490.4
	43	4401.9	69.15	1022.7
	44	4358.2	69.15	1012.6
Sample 3	32	4719.6	59.73	947.2
	42	4504.0	70.10	1060.8
	43	4549.3	70.12	1071.8
	44	4846.6	70.14	1142.2
	45	5290.4	70.17	1247.3
	46	4328.8	70.19	1020.9
	47	4691.0	70.18	1106.2
	48	4642.3	70.20	1095.0
	49	5066.0	70.20	1194.9
	50	4438.6	70.19	1046.8
	51	4573.7	80.00	1229.4
	52	4715.0	80.03	1267.9
	53	4441.2	80.11	1195.4
	54	5174.0	80.14	1393.2
	55	5466.6	80.17	1472.5
	56	4120.2	80.19	1110.1
	57	4396.5	80.20	1184.7
	58	4961.1	80.21	1337.0
	59	4656.1	80.24	1255.3
	60	4481.1	98.54	1483.7
	61	4916.2	98.62	1629.1
	62	5327.9	98.65	1766.0
	63	4526.7	98.70	1501.2
	64	5138.3	98.74	1704.7
	65	4848.1	98.75	1608.6
	66	4645.0	98.80	1542.0
	67	4915.9	98.80	1631.9
	68	5416.4	98.86	1799.2

Table B.2: Parameters for B_4C single-shot damage test at grazing angle 9 mrad.

B.5 B_4C, Single-Shot Damage Test at Grazing Angle 15 mrad, Observed Damage

Sample	**line No.**	**XGM** $[\mu J]$	**ATT** [%]	$\mathbf{E_{pulse}}[\mu J]$ **reached to sample**
Sample 3	69	45646.0	96.09	1473.9
	70	3894.7	96.18	1258.6
	71	4781.0	96.29	1546.8
	72	2895.5	52.07	506.6
	73	2279.2	51.98	398.1
	74	4014.6	51.87	699.7
	75	2988.2	27.22	273.3
	76	2991.1	26.97	271.0
	77	3777.1	27.10	343.9

Table B.3: Parameters for B_4C single-shot damage test at grazing angle 15 mrad.

B.6 B_4C, Single-Shot Damage Test at Grazing Angle 19 mrad, Observed Damage

Sample	line No.	XGM $[\mu J]$	ATT [%]	$\mathbf{E_{pulse}}[\mu J]$ reached to sample
Sample 2	1	4984.9	97.21	1674.9
	2	4603.4	60.99	943.5
	3	4949.7	38.52	640.3
	5	4805.9	23.23	371.4
	6	4290.5	14	201.8
	7	4688.2	9.32	144.9
	8	4438.8	6.9	102.9
	16	4717.3	56.1	887.6
	17	5038.2	59.92	1014.3
	18	4548.1	56.92	915.7
	19	4929.1	59.91	992.2
	20	4301.0	25.88	374.0
	21	4707.3	26.12	413.1
	22	4422.0	26.18	389.0
	23	4828.4	10.68	173.2
	24	4611.1	10.73	166.2
	25	5092.8	10.51	179.8
	26	4682.1	10.68	168.0

Table B.4: Parameters for B_4C single-shot damage test at grazing angle 19 mrad.

B.7 B_4C, Multi-Pulse Damage Test at Grazing Angle 9 mrad

Pulse/train	**Time of shootin**	**ATT** [%]	**E_{pulse} on sample** $[\mu J]$	**Fluence** $[\mu J/\mu m^2]$	**Damage**
30	10 sec	10	149.45	0.09	Yes
		3	48.16	0.03	No
		3	47.61	0.03	Yes
		1	15.11	0.009	No
		0.3	4.48	0.003	No
	5 min	10	165.83	0.1	Yes
		3	47.25	0.03	Yes
		3	48.49	0.03	Yes
		1	15.12	0.009	No
		0.3	4.57	0.003	No
300	10 sec	10	170.29	0.11	Yes
		3	47.27	0.03	Yes
		3	47.33	0.03	Yes
		0.3	3.81	0.002	No
	5 min	3	45.06	0.03	Yes
		3	46.46	0.03	Yes
		1	14.83	0.009	Yes
		0.3	4.54	0.003	Yes

Table B.5: Parameters for B_4C multi-pulse damage test at grazing angle 9 mrad.

Bibliography

[1] D. Attwood and A. Sakdinawat. *X-Rays and Extreme Ultraviolet Radiation: Principles and Applications*. Cambridge University Press, 2017. ISBN: 9781316810668. URL: https://books.google.de/books?id=TfmnDQAAQBAJ.

[2] Jens Als-Nielsen and Des McMorrow. *Elements of modern X-ray physics*. John Wiley & Sons, 2011.

[3] Carolyn MacDonald. *An introduction to x-ray physics, optics, and applications*. Princeton University Press, 2017.

[4] Henry P Freund and Thomas M Antonsen. *Principles of free-electron lasers*. Springer, 1992.

[5] Peter Schmüser et al. *Free-Electron Lasers in the Ultraviolet and X-Ray Regime: Physical Principles, Experimental Results, Technical Realization*. 2nd ed. Springer, 2014. ISBN: 978-3-642-54082-4.

[6] David Paganin. *Coherent X-ray optics*. 6. Oxford University Press, USA, 2006.

[7] S Serkez et al. "Overview of options for generating high-brightness attosecond x-ray pulses at free-electron lasers and applications at the European XFEL". In: *Journal of Optics* 20.2 (2018), p. 024005.

[8] Z Huang et al. "Brightness and coherence of synchrotron radiation and fels MOYCB101". In: *Proc. of IPAC (Shanghai, China)* (2013).

[9] Philip H Bucksbaum and Nora Berrah. "Brighter and faster: The promise and challenge of the X-ray free-electron laser". In: *Physics Today* 68.7 (2015), pp. 26–32.

[10] Henry N Chapman, Carl Caleman, and Nicusor Timneanu. "Diffraction before destruction". In: *Philosophical Transactions of the Royal Society B: Biological Sciences* 369.1647 (2014), p. 20130313.

[11] Wolfram Helml et al. "Ultrashort free-electron laser x-ray pulses". In: *Applied Sciences* 7.9 (2017), p. 915.

[12] Evgeny L Saldin, Evgeny A Schneidmiller, and Mikhail V Yurkov. "Coherence properties of the radiation from X-ray free electron laser". In: *Optics Communications* 281.5 (2008), pp. 1179–1188.

[13] Th Tschenscher and G Materlik. *TESLA Technical Design Report, Part V, The X-Ray Free Electron Laser*. 2002.

[14] Evgeny Schneidmiller, Mikhail Yurkov, et al. "Baseline parameters of the European XFEL". In: *Proc. FEL2017* (2017), pp. 109–112.

[15] V Balandin et al. "Optimized Bunch Compression System for the European XFEL". In: PAC. 2005.

[16] G Margaritondo and Primoz Rebernik Ribic. "A simplified description of X-ray free-electron lasers". In: *Journal of synchrotron radiation* 18.2 (2011), pp. 101–108.

[17] Primoz Rebernik Ribic and G Margaritondo. "Status and prospects of x-ray free-electron lasers (X-FELs): a simple presentation". In: *Journal of Physics D: Applied Physics* 45.21 (2012), p. 213001.

[18] Zhirong Huang and Kwang-Je Kim. "Review of x-ray free-electron laser theory". In: *Physical Review Special Topics—Accelerators and Beams* 10.3 (2007), p. 034801.

[19] Massimo Altarelli, Reinhard Brinkmann, and Majed Chergui. "The European X-ray free-electron laser. Technical design report". In: (2007).

[20] Hans Weise, Winfried Decking, et al. "Commissioning and first lasing of the European XFEL". In: *Proc. FEL'17* (2017), pp. 9–13.

[21] *How ultra-short light can improve data storage*. https://www.scienceinschool.org/article/2023/ultra-short-light-can-improve-data-storage/. Accessed: November 20, 2024.

[22] European XFEL. *Beamlines*. https://www.xfel.eu/facility/beamlines/index_eng.html. Accessed: 2024-07-09.

[23] Erdem Motuk et al. "Design and development of electronics for the EuXFEL clock and control system". In: *Journal of Instrumentation* 7.01 (2012), p. C01062.

[24] Thomas Tschentscher et al. "Photon beam transport and scientific instruments at the European XFEL". In: *Applied Sciences* 7.6 (2017), p. 592.

[25] Martin Dommach et al. "The photon beamline vacuum system of the European XFEL". In: *Journal of Synchrotron Radiation* 28.4 (2021), pp. 1229–1236.

[26] Harald Sinn et al. “Design of photon beamlines at the European XFEL”. In: *Proc. 32nd Int. Free Electron Laser Conf.(FEL'10)*. 2010, pp. 683–689.

[27] H Sinn et al. *Conceptual design report: X-ray optics and beam transport*. Tech. rep. European X-Ray Free-Electron Laser Facility GmbH, 2011.

[28] H Sinn et al. “X-ray optics and beam transport”. In: *European X-Ray Free-Electron Laser Facility GmbH, Hamburg, Germany* (2011).

[29] Tommaso Mazza et al. “The beam transport system for the Small Quantum Systems instrument at the European XFEL: optical layout and first commissioning results”. In: *Journal of synchrotron radiation* 30.2 (2023), pp. 457–467.

[30] Tim Salditt and Markus Osterhoff. “X-ray focusing and optics”. In: *Nanoscale photonic imaging* (2020), pp. 71–124.

[31] *Kirkpatrick-Baez (KB) mirror*. https://www.j-tec.co.jp/english/optical/optical-products/kb-mirror/. Accessed: November 20, 2024.

[32] Cameron M Kewish et al. “Wave-optical simulation of hard-x-ray nanofocusing by precisely figured elliptical mirrors”. In: *Applied Optics* 46.11 (2007), pp. 2010–2021.

[33] Malcolm R Howells et al. “Theory and practice of elliptically bent x-ray mirrors”. In: *Optical Engineering* 39.10 (2000), pp. 2748–2762.

[34] Tommaso Mazza et al. “Beam transport and focusing layout based on adaptive optics for the SQS scientific instrument at the European XFEL”. In: *Adaptive X-Ray Optics III*. Vol. 9208. SPIE. 2014, pp. 9–23.

[35] Ichiro Inoue et al. “Observation of femtosecond X-ray interactions with matter using an X-ray–X-ray pump–probe scheme”. In: *Proceedings of the National Academy of Sciences* 113.6 (2016), pp. 1492–1497.

[36] Manfred Faubel et al. “Ultrafast soft X-ray photoelectron spectroscopy at liquid water microjets”. In: *Accounts of chemical research* 45.1 (2012), pp. 120–130.

[37] Robert B Weakly et al. “Revealing core-valence interactions in solution with femtosecond X-ray pump X-ray probe spectroscopy”. In: *Nature Communications* 14.1 (2023), p. 3384.

[38] Carlo Kleine et al. “Soft X-ray absorption spectroscopy of aqueous solutions using a table-top femtosecond soft X-ray source”. In: *The journal of physical chemistry letters* 10.1 (2018), pp. 52–58.

[39] Enikoe Seres, Jozsef Seres, and Christian Spielmann. “Time resolved spectroscopy with femtosecond soft-x-ray pulses”. In: *Applied Physics A* 96 (2009), pp. 43–50.

[40] CS Lehmann et al. “Ultrafast x-ray-induced nuclear dynamics in diatomic molecules using femtosecond x-ray-pump–x-ray-probe spectroscopy”. In: *Physical Review A* 94.1 (2016), p. 013426.

[41] Antoine Rousse, Christian Rischel, and Jean-Claude Gauthier. “Femtosecond x-ray crystallography”. In: *Reviews of Modern Physics* 73.1 (2001), p. 17.

[42] Jasper J van Thor and Anders Madsen. “A split-beam probe-pump-probe scheme for femtosecond time resolved protein X-ray crystallography”. In: *Structural dynamics* 2.1 (2015).

[43] Gert Ingold et al. “Sub-Picosecond Tunable Hard X-Ray Undulator Source for Laser/X-Ray Pump-Probe Experiments”. In: *AIP Conference Proceedings*. Vol. 879. 1. American Institute of Physics. 2007, pp. 1198–1201.

[44] A Picón et al. “Hetero-site-specific X-ray pump-probe spectroscopy for femtosecond intramolecular dynamics”. In: *Nature communications* 7.1 (2016), p. 11652.

[45] JM Budarz et al. “Observation of femtosecond molecular dynamics via pump–probe gas phase x-ray scattering”. In: *Journal of Physics B: Atomic, Molecular and Optical Physics* 49.3 (2016), p. 034001.

[46] Jacob P Lee et al. “Few-femtosecond soft X-ray transient absorption spectroscopy with tuneable DUV-Vis pump pulses”. In: *Optica* 11.9 (2024), pp. 1320–1323.

[47] J Feldhaus et al. “Pump-probe experiments in the femtosecond regime, combining first and third harmonics of SASE FEL radiation”. In: *Free Electron Lasers 2002*. Elsevier, 2003, pp. 435–438.

[48] Lora Nugent-Glandorf et al. “A laser-based instrument for the study of ultrafast chemical dynamics by soft x-ray-probe photoelectron spectroscopy”. In: *Review of scientific instruments* 73.4 (2002), pp. 1875–1886.

[49] Etienne Gagnon et al. “Soft X-ray-driven femtosecond molecular dynamics”. In: *Science* 317.5843 (2007), pp. 1374–1378.

[50] Gerhard Ingold et al. “Towards pump-probe resonant X-ray diffraction at femtosecond undulator sources”. In: *Zeitschrift für Kristallographie-Crystalline Materials* 223.4-5 (2008), pp. 292–306.

[51] Xuan Liu et al. “Sub-15-fs X-ray pump and X-ray probe experiment for the study of ultrafast magnetization dynamics in ferromagnetic alloys”. In: *Optics Express* 29.20 (2021), pp. 32388–32403.

[52] Nadia L Opara et al. “Demonstration of femtosecond X-ray pump X-ray probe diffraction on protein crystals”. In: *Structural Dynamics* 5.5 (2018).

[53] Chelsea E Liekhus-Schmaltz et al. “Ultrafast x-ray pump x-ray probe transient absorption spectroscopy: A computational study and proposed experiment probing core-valence electronic correlations in solvated complexes”. In: *The Journal of Chemical Physics* 154.21 (2021).

[54] Gianluca Geloni et al. “Opportunities for Two-color Experiments at the SASE3 undulator line of the European XFEL”. In: *arXiv preprint arXiv:1706.00423* (2017).

[55] Svitozar Serkez et al. “Two colors at the SASE3 line of the European XFEL: Project scope and first measurements”. In: *39th Free Electron Laser Conference (FEL'19), Hamburg, Germany, 26-30 August 2019*. JACOW Publishing, Geneva, Switzerland. 2019, pp. 195–198.

[56] Svitozar Serkez et al. “Opportunities for two-color experiments in the soft X-ray regime at the European XFEL”. In: *Applied Sciences* 10.8 (2020), p. 2728.

[57] V Balandin et al. “Post-linac collimation system for the European XFEL”. In: *arXiv preprint arXiv:1305.1544* (2013).

[58] FMB Feinwerk- und Messtechnik GmbH. *Home*. https://www.fmb-berlin.de/. Accessed: 2024-11-05.

[59] COMSOL Multiphysics. “Introduction to COMSOL multiphysics®”. In: *COMSOL Multiphysics* 9 (1998), p. 2018.

[60] Frank Träger. *Springer handbook of lasers and optics*. Vol. 2. Springer, 2012.

[61] Eugene Hecht. *Optics*. Pearson Education India, 2012.

[62] Wadwan Singhapong et al. “Multilayer Optics for Synchrotron Applications”. In: *Advanced Materials Technologies* (2024), p. 2302187.

[63] SP Hau-Riege et al. “Wavelength dependence of the damage threshold of inorganic materials under extreme-ultraviolet free-electron-laser irradiation”. In: *Applied Physics Letters* 95.11 (2009).

[64] SP Hau-Riege et al. “Interaction of short x-ray pulses with low-Z x-ray optics materials at the LCLS free-electron laser”. In: *Optics express* 18.23 (2010), pp. 23933–23938.

[65] Lyman G Parratt. “Surface studies of solids by total reflection of X-rays”. In: *Physical review* 95.2 (1954), p. 359.

[66] T. Salditt and M. Osterhoff. “X-ray Focusing and Optics”. In: *Nanoscale Photonic Imaging*. Ed. by T. Salditt, A. Egner, and D. R. Luke. Vol. 134. Topics in Applied Physics. Springer, Cham, 2020. ISBN: 978-3-030-34412-2. DOI: 10.1007/978-3-030-34413-9_3. URL: https://doi.org/10.1007/978-3-030-34413-9_3.

[67] Metin Tolan. *X-Ray Scattering from Soft-Matter Thin Films. Materials Science and Basic Research*. 1st ed. Vol. 148. Springer Tracts in Modern Physics. Berlin, Heidelberg: Springer-Verlag Berlin Heidelberg, Oct. 1999, pp. IX, 198. ISBN: 978-3-662-14218-9. DOI: 10.1007/BFb0112834. URL: https://doi.org/10.1007/BFb0112834.

[68] Lawrence Berkeley National Laboratory (LBNL). *The Center for X-Ray Optics*. Available online. URL: https://henke.lbl.gov/optical_constants/.

[69] ZEISS. *an internationally leading technology enterprise operating in the optics and optoelectronics industries*. URL: https://www.zeiss.de.

[70] Idoia Freijo Martin et al. “Metrology and characterization of two optical delay line mirrors before and after B4C coating at European XFEL”. In: *Advances in Metrology for X-Ray and EUV Optics X*. Vol. 12695. SPIE. 2023, pp. 52–63.

[71] AM Engwall et al. “Sputter-deposited low-stress boron carbide films”. In: *Journal of Applied Physics* 128.17 (2020).

[72] Michael Störmer, Frank Siewert, and Harald Sinn. “Preparation and characterization of B4C coatings for advanced research light sources”. In: *Journal of Synchrotron Radiation* 23.1 (2016), pp. 50–58.

[73] Michael Störmer et al. “Single-layer and multilayer mirrors for current and next-generation light sources”. In: *Advances in X-Ray/EUV Optics and Components III*. Vol. 7077. SPIE. 2008, pp. 44–52.

[74] John XJ Zhang and Kazunori Hoshino. “Mechanical transducers: Cantilevers, acoustic wave sensors, and thermal sensors”. In: *Molecular sensors and nanodevices* (2019), pp. 311–412.

[75] Maria Rosa Ardigo, Maher Ahmed, and Aurélien Besnard. “Stoney formula: Investigation of curvature measurements by optical profilometer”. In: *Advanced Materials Research* 996 (2014), pp. 361–366.

[76] Ilia Petrov et al. “Simulation of wavefront propagation in diffraction of XFEL beams by single crystals”. In: *Advances in Computational Methods for X-Ray Optics V*. Vol. 11493. SPIE. 2020, pp. 151–157.

[77] Juan Reyes-Herrera et al. “X-ray beam quality after a mirror reflection: Experimental and simulated results for a toroidal mirror in a 4 th generation storage-ring beamline”. In: *Open Research Europe* 3 (2023).

[78] Luca Rebuffi and Xianbo Shi. “Advanced simulation tools in the OASYS suite and their applications to the APS-U optical design”. In: *Advances in Computational Methods for X-Ray Optics V*. Vol. 11493. SPIE. 2020, p. 1149303.

[79] Oleg Chubar et al. “Time-dependent FEL wavefront propagation calculations: Fourier optics approach”. In: *Nuclear Instruments and Methods in Physics Research Section A: Accelerators, Spectrometers, Detectors and Associated Equipment* 593.1-2 (2008), pp. 30–34.

[80] Oleg Chubar and P Elleaume. “Accurate and efficient computation of synchrotron radiation in the near field region”. In: *proc. of the EPAC98 Conference*. Vol. 1177. 1998.

[81] O Chubar et al. “Wavefront propagation simulations for beamlines and experiments with" Synchrotron Radiation Workshop"”. In: *Journal of Physics: Conference Series*. Vol. 425. 16. IOP Publishing. 2013, p. 162001.

[82] J Gaudin et al. “Damage study for the design of the European XFEL beamline optics.” In: *Damage to VUV, EUV, and X-Ray Optics II*. Vol. 7361. SPIE. 2009, pp. 15–21.

[83] MA Antimonov et al. “On the influence of monochromator thermal deformations on X-ray focusing”. In: *Nuclear Instruments and Methods in Physics Research Section A: Accelerators, Spectrometers, Detectors and Associated Equipment* 820 (2016), pp. 164–171.

[84] Jacek Krzywinski et al. “Damage threshold of platinum coating used for optics for self-seeding of soft x-ray free electron laser”. In: *Optics Express* 23.5 (2015), pp. 5397–5405.

[85] Richard A London et al. “Computational simulations of high-intensity x-ray matter interaction”. In: *Optics for Fourth-Generation X-Ray Sources*. Vol. 4500. SPIE. 2001, pp. 51–62.

[86] Marziyeh Tavakkoly et al. “Simulations about stability, damage, and heating impacts for an x-ray optical delay line at sase3”. In: *Journal of Physics: Conference Series*. Vol. 2380. 1. IOP Publishing. 2022, p. 012066.

[87] Harald Sinn. “Heat load estimates for XFEL beamline optics”. In: *energy* 10 (2007), p. 2.

[88] Ryszard Sobierajski et al. “Role of heat accumulation in the multi-shot damage of silicon irradiated with femtosecond XUV pulses at a 1 MHz repetition rate”. In: *Optics express* 24.14 (2016), pp. 15468–15477.

[89] Roman Shayduk and Peter Gaal. “Transition regime in the ultrafast laser heating of solids”. In: *Journal of Applied Physics* 127.7 (2020).

[90] Steven T Yang et al. “Comparing the use of mid-infrared versus far-infrared lasers for mitigating damage growth on fused silica”. In: *Applied Optics* 49.14 (2010), pp. 2606–2616.

[91] Kelin Regina Tasca et al. “Study of a diamond channel cut monochromator for high repetition rate operation at the EuXFEL: FEA thermal load simulations and first experimental results”. In: *Journal of Physics: Conference Series*. Vol. 2380. 1. IOP Publishing. 2022, p. 012053.

[92] Daniel Nilsson et al. “Simulation of heat transfer in zone plate optics irradiated by X-ray free electron laser radiation”. In: *Nuclear Instruments and Methods in Physics Research Section A: Accelerators, Spectrometers, Detectors and Associated Equipment* 621.1-3 (2010), pp. 620–626.

[93] Mohamed Darif, Nadjib Semmar, and France Orléans Cedex. “Numerical simulation of Si nanosecond laser annealing by COMSOL multiphysics”. In: *Proceedings of the COMSOL Conference 2008 Hannover*. 2008, pp. 567–571.

[94] Nikita Medvedev. “Electron-phonon coupling in semiconductors at high electronic temperatures”. In: *Physical Review B* 108.14 (2023), p. 144305.

[95] Takahisa Koyama et al. “Damage threshold of coating materials on x-ray mirror for x-ray free electron laser”. In: *Review of Scientific Instruments* 87.5 (2016).

[96] Andrew Aquila et al. “Fluence thresholds for grazing incidence hard x-ray mirrors”. In: *Applied physics letters* 106.24 (2015).

[97] Jinyu Cao et al. “Damage resistance of B 4 C reflective mirror irradiated by X-ray free-electron laser”. In: *Chinese Optics Letters* 21.2 (2023), p. 023401.

[98] Sh Dastjani Farahani et al. “Damage threshold of amorphous carbon mirror for 177 eV FEL radiation”. In: *Nuclear Instruments and Methods in Physics Research Section A: Accelerators, Spectrometers, Detectors and Associated Equipment* 635.1 (2011), S39–S42.

[99] Kazuto Yamauchi et al. “Nanofocusing of X-ray free-electron lasers by grazing-incidence reflective optics”. In: *Journal of Synchrotron Radiation* 22.3 (2015), pp. 592–598.

[100] Jacek Krzywinski et al. “Damage thresholds for blaze diffraction gratings and grazing incidence optics at an X-ray free-electron laser”. In: *Journal of Synchrotron Radiation* 25.1 (2018), pp. 85–90.

[101] Jangwoo Kim et al. “Damage threshold of platinum/carbon multilayers under hard X-ray free-electron laser irradiation”. In: *Optics Express* 23.22 (2015), pp. 29032–29037.

[102] T Koyama et al. “Damage threshold investigation using grazing incidence irradiation by hard X-ray free electron laser”. In: *Advances in X-Ray/EUV Optics and Components VIII*. Vol. 8848. SPIE. 2013, pp. 186–192.

[103] Stefan P Hau-Riege et al. “Multiple pulse thermal damage thresholds of materials for x-ray free electron laser optics investigated with an ultraviolet laser”. In: *Applied Physics Letters* 93.20 (2008).

[104] Thanh-Hung Dinh et al. “Controlled strong excitation of silicon as a step towards processing materials at sub-nanometer precision”. In: *Communications Physics* 2.1 (2019), p. 150.

[105] Tingting Sui et al. “The Influence of B4C Film Density on Damage Threshold Based on Monte Carlo Method for X-ray Mirror”. In: *Materials* 17.5 (2024), p. 1026.

[106] J Sempau et al. “An algorithm for Monte Carlo simulation of coupled electron-photon transport”. In: *Nuclear Instruments and Methods in Physics Research Section B: Beam Interactions with Materials and Atoms* 132.3 (1997), pp. 377–390.

[107] Eleonora Secco and Manuel Sánchez del Rıo. “Monte Carlo simulations of scattered power from irradiated optical elements”. In: *Advances in Computational Methods for X-Ray Optics II*. Vol. 8141. SPIE. 2011, pp. 305–316.

[108] Xavier Llovet and Francesc Salvat. “PENEPMA: A Monte Carlo program for the simulation of X-ray emission in electron probe microanalysis”. In: *Microscopy and Microanalysis* 23.3 (2017), pp. 634–646.

[109] Nanshun Huang and Haixiao Deng. “Thermal loading on crystals in an X-ray free-electron laser oscillator”. In: *Physical Review Accelerators and Beams* 23.9 (2020), p. 090704.

[110] Michael Störmer, Frank Siewert, and Harald Sinn. “Preparation and characterization of B4C coatings for advanced research light sources”. In: *Journal of Synchrotron Radiation* 23.1 (2016), pp. 50–58.

[111] T Mazza, H Zhang, and M Meyer. “Scientific instrument SQS”. In: *Tech. Des. Rep* (2012).

[112] Thomas M Baumann et al. “Harmonic radiation contribution and X-ray transmission at the Small Quantum Systems instrument of European XFEL”. In: *Journal of Synchrotron Radiation* 30.4 (2023).

[113] J Chalupskỳ et al. “Characteristics of focused soft X-ray free-electron laser beam determined by ablation of organic molecular solids”. In: *Optics Express* 15.10 (2007), pp. 6036–6043.

[114] Jaromır Chalupskỳ et al. “Fluence scan: an unexplored property of a laser beam”. In: *Optics express* 21.22 (2013), pp. 26363–26375.

[115] J. Chalupský et al. “Spot size characterization of focused non-Gaussian X-ray laser beams”. In: *Optics express* 18.26 (2010), pp. 27836–27845.

[116] Vojtěch Vozda et al. “Characterization of megahertz X-ray laser beams by multishot desorption imprints in PMMA”. In: *Optics express* 28.18 (2020), pp. 25664–25681.

[117] Takahisa Koyama et al. “Investigation of ablation thresholds of optical materials using 1-μm-focusing beam at hard X-ray free electron laser”. In: *Optics express* 21.13 (2013), pp. 15382–15388.

[118] J Gaudin et al. “Amorphous to crystalline phase transition in carbon induced by intense femtosecond x-ray free-electron laser pulses”. In: *Physical Review B—Condensed Matter and Materials Physics* 86.2 (2012), p. 024103.

[119] J Chalupskỳ et al. “Damage of amorphous carbon induced by soft x-ray femtosecond pulses above and below the critical angle”. In: *Applied Physics Letters* 95.3 (2009).

[120] J Chalupskỳ et al. “Deep learning for laser beam imprinting”. In: *Optics Express* 31.12 (2023), pp. 19703–19721.

[121] Jia-Ming Liu. “Simple technique for measurements of pulsed Gaussian-beam spot sizes”. In: *Optics letters* 7.5 (1982), pp. 196–198.

[122] Andrew Aquila et al. “Results from single shot grazing incidence hard x-ray damage measurements conducted at the SACLA FEL”. In: *Damage to VUV, EUV, and X-ray Optics IV; and EUV and X-ray Optics: Synergy between Laboratory and Space III*. Vol. 8777. SPIE. 2013, pp. 98–101.

[123] V Hajkova et al. “X-ray laser-induced ablation of lead compounds”. In: *Damage to Vuv, Euv, and X-Ray Optics III*. Vol. 8077. SPIE. 2011, pp. 275–281.

[124] R Sobierajski et al. “Experimental set-up and procedures for the investigation of XUV free electron laser interactions with solids”. In: *Journal of instrumentation* 8.02 (2013), P02010.

[125] Igor A Makhotkin et al. “Experimental study of EUV mirror radiation damage resistance under long-term free-electron laser exposures below the single-shot damage threshold”. In: *Journal of synchrotron radiation* 25.1 (2018), pp. 77–84.

[126] Takahisa Koyama et al. “Damage to inorganic materials illuminated by focused beam of X-ray free-electron laser radiation”. In: *Damage to VUV, EUV, and X-ray Optics V*. Vol. 9511. SPIE. 2015, p. 951107.

[127] Stefan Hau-Riege. *Absorbed XFEL dose in the components of the LCLS X-Ray optics*. Tech. rep. Lawrence Livermore National Lab.(LLNL), Livermore, CA (United States), 2005.

[128] SP Hau-Riege et al. “Damage threshold of inorganic solids under free-electron-laser irradiation at 32.5 nm wavelength”. In: *Applied Physics Letters* 90.17 (2007).

[129] A. Ferrari et al. *FLUKA: a multi-particle transport code*. Tech. rep. CERN-2005-10. INFN/TC_05/11, SLAC-R-773. CERN, 2005.

[130] A.Fassò, A.Ferrari, J.Ranft, and P.R.Sala. *Release notes for Fluka2024.1*. Available online. URL: http://www.fluka.org/fluka.php?id=release_notes.

[131] LF Pires et al. “Gamma ray attenuation for determining soil density: laboratory experiments for Environmental Physics and Engineering courses”. In: *Revista Brasileira de Ensino de Fısica* 42 (2020), e20190340.

[132] Wenbin Li et al. “Damage study on B4C films using a table-top nanosecond EUV damage instrument”. In: *EUV and X-ray Optics, Sources, and Instrumentation*. Vol. 11776. SPIE. 2021, pp. 109–116.

[133] Kazuki Yoshikawa et al. “Time-resolved photoelectron diffraction imaging of methanol photodissociation involving molecular hydrogen ejection”. In: *Physical Chemistry Chemical Physics* 26.38 (2024), pp. 25118–25130.

[134] JR Crespo López-Urrutia, P Beiersdorfer, and K Widmann. “Lifetime of the 1 s 2 s S 1 3 metastable level in He-like S 14+ measured with an electron beam ion trap”. In: *Physical Review A—Atomic, Molecular, and Optical Physics* 74.1 (2006), p. 012507.

[135] H-D Betz et al. “New technique for the measurement of lifetimes of heavy-ion inner-shell vacancies”. In: *Physical Review Letters* 33.14 (1974), p. 807.

[136] P Beiersdorfer et al. “Observation of lifetime-limited X-ray linewidths in cold highly charged ions”. In: *Physical review letters* 77.27 (1996), p. 5353.

[137] L Zhang et al. “Performance studies of cryogenically cooled monochromator crystals for X-FELs”. In: *AIP Conference Proceedings*. Vol. 705. 1. American Institute of Physics. 2004, pp. 639–642.

[138] Daniel Malacara. “Optical Shop Testing”. In: *Wiely Interscience* (2007).

[139] Maurizio Vannoni and Idoia Freijo Martın. “Absolute interferometric characterization of an x-ray mirror surface profile”. In: *Metrologia* 53.1 (2015), p. 1.

[140] *What is a Fizeau Interferometer?* https://qd-uki.co.uk/what-is-a-fizeau-interferometer/. Accessed: November 20, 2024.

[141] Pavel Pavliček and Erik Mikeska. “White-light interferometer without mechanical scanning”. In: *Optics and Lasers in Engineering* 124 (2020), p. 105800.

[142] Nathan Ida and Norbert Meyendorf. *Handbook of advanced nondestructive evaluation*. Vol. 10. Springer International Publishing Cham, Switzerland, 2019.

[143] Joanna Schmit and Anna Pakuła. “White light interferometry”. In: (2019).

[144] James C Wyant. “White light interferometry”. In: *Holography: a tribute to yuri denisyuk and emmett leith*. Vol. 4737. SPIE. 2002, pp. 98–107.

[145] Peter De Groot. “Principles of interference microscopy for the measurement of surface topography”. In: *Advances in Optics and Photonics* 7.1 (2015), pp. 1–65.

[146] T Mazza, Haiou Zhang, and Michael Meyer. *Technical Design Report: Scientific Instrument SQS*. Tech. rep. European X-Ray Free-Electron Laser Facility GmbH, 2012.

[147] Andrey A Sorokin et al. “An X-ray gas monitor for free-electron lasers”. In: *Journal of synchrotron radiation* 26.4 (2019), pp. 1092–1100.

[148] Theophilos Maltezopoulos et al. “Operation of X-ray gas monitors at the European XFEL”. In: *Journal of synchrotron radiation* 26.4 (2019), pp. 1045–1051.

[149] Jan Grünert et al. “X-ray photon diagnostics at the European XFEL”. In: *Journal of Synchrotron Radiation* 26.5 (2019), pp. 1422–1431.

[150] Yiping Feng et al. “Time-dependent simulation of the gas attenuator for the LCLS-II X-ray FEL’s under high beam power operations”. In: *X-Ray Lasers and Coherent X-Ray Sources: Development and Applications XI*. Vol. 9589. SPIE. 2015, pp. 125–134.

[151] DD Ryutov et al. *The Physics of the Gas Attenuator for the Linac Coherent Light Source (LCLS)*. Tech. rep. Lawrence Livermore National Lab.(LLNL), Livermore, CA (United States), 2009.

[152] Raúl Villanueva Guerrero. *SASE3 Gas Attenuator Device PLC Interlock System*. Tech. rep. European XFEL, 2020.

[153] Raúl Villanueva Guerrero. "The Gas Attenuator Instrument for SASE3 Soft X-Ray Beamline at the European XFEL". In: *European XFEL Users' Meeting*. 2014.